UNIVERSITY OF CALIFORNIA
Los Angeles

Laser-Produced Plasmas as Drivers of Quasi-Parallel Collisionless Shock Formation in the Laboratory

A dissertation submitted in partial satisfaction
of the requirements for the degree
Doctor of Philosophy in Physics

by

Peter Ver Bryck Heuer

2020

ABSTRACT OF THE DISSERTATION

Laser-Produced Plasmas as Drivers of Quasi-Parallel Collisionless Shock Formation in the Laboratory

by

Peter Ver Bryck Heuer
Doctor of Philosophy in Physics
University of California, Los Angeles, 2020
Professor Christoph Niemann, Chair

Quasi-parallel collisionless shocks are objects of considerable interest in space and astrophysics, most notably as possible sites of cosmic ray acceleration. Such shocks occur naturally in systems such as supernova remnants and planetary bow shocks, where the complex and turbulent structures they form are commonly observed by spacecraft. However, *in situ* spacecraft measurements have some inherent limitations, such as a moving reference frame and non-repeatable measurements. Generating a quasi-parallel collisionless shock in a repeatable, well-diagnosed laboratory environment could therefore improve our understanding of their formation and structure.

The quasi-parallel collisionless shocks observed in space and astrophysics are far too large to fit in a laboratory, but scaled versions of these systems can be created using smaller, denser plasmas with similar dimensionless parameters. However, quasi-parallel collisionless shocks are particularly challenging to scale to a feasible experiment. The shock formation process is mediated by several electromagnetic ion/ion beam instabilities which require long length scales (> 500 ion-inertial lengths) to grow, so an experiment must include a long

magnetized background plasma. This background plasma must be overlapped over the same length by a highly super-Alfvénic beam plasma. Matching the dimensionless parameters of the shocks observed in space sets demanding requirements on the densities of both plasmas as well as the background magnetic field strength. Laser-produced plasmas (LPPs) provide a promising beam plasma source (a "driver") for such experiments.

A recent experimental campaign has been conducted at UCLA to investigate the potential of LPPs as drivers of quasi-parallel collisionless shocks. These experiments combine one of two high-energy lasers with the magnetized background plasma of the Large Plasma Device (LAPD) to drive the electromagnetic ion/ion beam instabilities responsible for shock formation. The experiments have observed electromagnetic waves consistent with the very early stages of quasi-parallel shock formation. These waves are similar to the ultra-low frequency (ULF) waves observed by spacecraft upstream of the Earth's quasi-parallel bow shock. At present, the amplitudes of the waves generated by these experiments are too low ($dB/B_0 \sim 0.01$) to fully form a quasi-parallel shock.

The wave amplitudes observed in these experiments are low because the conditions for beam instability growth are only met in a small region near the laser target. Outside of this region, decreasing LPP density due to velocity dispersion and cross-field transport terminates the wave growth and consequently the shock formation process. Future experiments will require technical innovations to expand this growth region in order to produce larger-amplitude waves. Promising approaches including trains of laser pulses and heating electrons in the background plasma to reduce collisional cross-field transport. Along with comparisons to analytic theory and simulations, the results of the current experiments can inform the design of future laboratory quasi-parallel shock experiments.

The dissertation of Peter Ver Bryck Heuer is approved.

Troy A. Carter

Walter N. Gekelman

Christopher T. Russell

Christoph Niemann, Committee Chair

University of California, Los Angeles

2020

To Cathy

TABLE OF CONTENTS

LIST OF FIGURES

LIST OF TABLES

ACKNOWLEDGMENTS

I would like to thank:

Andrew Hutton, Phil Adderley, Marcy Stutzman, and all of the other scientist and staff at the Thomas Jefferson National Accelerator Facility who volunteered their time to work with a couple of high school students and, in doing so, launched my career.

My doctors, especially Peter Rowe, for making everything else possible.

Stephen Vincena and Shreekrishna Tripathi, for their advice, for fixing the LAPD countless times, and for often staying very late to squeeze out one more data run.

Patrick Pribyl, Lucky Zoltan, Marvin Drandell, Tai Ly, and Avdit Kohli for their help and many quick repair jobs.

Derek Schaeffer, Carmen Constantin, and especially my advisor Christoph Niemann, for their invaluable leadership, mentorship, and support.

My committee members: Troy Carter, Walter Gekelman, and Chris Russell, for their feedback and advice throughout this process.

Dan Winske, for his support of this project, and for laying much of the theoretical foundations on which it rests.

Lynn Wilson, for being a great collaborator and answering every long email of questions with an even longer email of detailed answers.

My fellow graduate students, especially my colleagues Bobby Dorst and Jessica Pilgrim, for all of their help and companionship.

Martin Weidl, for being the best theorist/computationalist an experimentalist could ever hope to work with.

And my brother, sister, and parents for all of their love and support.

VITA

2014	B.S. (Physics), University of Rochester
2016	M.S. (Physics), University of California, Los Angeles
2014-2015	Teaching Fellow, University of California, Los Angeles
2015-2020	Research Fellow, University of California, Los Angeles

PUBLICATIONS

P. V. Heuer, M. S. Weidl, R. S. Dorst, D. B. Schaeffer, S. K. Tripathi, S. Vincena, C. G. Constantin, C. Niemann, D. Winske (2020) Laser-produced plasmas as drivers of laboratory collisionless quasi-parallel shocks. *Physics of Plasmas*, 27 (4), 042103

P. V. Heuer, M. S. Weidl, R. S. Dorst, D. B. Schaeffer, S. K. Tripathi, S. Vincena, C. G. Constantin, C. Niemann, L. Wilson III, D. Winske (2020) Laboratory measurements of ULF-analogue waves driven by the right-hand resonant ion beam instability. *The Astrophysical Journal Letters*, 891 (1), L11

P. V. Heuer, M. S. Weidl, R. S. Dorst, D. B. Schaeffer, A. S. Bondarenko, S. K. P. Tripathi, B. Van Compernolle, S. Vincena, C. G. Constantin, C. Niemann, D. Winske (2018) Observations of a field-aligned ion/ion-beam instability in a magnetized laboratory plasma. *Physics of Plasmas*, 25 (3), 032104

P. V. Heuer, D. B. Schaeffer, E. N. Knall, C. G. Constantin, L. R. Hofer, S. Vincena, S. Tripathi, C. Niemann (2017) Fast gated imaging of the collisionless interaction of a laser-produced and magnetized ambient plasma. *High Energy Density Physics*, 22, 17-20

CHAPTER 1

Introduction

Collisionless shocks are discontinuities formed by the interaction of a supersonic plasma with a subsonic plasma in the absence of single-particle collisions [20], and are objects of considerable interest in space and astrophysics [18, 19]. Collisionless bow shocks form the boundaries of planetary magnetospheres [128, 66], protecting planets from the solar wind. Interplanetary collisionless shocks also form within the solar wind [126, 139]. Understanding the behavior of these systems is key to forecasting the impact of violent solar weather events like coronal mass ejections on the Earth [27]. Bow shocks are also formed by other objects in the solar system such as comets [125]. At the edge of the solar system, the termination shock is a collisionless shock that separates the heliosphere from the intergalactic medium [150, 114]. Similar solar bow shocks formed by other stars have also been observed [98]. Supernovae also create collisionless shocks as stellar material explodes into the interstellar medium. The resulting shock continues to propagate outward long after the explosion, forming a supernova remnant. Particle acceleration via the diffusive shock acceleration mechanism in these objects may provide an explanation for the origin of extremely high-energy cosmic rays [12, 22].

Collisionless shocks in space are typically magnetized, and the dynamics of the shock depend strongly on the angle between the velocity of the supersonic plasma and the ambient magnetic field, θ_n (Fig. 1.1). A shock (or part of a shock) in which the inflowing plasma streams nearly parallel ($\theta_n \sim 0^\circ$) or nearly perpendicular ($\theta_n \sim 90^\circ$) to the ambient magnetic field is called a quasi-parallel or quasi-perpendicular shock respectively. The processes that mediate shock formation in the quasi-parallel regions are slower and more turbulent than

in the quasi-perpendicular regions, leading to the development of extended complicated structures (Fig. 1.2). These structures make quasi-parallel shocks particularly interesting as sites of particle acceleration [40], and particularly complicated to understand.

Astrophysical shocks such as supernova remnants have been observed remotely, providing evidence of particle acceleration [1]. Spacecraft orbiting the Earth have made many *in situ* measurements of waves [51, 142, 29] and particle distributions [97, 39] throughout the terrestrial quasi-parallel bow shock. Recent multi-spacecraft missions have enabled the first low-resolution spatially resolved measurements in this region [49, 84]. Further flung spacecraft have observed similar bow shock structures at comets [50, 125] and other planets throughout the solar system [103]. Recently the Voyager spacecraft provided the first direct measurements of the solar wind's termination shock [114].

However, spacecraft measurements have several limitations. Single spacecraft missions have no spatial resolution transverse to the spacecraft trajectory, while multi-spacecraft missions are limited to a small number of transverse datapoints. Spacecraft measurements are inherently acquired in a moving reference frame from which properties in the plasma rest frame must be derived. Moving spacecraft cannot measure changes as a function of time at a fixed location, making it difficult to seperate the temporal and spatial evolution of a strucure (a problem often addressed by invoking the Taylor hypothesis [117]). *In situ* measurements are dependent on natural enviromental variations to make observations under different conditions. Remote shock systems, such as supernova remnants [40], are entirely physically inaccessible.

All of these limitations could potentially be addressed by laboratory experiments [30, 67]. Control over experimental conditions enables systematic investigation of parameter scaling [105] and access to conditions relevant to remote space and astrophysical systems. Measurements can be taken directly in the plasma rest frame, removing a potential source of error. Arrays of probes that are stationary in the plasma rest frame can unambiguously observe the growth and evolution of both spatial and temporal features. Repeatable mea-

surements allow for the collection of volumetric datasets with high temporal and spatial resolution [107]. These measurements can then be used to validate theory, benchmark simulations, and inform the interpretation of spacecraft observations. Perpendicular collisionless shocks [147, 90, 106] and shocks with self-generated magnetic fields have been studied in previous experiments [36, 70, 95], but a quasi-parallel collisionless shock has not yet been produced in the laboratory.

The quasi-parallel collisionless shocks observed in space and astrophysics are far too large to fit in a laboratory, but scaled versions of these systems can be created using smaller, denser plasmas with similar dimensionless parameters. However, quasi-parallel collisionless shocks are particularly challenging to scale to a feasible experiment. The shock formation process is mediated by several electromagnetic ion/ion beam instabilities which require long length scales ($L > 500$ ion-inertial lengths, where L is the experiment length scale) to grow, so an experiment must include a long magnetized background or "core" plasma. This core plasma must be overlapped over the same length by a highly super-Alfvénic "beam" plasma. Matching the dimensionless parameters of shocks observed in space sets demanding requirements on the densities of both the beam and core plasmas (n_b and n_c respectively), the beam velocity (v_b), and the background magnetic field strength (B_0). Laser-produced plasmas (LPPs) provide a promising beam plasma source (a "driver") for such experiments.

A recent series of experiments has been conducted at the University of California Los Angeles (UCLA) to evaluate the potential of LPPs as drivers of quasi-parallel collisionless shocks. A beam plasma created using one of two high-energy lasers interacts with a magnetized core plasma produced by the Large Plasma Device (LAPD) [47]. The beam plasma flows nearly parallel to the background magnetic field ($\theta_n \sim 0°$). Waves generated by electromagnetic beam instabilities are measured using an array of magnetic flux probes.

Although the parameters of the plasmas produced in the experiment are very different from the corresponding parameters in space, the dimensionless ratios of these quantities relevant to quasi-parallel shock formation are comparable (Table 1.1). In particular, experi-

	Laboratory	Foreshock
Core Ions	He^{+1}	p^+
Beam Ions	C^{+2}-C^{+5}	p^+
L (m)	12	$> 10^7$
B_0 (G)	300	5×10^{-5}
δ_{ci} (m)	0.14	10^5
ω_{cc} (rad/s)	7×10^5	0.5
v_A (km/s)	100	50
n_c (cm^{-3})	10^{13}	5
v_b (km/s)	400	300
λ_{mfp} (m)	4×10^3	10^{13}
n_b/n_c	$\sim 10\%$	$\sim 10\%$
$v_b/v_{b,th}$	$\sim 50\%$	$\sim 50\%$
L/δ_{ci}	80	> 100
L/λ_{mfp}	3×10^{-3}	10^{-6}
v_b/v_A	4	6

Table 1.1: A comparison of physical parameters and dimensionless quantities between the laboratory experiments and the Earth's quasi-parallel foreshock. L is the system length, λ_{mfp} is the beam ion/core ion Coulomb mean free path, and $v_{b,th}$ is the beam thermal velocity. Parameters vary substantially throughout both the experiment and the foreshock, but these values are representative. Foreshock parameters are based on measurements made by the Wind spacecraft [142].

mental parameters were chosen to be comparable to those measured in the foreshock region of the Earth's quasi-parallel bow shock. Important scaling parameters for length and time scales are the core ion cyclotron frequency $\omega_{cc} = q_c B_0/m_c = 2\pi f_{ci}$ (where q_c is the core ion charge, B_0 is the magnitude of the background magnetic field, and m_c is the core ion mass) and the core ion inertial length $\delta_{ci} = v_A/\omega_{cc}$ (where $v_A = B_0/\sqrt{\mu_0 n_c m_c}$ is the Alfvén velocity in the core plasma, μ_0 is the permeability of free space, and n_c is the density of the core plasma). The experiment length scale L is far smaller than the beam ion/core ion Coulomb mean free path λ_{mfp}, so the ion dynamics are effectively collisionless. The dimensionless experiment length L/δ_{ci} is too small to hold a fully-formed parallel shock, but is sufficient to observe the early stages of instability growth [135]. The experiment utilizes different species of core and beam ions than are typically present in space, which results in waves of slightly higher-frequency (when normalized to ω_{cc}) but which are otherwise similar to those

observed by spacecraft [63, 64]. The beam drift velocities v_b, beam thermal velocities $v_{b,th}$, core plasma Alfvén velocities v_A, and beam Alfvénic Mach numbers are directly comparable to conditions in the Earth's bow shock.

These experiments have observed ion/ion beam instability growth consistent with the very early (linear) stages of quasi-parallel shock formation [62] including the generation of waves directly comparable to those observed far upstream of planetary bow shocks [63]. However, spatial dispersion quickly reduces the LPP density below the shock formation threshold, terminating the process before the waves reach large amplitudes [64]. Novel techniques to counteract this dispersion as well as improved facilities are necessary in order for future experiments to produce a fully-formed quasi-parallel collisionless shock.

1.1 Definition and Classification of Shocks

A shock is a sharp discontinuity that forms between two fluids when the relative velocity between the fluids is greater than the local characteristic sound speed [20]. The resulting boundary could be either stationary or moving in the rest frame. Examples include the bow shock formed by a body in a supersonic flow (stationary) or a blast wave propagating away from a powerful explosion (moving). When viewed in a reference frame in which the shock transition is stationary (the shock frame), these systems are identical. In the shock frame, the unshocked supersonic fluid is called the upstream or inflow and the post-shock fluid is called the downstream or background (Fig. 1.1). Shocks are characterized by their Mach number, M, defined as the ratio between the inflowing fluid velocity and the characteristic sound speed in the downstream fluid.

Because by definition energy arrives at a shock faster than waves could transport it away, the energy of the inflowing fluid must be dissipated locally, for example as heat. The efficiency of this dissipation process determines the width of the shock transition, with instantaneous dissipation leading to a shock of zero width. The dissipation mechanism is also the primary

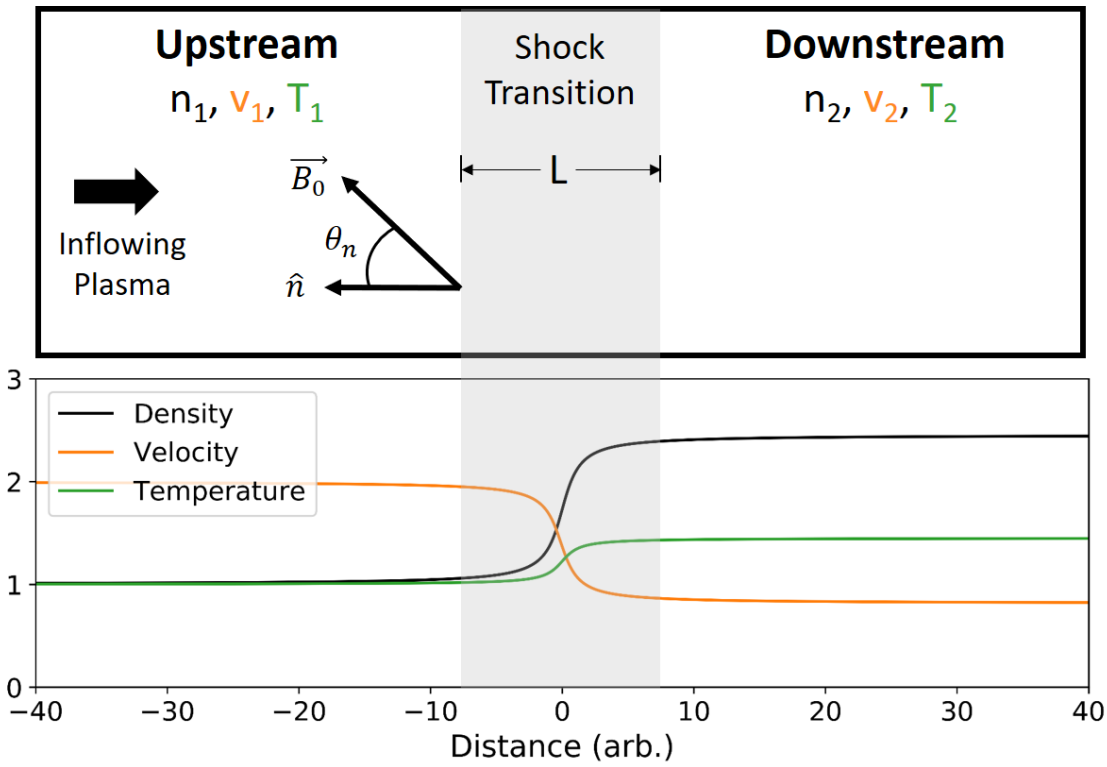

Figure 1.1: A cartoon diagram of a fluid shock shows the upstream and downstream regions separated by a shock transition region of finite width. The shock slows, compresses, and heats the inflowing plasma within the shock transition. Simple curves are plotted here for illustrative purposes, but in actual shocks the way quantities vary through the transition region is complex and depends strongly on the type of shock in question.

distinguishing feature between different types of of shock. Shocks that form in dense fluids in which intra-particle collisions dissipate energy are classified as collisional (or hydrodynamic) shocks. The characteristic length and time scales of such shocks are the particle mean free path, λ_{mfp}, and the collision frequency ν_c. If L is the system length scale, then the definition of a collisional shock can be expressed as $L > \lambda_{mfp}$.

In contrast, shocks that form in the absence of intra-particle collisions are called collisionless ($L < \lambda_{mfp}$). Such shocks are mediated by the formation of structures in the bulk electromagnetic fields (rather than than the single particle fields involved in a Coulomb collision), and are therefore inherently plasma phenomena with no neutral fluid analog. As collisions become negligible, the characteristic physical length and time scales become the ion inertial length δ_{ci} and the inverse of the ion cyclotron frequency f_{ci}^{-1}. The characteristic sound speed is either the magnetosonic sound speed c_s or the Alfvén velocity v_A, depending on how well-magnetized the system is. The Mach numbers corresponding to each sound speed are defined as $M_s = v/c_s$ and $M_A = v/v_A$ respectively.

Collisionless shocks can dissipate energy through several mechanisms. At such high frequencies ($\sim f_{ci}$), dispersive plasma waves can propagate with group velocities much higher than the characteristic sound speeds, allowing them to transport energy away from the shock transition. The capacity of wave dissipation to disperse energy is limited (because the wave speed is not infinite). Shocks that dissipate energy only through wave dissipation are termed sub-critical. Collisionless shocks can also generate large magnetic fields transverse to the inflowing plasma, or electric fields parallel to the flow, which can dissipate energy by scattering (and therefore thermalizing) particles. These fields can also reflect inflowing particles back into the upstream region. Shocks that dissipate energy at least in part by particle reflection are termed super-critical. Collisionless shocks are also capable of accelerating a small number of particles to very high energies through the process of diffusive shock acceleration [13, 8, 7].

The dynamics of collisionless shock formation are strongly influenced by the strength and orientation of the ambient magnetic field. The degree of magnetization is defined by the Hall

parameter $\chi = f_{ci}/\nu_c$, with $\chi > 1$ signifying a magnetized plasma. Initially unmagnetized collisionless shocks must self-generate transverse magnetic fields through mechanisms like the Weibel instability [36]. Magnetized collisionless shocks are classified as either quasi-parallel or quasi-perpendicular based on the angle between their shock normal and the ambient magnetic field, θ_n. Shocks where $0° \leq \theta_n \leq 45°$ are considered to be quasi-parallel because they involve similar formation physics as nearly-parallel shocks where $\theta_n \sim 0°$ [52]. Shocks where $45° \leq \theta_n \leq 90°$ are considered quasi-perpendicular. Shocks near the boundary of these ranges where $0° \ll \theta_n \ll 90°$ are also sometimes referred to as oblique. Perpendicular collisionless shocks are sub-critical up to $M_A \sim 3$, and are characterized by narrow shock widths of approximately one ion-inertial length. Quasi-parallel shocks are always super-critical and are hundreds of ion-inertial lengths wide.

On sufficiently large scales, collisionless shocks share many properties of collisional shocks. The Rankine-Hugoniot jump conditions derivable for fluid shocks are satisfied between the far upstream and far downstream of collisionless shocks. However, fluid theories do not capture the ion-scale dynamics responsible for collisionless dissipation mechanisms. Parallel shocks in magnetohydrodynamics are completely unaffected by the presence of a magnetic field [35], which is far from accurate in the collisionless case. The study of this collisionless shock microphysics therefore requires the use of kinetic theory [19].

1.2 The Structure of Quasi-Parallel Shocks

Quasi-perpendicular shocks dissipate energy within a relatively thin shock transitions ($L \sim \delta_{ci}$) outside of which something resembling the jump conditions of a fluid shock are satisfied (Fig. 1.2a). In contrast, quasi-parallel shocks dissipate energy throughout large regions of turbulence that extend far from the nominal shock position into both the upstream and downstream (Fig. 1.2b,c). This entire turbulent region must be considered part of the shock, resulting in a very large shock width $L \gg 100\delta_{ci}$.

Dissipation in quasi-parallel collisionless shocks is provided by transverse magnetic fields in the form of waves generated by several electromagnetic ion/ion beam instabilities. These waves dissipate energy by scattering inflowing particles, thermalizing the initially cold beam distribution. Some wave energy is also transferred by beam instabilities into the core plasma, which is both accelerated and thermalized (together comprising heating). The large-amplitude waves can also act as magnetic mirrors, reflecting inflowing ions back into the upstream [94, 140].

The ions reflected by the shock penetrate far into the upstream, eventually giving up their energy through beam instabilities with the inflowing plasma. The result is an extended region of turbulent waves upstream of the shock called the foreshock (Fig. 1.2c) [33]. Throughout this region wave-particle scattering thermalizes both the inflowing and reflected ions, providing more dissipation [39]. Wave-particle interactions in this turbulent foreshock region results in a number of different ion populations that can be distinguished by their velocity distribution functions, including (among others) reflected ions, diffuse ions, and intermediate ions [15, 97]. These modified ion distributions are in turn unstable to more beam instabilities.

Most of the waves generated in the foreshock have a lower group velocity than the inflowing plasma and are therefore convected back towards, and eventually into, the shock. Some waves pass through the shock entirely: in the case of the Earth's bow shock, some waves reach the surface of the Earth [74]. The interaction of the waves with the shock modulates number of shock-reflected ions [110], creating a feedback loop that couples the shock and foreshock [17]. This process ultimately manifests as a cyclic reformation of the shock [16, 145, 110, 109]. The foreshock is therefore not separable from the shock transition, and must be considered as an integral part of the quasi-parallel shock system.

The large-amplitude waves created in the foreshock interact with one another (and with the foreshock ion populations via beam instabilities) through nonlinear processes to form a wide variety of foreshock structures. Examples include spontaneous hot flow anomalies

(SHFAs) [119, 94, 93], shockets [57, 108, 140], short large-amplitude magnetic structures (SLAMS) [124, 140], jets [65], and filaments [133, 60, 92]. The observation of various waves and foreshock structures are associated with the presence of different ion distributions [140, 142]. Understanding the formation and non-linear interactions between these waves and ion distributions is an essential part of understanding the structure and formation mechanisms of quasi-parallel shocks.

1.3 Scope of Dissertation

This dissertation presents the results of a recent series of experiments using laser-produced plasmas (LPPs) to drive beam instabilities relevant to quasi-parallel shock formation.

Chapter 2 (Theory) provides both a conceptual and an analytical overview of the linear theory that describes the growth of the electromagnetic ion/ion beam instabilities. Emphasis is placed on the way the instability growth rates and observed wave frequencies depend on the beam parameters, including for the experimentally-relevant case of heavy beam ions.

Chapter 3 (Experimental Setup) describes the physical setup of the experiments including the parameters of the core plasma, the specifications of the lasers used to produce the beam plasma, and descriptions of the diagnostics fielded.

Chapter 4 (Characterization of the Laser-Produced Plasma) describes measurements of the LPP, including the velocity distribution and density evolution. A variety of mechanisms that contribute to decreasing LPP density are evaluated and compared. A Monte-Carlo model for LPP density dispersion is used to predict the evolution of the density distribution.

Chapter 5 (Electromagnetic Wave Measurements) presents magnetic field measurements of waves generated by beam instabilities in the experiment. Wave parameters (polarization, frequency, wavelength) are determined and found to be consistent with predictions from linear theory. Measurements of the wave spatial structure are also presented. Results are compared to simulations of the experiment as well as measurements of ULF waves from the

terrestrial quasi-parallel foreshock.

Chapter 6 (Directions for Future Work) proposes several improvements that could allow future experiments to generate larger-amplitude waves or even a fully-formed quasi-parallel shock. Several possible measurements that could be made by an improved experiment are also proposed.

Chapter 7 (Conclusions) summarizes the results of this work.

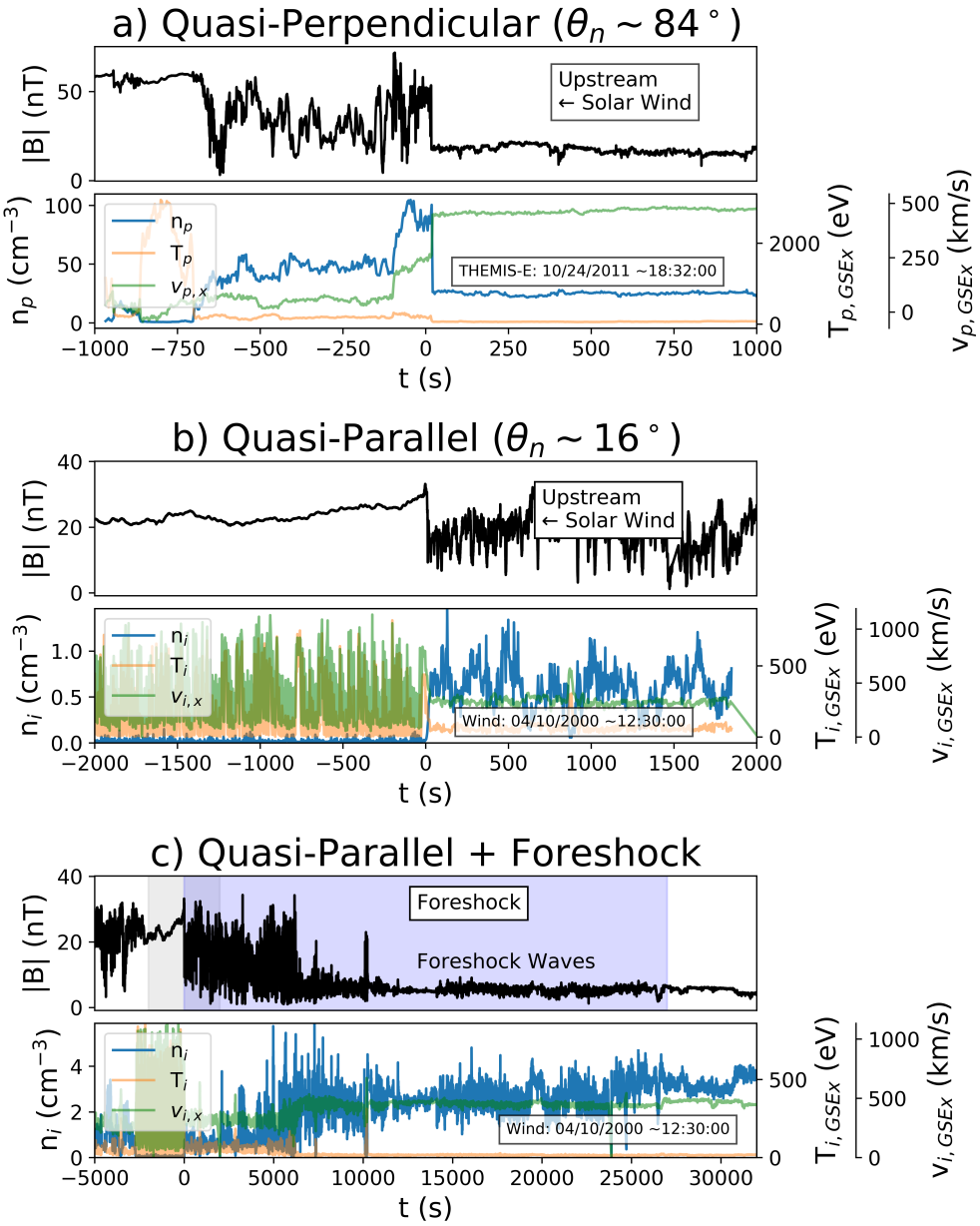

Figure 1.2: A comparison of magnetic field, ion density, ion velocity (along the Earth-Sun line, x_{GSE}), and temperature between two spacecraft crossings of the Earth's bow shock. a) shows a crossing of the quasi-perpendicular bow shock observed by THEMIS-E [4, 5, 138]. b,c) show a crossing of the quasi-parallel bow shock and foreshock (over different time scales) recorded by the Wind spacecraft [78, 82, 142]. The time axes are set such that $t = 0$ reflects the bow shock "crossing". The grey and blue shaded boxes in (c) denote the time region corresponding to (b) and the foreshock region respectively. Note that the plasma moment measurements are only of the bulk plasma and do not include other important ion populations such as field-aligned beams and diffuse ions. All data was downloaded from NASA's CDAweb.

CHAPTER 2

Theory

The growth of electromagnetic ion/ion beam instabilities, which occurs on kinetic spatial and temporal scales, plays a crucial role in the formation of quasi-parallel collisionless shocks. Sec. 2.1 develops a linear analytic theory to describe the growth of these instabilities and shows how they arise from anomalous cyclotron resonances with Doppler-shifted plasma waves. Sec. 2.2 investigates the dependence of these instabilities on plasma parameters and considers their relationship to other similar instabilities. Together, these theoretical results define the parameter design space for laboratory parallel shock experiments, which is discussed in Sec. 2.3.

2.1 The Collisionless Quasi-Parallel Shock Problem

A kinetic theory for the formation of quasi-parallel collisionless shocks must begin with an appropriate plasma distribution function. This distribution function must contain two separate populations of ions (of either identical or different species) with a relative drift velocity, along with their accompanying electrons. Since the dynamics of interest occur at ion scales, the two electron populations can be assumed for most purposes to effectively act as a single shared electron population. The resulting distribution function is called the three-component configuration [45], and is illustrated in Fig. 2.1. The less-dense and more-dense ion components are labeled the 'beam' ('b') and 'core' ('c') respectively, while the electrons are labeled 'e'.

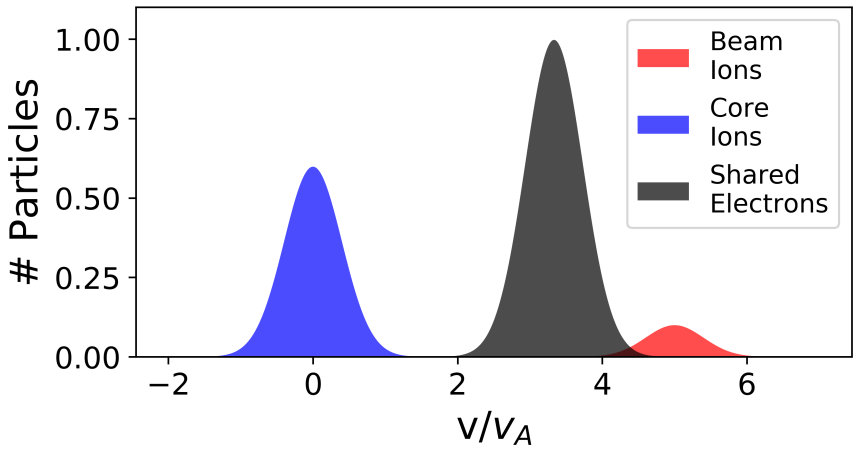

Figure 2.1: Example velocity distribution functions for the core ion, beam ion, and shared electron components in a three-component plasma configuration.

The three-component configuration can be unstable to a variety of beam instabilities, depending on the parameters of the plasmas. Some of these instabilities occur between two ion species (ion/ion instabilities), while others occur between one ion species and the electrons (electron/ion or current drift instabilities). Instabilities are further classified as either electrostatic or electromagnetic. Of this menagerie, electromagnetic ion/ion instabilities have the lowest growth rates, generally on the order of the ion cyclotron period. However, many of the faster-growing instabilities require and are sensitive to volatile conditions such as high temperatures or large velocity distribution anisotropy. Electromagnetic ion/ion instabilities extract their free energy from the relative ion/ion drift velocity, and are relatively insensitive to other plasma parameters. For this reason, despite their slow growth rate, electromagnetic ion/ion beam instabilities come to dominate in most quasi-parallel shocks [43].

The processes of shock formation and beam instability growth are inherently non-linear. A linear theory of either is therefore by definition an over-simplification. However, while shock formation requires non-linearity, the electromagnetic ion/ion beam instabilities can begin to grow in a linear regime. Studying this case provides some useful intuition for processes that are otherwise accessible only through numerical dispersion solvers and simulations. In some cases, such as in the far-upstream regions of quasi-parallel foreshocks where

reflected ion densities are low, this linear theory is surprisingly adequate.

2.1.1 Derivation of the Linear Cold Plasma Dispersion Relation

Motivated by the discussion of quasi-parallel shock formation in Chapter 1, we will search for electromagnetic instabilities of the three-component configuration that generate waves that propagate parallel to an ambient magnetic field at frequencies comparable to the ion cyclotron frequency. We define z to be the field-parallel direction, with k_z being the component of the wavenumber parallel to the field. Each species s has charge q_s, mass m_s, number density n_s, drift velocity v_s, and thermal velocity $v_{th,s}$. The plasma frequency is defined as $\omega_{ps}^2 = n_s q_s^2/\epsilon_0 m_s$ and $\omega_{cs} = q_s B_0/m_s$ is the cyclotron frequency.

We will begin with the dispersion relation for parallel wave propagation derived from the Vlasov and Maxwell equations for multiple species each with a Maxwellian velociy distribution by Stix [113] (Eq. 11.2-3 therein). These expressions can be rearranged as [45, 43]

$$\omega^2 - k^2c^2 + \sum_{s,m} \omega_{p,s}^2 \left(\zeta_s^0 Z(\zeta_s^m) + \frac{1}{2}(1 - T_\perp/T_\parallel) Z'(\zeta_s^m) \right) = 0 \tag{2.1}$$

where ω is the complex frequency, Z is the plasma dispersion function [37], $m \in \mathbb{Z}$, and ζ_s^m is the cyclotron resonance condition

$$\zeta_s^m = \frac{\omega - k_z v_{z,s} + m\Omega_s}{\sqrt{2} k_z v_{th,s}} \tag{2.2}$$

sometimes abbreviated as ζ for brevity. A species s is exactly in wave-particle resonance when

$$\mathbb{R}e(\zeta_s^m) = 0 \tag{2.3}$$

however, substantial energy can be transferred when waves and particles are *near* resonance,

so a broader definition of resonance is appropriate [45, 137]

$$|\mathbb{R}e(\zeta_s^m)| \leq 1 \tag{2.4}$$

Correspondingly, non-resonance is defined as $|\mathbb{R}e(\zeta_s^m)| > 1$. ζ_s^m with $m = 0$ corresponds to Landau wave-particle resonance, while $m \neq 0$ corresponds to wave-particle gyroresonances of which only $m = \pm 1$ are significant for parallel propagating waves [45].

Following Stix, we can simplify Eq. 2.1 by assuming the plasma to be cold ($v_{th,s} \ll v_s$), which corresponds to the limit $\zeta_s^m \gg 1$. For shocks in space this is generally a reasonable approximation for the electron and core species, but a very poor one for the hot beam plasma. Luckily, the relative insensitivity of the instabilities of interest to the ion temperatures ultimately makes this assumption acceptable. The limit can be taken using an asymptotic expansion of $Z(\zeta)$ for large ζ [37]

$$Z(\zeta) \approx i\pi^{1/2}\sigma e^{-\zeta^2} - \zeta^{-1}\left(1 + \frac{1}{2}\zeta^{-2} + \frac{3}{4}\zeta^{-4} + ...\right) \tag{2.5}$$

where σ is a piecewise function of ζ. This expression is valid over all frequencies, but it can be truncated by considering only the frequency range near the first gyroresonance at $m = 1$. This is a local minimum of ζ, and we can therefore neglect all but the first order term in Eq. 2.5, leaving

$$Z(\zeta) = -\frac{1}{\zeta} \tag{2.6}$$

Since it is always true that $Z' = -2(1+\zeta Z)$ (Stix Eq. 10.66), in this limit it is also true that $Z' = 0$. Note that this limit removes the temperature dependence without assuming temperature isotropy, so the following solutions are valid for $T_\perp \neq T_\parallel$. The simplified dispersion relation is then (Stix Eq. 11.5-6)

$$\omega^2 - k^2c^2 - \sum_s \omega_{p,s}^2 \frac{\omega - k_z v_{z,s}}{\omega - k_z v_{z,s} \pm \Omega_s} = 0 \tag{2.7}$$

In order to work with dimensionless variables, we normalize the charge, mass, gyrofrequency, and plasma frequency of each species to the core plasma values. Velocities are normalized to the core Alfvén velocity, and wavenumbers are multiplied by the core ion inertial length $\delta_{i,c} = c/\omega_{p,c}$. The frequencies for each species can then be expressed as $\Omega_s = (q_s/m_s)\Omega_c$ (note that $\Omega_e < 0$) and $\omega_{p,s}^2 = (n_s q_s^2/m_s)\omega_{p,c}^2$. The number densities are normalized to the electron density such that

$$n_e = \sum_{s \neq e} n_s = 1 \tag{2.8}$$

The resulting dimensionless equation is

$$\frac{\omega^2}{\omega_{p,c}^2} - k^2 - \sum_s \frac{n_s q_s^2}{m_s} \frac{\omega - k v_s}{\omega - k v_s \pm \Omega_s} = 0 \tag{2.9}$$

Clearing the denominator (allowable even at resonance, where $\mathbb{R}e(\zeta_s^m) = 0$, because in that region $\mathbb{I}m(\zeta_s^m) \neq 0$) the equation becomes

$$\left(\frac{\omega^2}{\omega_{p,c}^2} - k^2\right) \prod_s (\omega - k v_s \pm \Omega_s) - \sum_s \frac{n_s q_s^2}{m_s} (\omega - k v_s) \prod_{s' \neq s} (\omega - k v_{s'} \pm \Omega_{s'}) = 0 \tag{2.10}$$

The electron density can be eliminated from this equation using Eq. 2.8. A velocity may also be eliminated by choosing a co-moving reference frame. The electron frame, where $v_e = 0$, is a convenient choice. Another velocity may be eliminated by assuming the plasma to be current-free

$$\sum_s q_s n_s v_s = 0 \tag{2.11}$$

which, along with $v_e = 0$, leads to the requirement

$$v_c = \frac{q_b}{q_c} \frac{n_b}{1 - n_b} v_b \tag{2.12}$$

For the purpose of Doppler shifting between frames, it is useful to note that the velocity of

the electron rest frame relative to the core ion rest frame is

$$v_e = q_b n_b v_b \tag{2.13}$$

The electron term of Eq. 2.10 can be further simplified by taking the cold electron limit

$$|\Omega_e| \gg \omega - k v_e \tag{2.14}$$

With these simplifications, the dispersion relation for the three-component configuration near the $m = +1$ resonance can be written

$$\begin{aligned}
&\left(\frac{\omega^2}{\omega_{p,c}^2} - k^2\right)(\omega - k v_c + \Omega_c)(\omega - k v_b + \Omega_b) \\
&- \frac{n_b q_b^2}{m_b}(\omega - k v_b)(\omega - k v_c + \Omega_c) \\
&- n_c(\omega - k v_c)(\omega - k v_b + \Omega_b) \\
&- n_e q_e \frac{\omega - k v_e}{\Omega_c}(\omega - k v_c + \Omega_c)(\omega - k v_b + \Omega_b) \\
&= 0
\end{aligned} \tag{2.15}$$

It is sometimes useful to consider the simpler case of a stationary single-species plasma with ions (i) and electrons (e). The dimensionless dispersion relation for this case can be obtained from Eq. 2.9 with $s \in i, e$.

$$\frac{\omega^2}{\omega_{p,i}^2} - k^2 - \frac{\omega}{\omega \pm 1} - \frac{\omega_{p,e}^2}{\omega_{p,i}^2}\frac{\omega}{\omega \pm \Omega_e} = 0 \tag{2.16}$$

where the upper and and lower signs correspond to the whistler and ion cyclotron waves respectively. At low frequencies ($\omega \ll \Omega_i$) this equation approaches the Alfvén wave dispersion relation $\omega = k|v_A|$. In practice it is often convenient to recover Eq. 2.16 from Eq. 2.15 by setting $n_b = v_b = v_c = 0$ and $n_c = n_e = 1$.

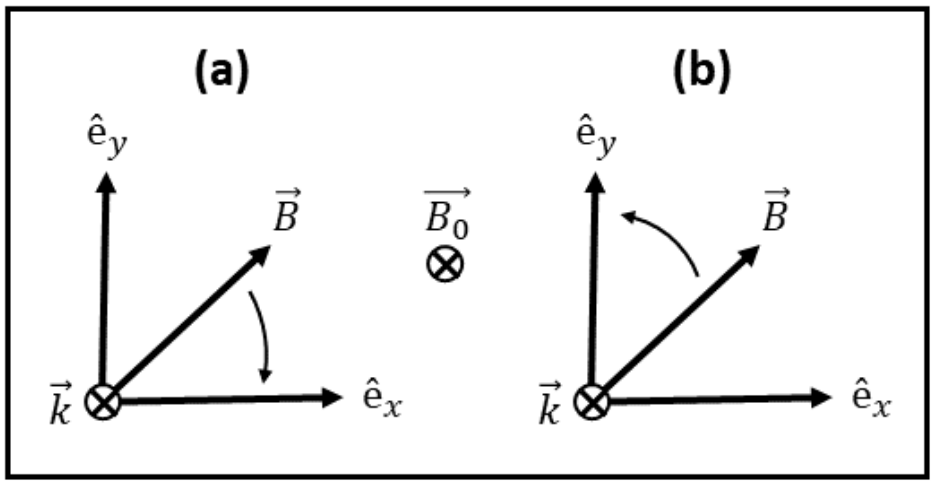

Figure 2.2: Clockwise (a) and counter-clockwise (b) rotating magnetic field vectors are classified as either right-handed or left-handed based on one of several conventions.

2.1.2 Common Characteristics of Dispersion Relation Solutions

Both the single-species dispersion relation (Eq. 2.16) and the three-component dispersion relation (Eq. 2.15) admit complex wave solutions of the form

$$\omega = \omega_r + i\gamma \tag{2.17}$$

where ω_r is the wave frequency and γ is its growth rate. Solutions with $\gamma > 0$ represent instabilities (growing in time), solutions with $\gamma < 0$ are damped, and solutions with $\gamma = 0$ are steady-state.

2.1.3 Defining Wave Polarization

All parallel-propagating wave solutions are circularly polarized (non-circular polarization is possible only for obliquely propagating waves), and the handedness of their polarization provides a useful means of comparing experimental measurements to theoretical predictions. The signs of the real frequencies in the derivation in Sec. 2.1.1 are chosen such that the

polarization is

$$P = \frac{\omega_r}{|\omega_r|} \tag{2.18}$$

where $P = +1$ is defined as right-hand circularly polarization (RCP) and $P = -1$ as left-hand circular polarization (LCP). Physically, the polarization of a wave is defined by the sense of rotation of its electric or magnetic field vector, which can be determined by comparing the phase of the different field components. However, the sense of the vector's rotation depends on the viewer's point of view (POV), leading to several competing conventions:

- **Source POV:** Defined from the perspective of an observer at the source looking along the direction of wave propagation parallel to k, RCP waves rotate clockwise and LCP waves counter-clockwise. This perspective is illustrated in Fig. 2.2 for RCP (a) and LCP (b) waves respectively.

- **Observer POV:** Defined from the perspective of an observer in the path of the wave, looking back towards the source anti-parallel to k, RCP waves rotate counter-clockwise and LCP waves rotate clockwise. This is the reverse of the previous convention, and is commonly adopted in optics.

- **B-Field Aligned POV (plasma physics):** RCP is defined to be rotation in the same direction as a gyrating electron. Under this convention, the polarization depends on the direction of the background field relative to k. Defined from the perspective of an observer looking parallel to the background magnetic field (as illustrated in Fig. 2.2), RCP waves rotate clockwise, and LCP waves counter-clockwise.

This last convention is commonly used in the literature on quasi-parallel shocks [45], and is therefore adopted here. When waves propagate anti-parallel to the background magnetic field, as is the case in the LAPD shock experiments, this convention therefore defines RCP as clockwise rotation when viewed parallel to the field, or counter-clockwise when viewed anti-parallel to the field.

The handedness of a circularly polarized wave under any of these conventions also depends on the reference frame from which it is viewed. If the same wave is viewed from two reference frames in which its phase velocity has opposite sign, the perceived sense of rotation (and therefore polarization) will also be reversed. An important example of this is the waves generated by the Right-Hand Resonant Instability (Sec. 2.1.5), which are LCP in the electron rest frame but RCP when observed in the rest/spacecraft frame. For this reason it would in theory be preferable to identify wave modes using the handedness of their rotation in space rather than time, because the former is frame-invarient. This quantity is called the helicity, and is defined to be [43]

$$\sigma = \frac{k_z}{k} \tag{2.19}$$

where $\sigma = +1$ corresponds to left-handed helicity, and $\sigma = -1$ to right-handed helicity. In situations where the spatial structure of the wave is equally or better known than the temporal structure (for example, in a simulation), this is a more convenient method for identifying wave modes. However, in the case of many spacecraft or laboratory time series measurements, only the polarization can be determined and must therefore be used by necessity.

2.1.4 Wave Solutions to the Single-Species Dispersion Relation

Before looking for instabilities in the three-component configuration (Eq. 2.15) it is instructive to examine the stable wave solutions to the single-species dispersion relation (Eq. 2.16). These solutions are plotted in the plasma rest frame (in this case equivalent to the electron rest frame) in Fig. 2.3.

The two solutions to the dispersion relation correspond to four wave modes representing RCP or LCP waves propagating either parallel or anti-parallel to the ambient field. At low frequencies ($\omega \approx 0$) all four waves approach the Alfvén wave dispersion relation $\omega = k|v_A|$. At higher frequencies the RCP wave approaches the whistler dispersion relation while

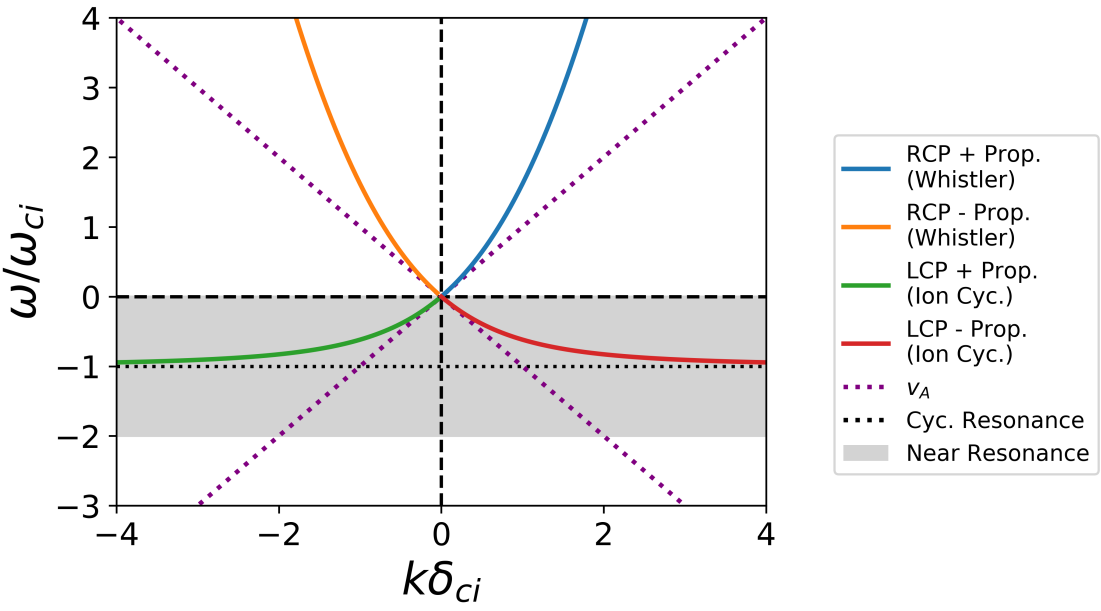

Figure 2.3: Four non-trivial waves emerge as solutions to the cold plasma dispersion relation in a single-species plasma (Eq. 2.16). These correspond to RCP (whistler) and LCP (ion cyclotron) waves propagating parallel (right, +) and anti-parallel (left, −) along the field. Waves within the band $\omega/\omega_{ci} = -1 \pm 1$ are cyclotron resonant with the ions.

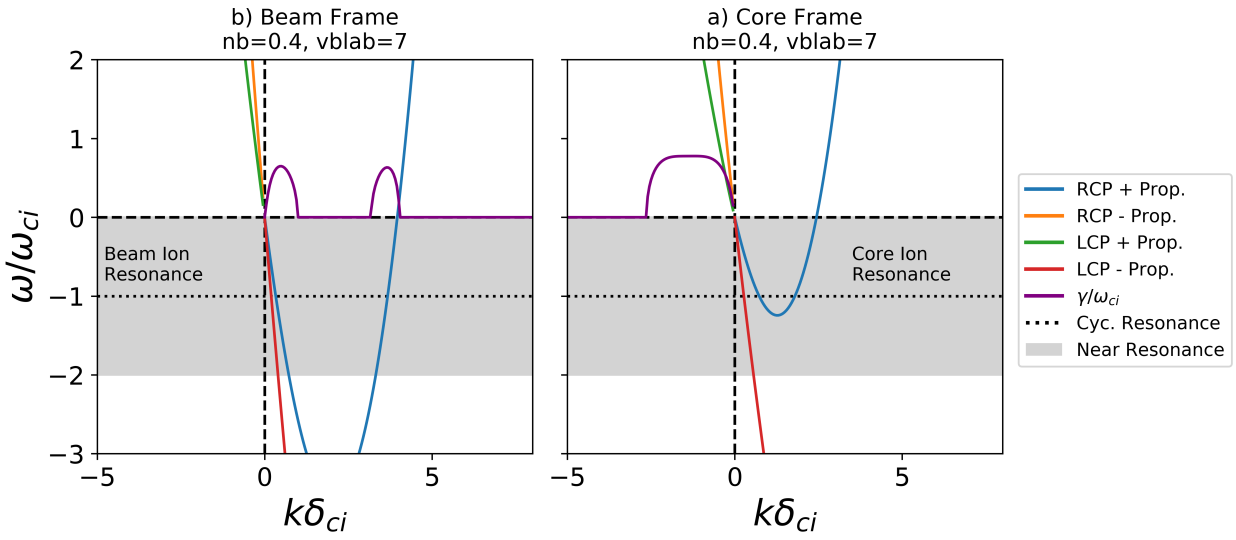

Figure 2.4: Wave dispersion relation solutions calculated in the electron rest frame are Doppler-shifted into the beam ion (a) and core ion (b) reference frames. In both cases, RCP waves that would not typically be resonant with the ions are Doppler-shifted into the near-resonant band. For the purpose of illustration, the curves plotted are solutions to the single-plasma dispersion relation rather than the three component dispersion relation. The solutions to the three component dispersion relation are almost identical but are more prone to numerical artifacts.

the LCP wave approaches the ion cyclotron wave dispersion relation (Eq. 2.16). The ion cyclotron waves are always partially resonant with the ions and become strongly resonant at $\omega/\omega_{ci} = -1$, corresponding to cyclotron damping. The RCP waves are not resonant with the ions and propagate freely. Other wave modes, such as the lower hybrid wave, do not appear under the approximations made in Sec. 2.1 but are treated elsewhere [35].

2.1.5 Instability Solutions

In the electron rest frame (ERF), the wave solutions to the three-component configuration dispersion relation (Eq. 2.15) with beam and core ions of the same species remains approximately identical to those found for the single-species plasma. However, the two ion species now have non-zero drift velocities in the electron rest frame, and so the Doppler shift term in the resonance condition (Eq. 2.2) now allows unstable wave-particle resonances. These

resonances lead to instability solutions with $\gamma > 0$.

These resonant processes are most easily understood by viewing the dispersion relation solutions in the rest reference frames of the two ion components. The dispersion relation viewed from the beam ion and core ion reference frames for a beam density of $n_b = 0.4$ and a lab frame beam velocity $v_b = 7$ are shown in Fig. 2.4. In the beam ion frame (Fig. 2.4a), the RCP parallel-propagating wave (blue) has been Doppler shifted far enough that parts of the curve are within the near-resonant zone. These areas of the curve correspond to a gyroresonant instability with the beam ions, resulting in a non-zero growth rate γ (purple) in this region. In the example shown the beam current is so large that part of the curve is Doppler shifted past the near-resonant zone, leaving a region of stability between two instabilities. At lower beam currents these two peaks would merge together.

The instability represented by the peak closest to $k = 1$ is called the Right Hand Resonant Instability (RHI) because the waves it generates are RCP and parallel propagating in the core plasma reference frame. As the beam current increases and the peaks bifurcate this peak remains near $k \sim 1$. The second peak at $k > 1$ is called the Electron/Ion Whistler Instability [2], and is an electron/ion current instability made further unstable by the addition of the core ions. As the beam current continues to increase, the Electron/Ion Whistler Instability peak runs away to $k \to \infty$.

A nearly symmetric process occurs in the core ion rest frame, illustrated in Fig. 2.4b. In this case, the backwards-propagating RCP wave is Doppler shifted into resonance with the core ions, leading to a second resonant instability and corresponding growth rate $\gamma > 0$. At the parameters shown a single instability is observed, but this peak will also bifurcate given sufficient beam current. This process is strikingly similar to the instability observed in the beam frame, but the cases are not exactly symmetric unless $n_b = 0.5$. In the typical case where $v_b > v_c$, the Doppler shift from the ERF to the beam ion rest frame is always larger than the Doppler shift from the ERF to the core ion rest frame. In any case, Doppler shifting the problem to the core ion rest frame where measurements are typically made obscures the

quasi-symmetry.

This instability is called the Non-Resonant Instability (NRI) [144, 43]. This name is a historical misnomer, and recent work consistent with the explanation presented here has shown this instability to also be resonant [137, 136]. The waves generated by the NRI are RCP and backwards propagating in the electron rest frame, but appear LCP and forward propagating when observed in the core ion rest frame. The maximum NRI growth rate always remains near $k \sim -1$. At higher beam velocities this peak also bifurcates [137] to form a second instability which also runs away to $k \to -\infty$.

2.1.6 Relationship to Other Instabilities

The names RHI and NRI are conventional in space physics, but similar instabilities are known by different names in other fields. Bell's instability [9] is often discussed in the context of astrophysical shocks, and is a special case of the NRI [136]. Gyroresonant instabilities similar to the RHI and NRI have also been observed in magnetic mirror devices [42, 23]. The Left-Hand Resonant Instability (LHI) observed in space physics is a special case of the RHI driven in hot beams ($v_{th} \gg v_b$) in which a sufficient number of fast ions move opposite to the beam's drift velocity ("backwards") and excite waves that are LCP in the core ion rest frame [43].

A set of modified versions of these instabilities occur either when the beam drift velocity is oblique or when the beam temperature is hot and highly anisotropic [41]. These configurations are closely related because a hot highly anisotropic beam contains obliquely moving particles. Similar waves have been observed to be driven by neutral ion beams in tokamaks, where the RHI and NRI are comparable to Compressional Alfvén Eigenmodes [59, 10] and Global Alfvén Eigenmodes [81] respectively.

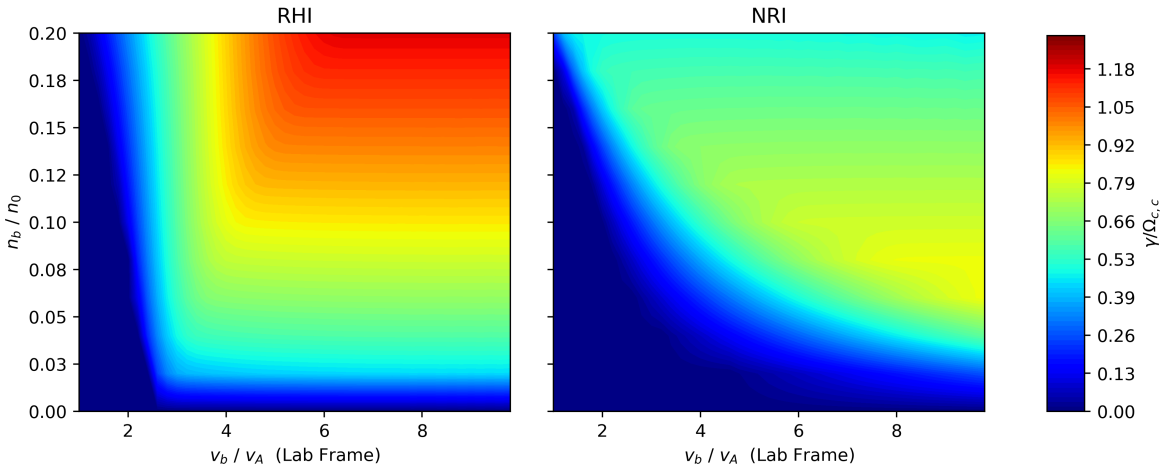

Figure 2.5: Growth rates for the RHI and NRI as a function of beam ion velocity and density. These growth rates are calculated for C^{+4} beam ions and He^{+1} core ions.

2.2 Beam Instability Properties

The properties of the waves and beam instabilities described in Sec. 2.1 depend on the plasma parameters of the beam and core ions. In particular, the beam instability growth rates depend strongly on the density and velocity of the beam ions relative to the core ions (Sec. 2.2.1). The instability growth rates also depend on the charge and mass of the two ion species, as do the frequencies and wavelengths of the waves that they generate (Sec. 2.2.2).

2.2.1 Dependence of Instability Growth Rates on Beam Parameters

The growth rates of both the RHI and the NRI depend strongly on the density and velocity of the beam ions relative to the core ions. A study of the dependence of the RHI and NRI growth rates on these parameters up to $n_b/n_0 = 0.2$ is presented in Fig. 2.5. The RHI has a sharp onset at a Mach number cutoff of $M_A \sim 2$ that is relatively consistent across beam densities higher than a few percent. The RHI growth rate in this limit can be analytically calculated to be [42]

$$\frac{\gamma_{RHI}}{\Omega_{c,c}} = \left(\frac{n_b}{2n_0}\right)^{1/3} \tag{2.20}$$

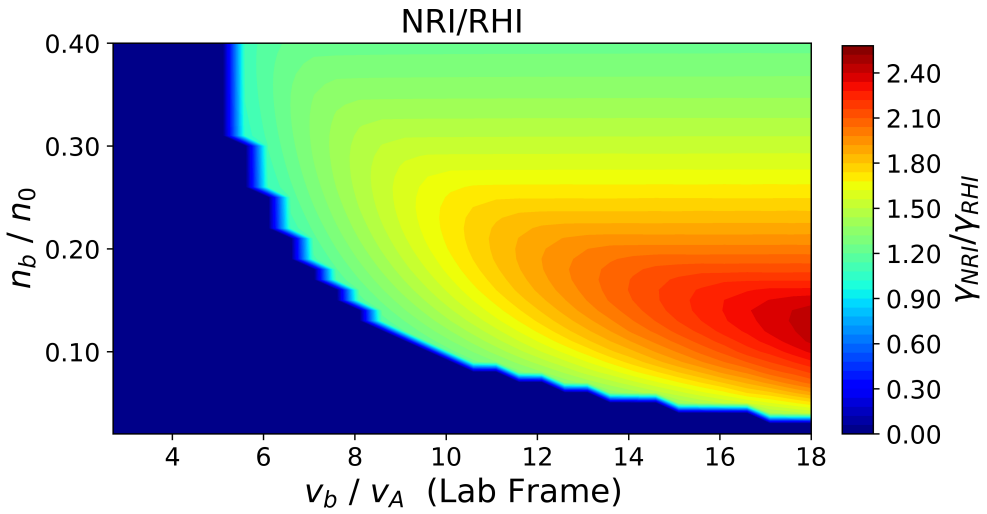

Figure 2.6: The ratio between the NRI and RHI growth rates plotted over a wide range of parameters to show the requirements for the NRI to become dominant. These growth rates are calculated for a proton beam and a proton core. Linear steps along the transition are a numerical artifact of the finite grid resolution in parameter space.

Above $M_A \sim 4$ (for these parameters), the RHI growth rate becomes approximately independent of Mach number. The NRI has a higher density and velocity onset threshold than the RHI, but otherwise has a lower overall growth rate over this region of parameter space. Eventually, at much higher Mach numbers, the NRI becomes dominant (Fig. 2.6) [137, 136].

Since these growth rates are derived from Eq. 2.15, they carry an implicit cold-beam assumption. Similar calculations for warm beams have been carried out numerically [137], and define the bounds for which these assumptions are acceptable. Over a range of beam temperatures v_A/v_{th} from $0-1$ the RHI growth rate remains unchanged while the NRI growth rate is slightly decreased. The maximum growth rate of both instabilities remains constant. Over the same range, the Electron/Ion Whistler Instability growth rate decreases by a larger amount, and its maximum growth rate moves slightly towards lower k. At much higher temperatures ($v_A/v_{th} \sim 10$) the RHI and NRI growth rates are significantly smaller and no longer resemble the linear solutions. It is therefore safe to conclude that the cold-beam approximation is acceptable as long as $v_A/v_{th} \gtrsim 1$.

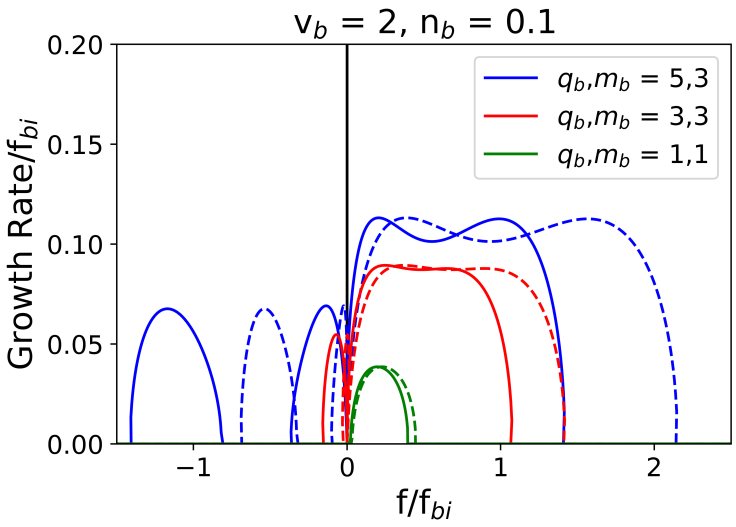

Figure 2.7: Growth rates as a function of frequency (normalized to the beam ion cyclotron frequency f_{bi}) are plotted for several different beam ion species in both the electron rest frame (solid lines) and the core ion rest frame (dashed lines).

2.2.2 Dependence on Ion Species

Most of the examples presented here have used beam and core ions of the same species for simplicity. This situation is common in space, where both beam and core ions are typically protons. However, the laboratory experiments described in this manuscript utilize beam ions with higher atomic masses and charge states than the core ions. This same situation is also occasionally found in space, such as at cometary bow shocks [44]. In this case the growth rates predicted by linear theory are modified, and the waves generated will be of higher frequency.

Unfortunately, the dependence of the growth rate and wave frequency cannot be simply compensated for by scaling the results to a dimensionless quantity such as the core or beam ion cyclotron frequency. Both the wave frequency and the growth rate depend on the ratio of the charge, mass, and density of the beam ions to the corresponding core ion quantities. However, as seen in Eq. 2.15, these ratios cannot be factored into ω, so no simple scaling of the frequency as a function of these parameters is possible.

In the electron rest frame, cases with different charge/mass ratios have different solutions, even when scaled to f_{bi}, which is a consequence of the q_b^2/m_b term in Eq. 2.15. This difference is even more pronounced when the results are Doppler shifted to the core ion rest frame, since this introduces a further dependence on the charge, density, and velocity of the ions as shown in Eq. 2.13. This fact is illustrated in Fig. 2.7. Laboratory experiments with heavier, more highly charged ions than protons will therefore produce considerably higher frequency waves than those observed in space. Depending on the time scales of the experiment and the frequency sensitivity of the available diagnostics this effect may be disadvantageous or beneficial.

2.3 Theoretical Constraints on the Design of Laboratory Quasi-Parallel Shock Experiments

The theoretical results presented in this chapter determine the conditions required for the growth of the electromagnetic beam instabilities necessary to form a parallel shock. Achieving these conditions in a laboratory experiment is a challenging endeavor. A super-Alfvénic ($M_A \sim 10$) beam plasma must overlap a 5-10 times denser core plasma over a length of hundreds of ion-inertial lengths to allow sufficient time for the instabilities to grow and interact to form a shock. Simulations provide more specific guidance, suggesting that > 500 ion-inertial lengths are required [135]. The core plasma density must be high enough to fit this many ion-inertial lengths in the experimental apparatus, but low enough that Coulomb collisions remain negligible over that same distance. The background magnetic field must be strong enough to magnetize both plasmas on the time scale of the experiment but low enough that the beam satisfies the Mach number requirement. The usual magnetization criterion, $\nu_{bi,ci} \ll f_{ci}$ where $\nu_{bi,ci}$ is the beam ion/core ion Coulomb collision frequency and f_{ci} is the ion cyclotron frequency, is here a necessary but insufficient condition. Beam instability growth and subsequent quasi-parallel shock formation require many ion gyroperiods (f_{ci}^{-1}), leading

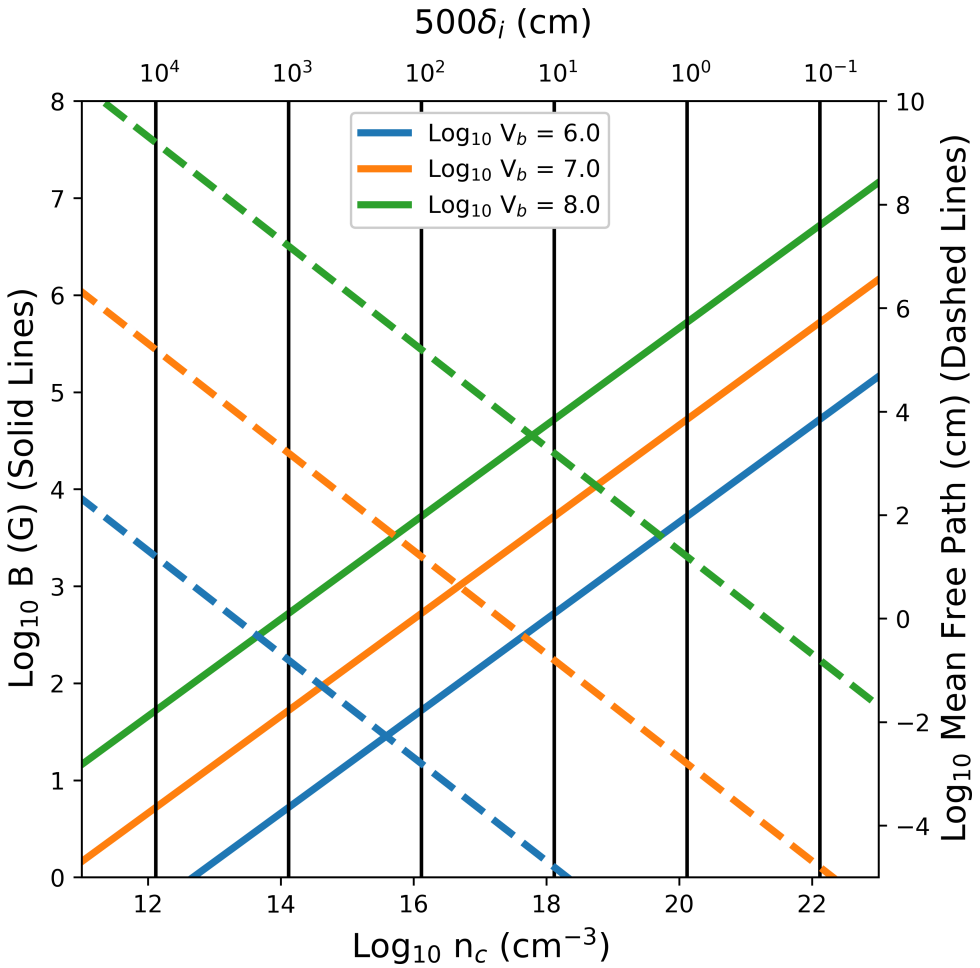

Figure 2.8: Required background magnetic field (solid lines) to maintain $M_A = 10$ for different beam velocities (v_b in cm/s, line colors) as a function of core density (n_c in cm^{-3}) calculated for proton beam and core plasmas. The beam-ion/core-ion mean free path for each beam velocity (dashed colored lines) and the physical length of a $L = 500\delta_i$ experiment at several densities (black lines) are overplotted for comparison.

to the usually more stringent condition $v_b/L \ll f_{ci}$. Studying these processes also requires that the ion gyroperiod and ion-inertial length must be well-resolvable by diagnostics. These competing conditions have yet to be simultaneously realized in an experiment.

Consider a laboratory experiment constituting a magnetized proton core plasma at rest in the lab frame and a less dense proton beam plasma streaming parallel to the ambient field. Assuming a practical system length upper limit of $L = 10^3$ cm for a laboratory experiment implies that a minimum core density of $n_c \geq 10^{14}$ cm^{-3} is required for a parallel shock to form ($\sim 500\delta_i$). At this density the core plasma will be collisional. However, for a beam velocity of $v_b \geq 10^7$ cm/s, the beam ion/core ion collisional mean free path $\lambda_{bi,ci}$ is much larger than L. This is possible because $\lambda_{bi,ci} \propto |v_b - v_c|^4$ [77]. Satisfying the condition that $M_A \geq 10$ for this beam velocity and core density requires a background magnetic field of $B_0 \leq 100$ G (Fig. 2.8).

A similar experiment could be conducted at smaller length scales and higher densities: an $L = 1$ cm experiment would require a core density of 10^{20} cm^{-3}. In order to maintain $L < \lambda_{bi,ci}$, such an experiment would require $v_b \sim 10^7$ cm/s. Maintaining $M_A = 10$ at this beam velocity would require a background field of $B_0 \sim 10 - 50$ T (Fig. 2.8).

The ideal beam plasma for a laboratory quasi-parallel shock experiment would be spatially and temporally uniform with a density $n_b/n_c \sim 10\%$ and with no magnetic structure comparable to the ambient magnetic field strength. Electrostatic ion accelerators provide a uniform beam, but producing an ion beam with 1% of even the lowest core densities discussed above with such an accelerator is challenging. Bursts of plasma such as spheromaks [73] and field-reversed configurations [112] can be sufficiently dense and fast, but have substantial internal magnetic fields that may perturb the quasi-parallel field geometry. Laser-produced plasmas (LPPs) can be produced with densities and velocities in the desired range [104]. Significant magnetic fields are created near the target [25], but most of the fast LPP ions escape this region into the relatively unperturbed ambient magnetic field. These characteristics make LPPs attractive drivers for laboratory quasi-parallel collisionless shock experiments.

CHAPTER 3

Experimental Setup

In the experiments described in this manuscript, electromagnetic ion/ion beam instabilities are generated by the interaction of a magnetized core plasma and a super-Alfvénic but less dense laser-produced plasma (LPP) beam. The core plasma is created by the Large Plasma Device (LAPD) at UCLA (Sec. 3.1) [46, 47]. The beam is a laser-produced plasma (LPP) ablated by one of two lasers (Sec. 3.2) from a plastic target embedded in the core plasma. The LPP is directed along the target surface normal, and the target surface is oriented such that the bulk LPP velocity is anti-parallel to the background magnetic field. This orientation is chosen as a matter of experimental convenience: the beam instability and shock formation theory in this geometry is identical to the field-parallel case. A variety of diagnostics are used to characterize both plasmas and to measure the resulting waves (Sec. 3.3).

A Cartesian experimental coordinate system is defined such that the positive z-axis is aligned with the background magnetic field (Fig. 3.1). The positive y-axis is chosen to be parallel to the laser target, and the x-axis is defined to complete a right-handed coordinate system. The spatial and temporal origins are defined such that the laser hits the target at $(x,y,z) = (0,0,0)$ and $t = 0$.

3.1 Core Plasma: The Large Plasma Device

The LAPD [46, 47] produces a cylindrical plasma column 20 m long and approximately 40 cm in diameter with a variable axial magnetic field of 0.2-1.8 kG. The chamber can be filled

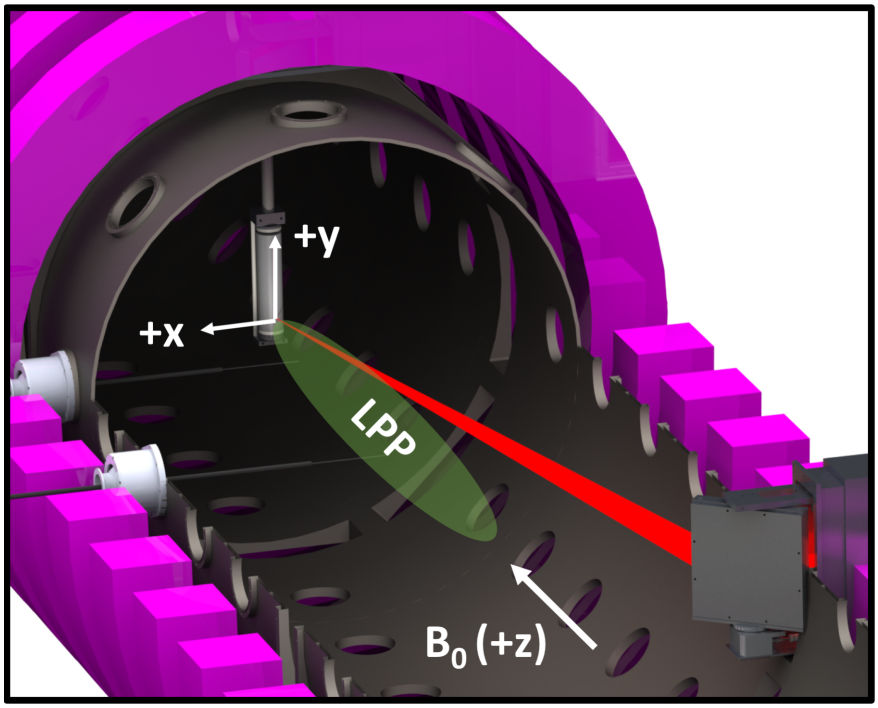

Figure 3.1: A diagram of the experimental setup near the laser target that defines the experimental coordinate system.

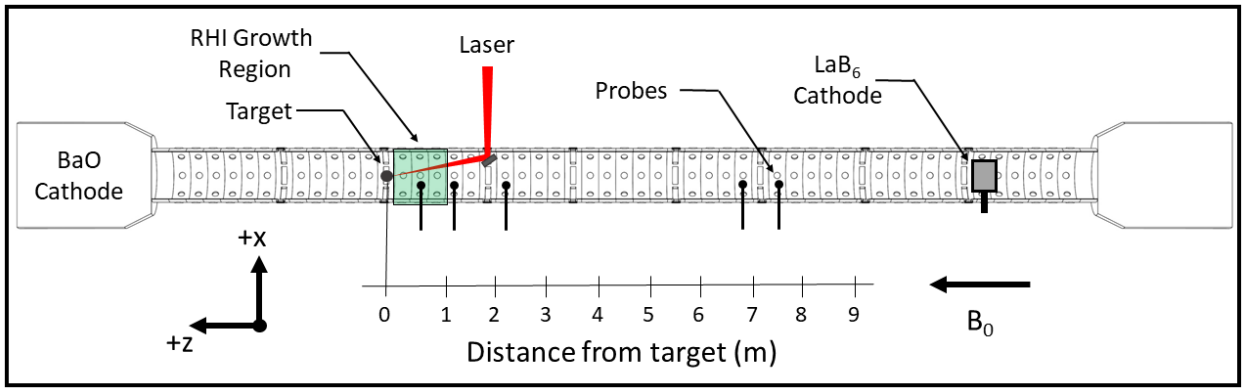

Figure 3.2: A diagram of the entire experiment, showing the relative placements of the LAPD cathodes, the laser target, and some example probe locations. The RHI grows in the shaded region (Sec. 5.4.1).

Parameter	Symbol	Typical Value
Magnetic Field	B_0	300 G
Dominant Plasma Species	-	He^{1+}
Density	n_c	10^{13} cm^{-3}
Electron Temperature	T_e	5 eV
Ion Temperature	T_i	1 eV
Ion Cyclotron Frequency	f_{ci}	114 kHz
Alfvén Velocity	v_A	100 km/s
Ion Inertial Length	δ_i	15 cm
Debye Length	λ_D	5 μm
Thermal/Magnetic Pressure Ratio	β	10^{-3}

Table 3.1: Typical LAPD plasma parameters for these experiments.

with various low pressure gases (H, He, Ne, etc.). The gas is almost completely ionized by thermionic emission at two concentric cathodes positioned at opposite ends of the vacuum chamber. Unless otherwise specified, the experiments described here were performed in a helium plasma with a background magnetic field of $B_0 = 300$ G. A list of these parameters and the corresponding values of some common plasma physics constants is shown in Table 3.1.

The main discharge is driven by a circular barium oxide (BaO) coated cathode 60 cm in diameter. This plasma is relatively low density ($n_e \sim 10^{12}$ cm^{-3}). The second source is a 20 cm $\times$ 20 cm square lanthanum hexaboride (LaB_6) cathode that produces a higher density plasma ($n_e \sim 10^{13}$ cm^{-3}). Mesh anode grids positioned in front of both cathodes collect the thermionic electrons. Experiments are performed in the current-free region between the anodes. The plasma is initiated by the BaO cathode, which aids the breakdown of the LaB_6 cathode. The density remains at its maximum value (with both cathodes on) for several milliseconds, providing a stable and quiescent plasma on the 100 μs time scale of the experiment. Both cathodes can be pulsed at up to 1 Hz, producing a highly repeatable plasma.

Parameter	200 J (Raptor)	15 J (Peening)
Max. Energy	200 J	15 J
Pulse Length	35 ns	15 ns
Shot rate	1 / 45 min.	1 / s
Beam Width	10 cm	4 cm
Spot Width	3 mm	60 um
f/N	34	86
Nominal Intensity	10^{10} W/cm^2	10^{13} W/cm^2

Table 3.2: A comparison of typical parameters for the Raptor and Peening lasers.

3.2 Beam Plasma: The Phoenix Laser Laboratory

The Phoenix Laser Laboratory is a high-energy laser facility at UCLA that operates two lasers used in this series of experiments (Sec. 3.2.1). For a given experiment, one of the two beams is transported down to the LAPD chamber as a collimated beam. The beam is then brought to a focus by a 3.44 m lens outside of the LAPD vacuum chamber. After entering the chamber through an anti-reflection coated window, the beam is reflected by a final steering mirror (Sec. 3.2.2) onto the target (Sec. 3.2.3).

3.2.1 Lasers

The Raptor laser is a 200 J, 1053 nm Nd:glass laser with a typical pulse length of 35 ns and a shot cycle of 45 minutes [89]. The spot size on target is limited to a diameter of ≥ 3 mm by the intensity threshold of stimulated Brillouin scattering (SBS) from the LPP which, if exceeded, would scatter sufficient energy back into the laser amplifiers to damage them. The resulting nominal intensity on target is very low. However, experimentally determined scaling relations [53] based on debris velocity imply that the intensity is actually much higher, on the order of 10^{12} W/cm^2. This discrepancy is likely due to hot spots in the beam with much higher than nominal intensity. If so, these hot spots are likely responsible for creating the fast ions studied in these experiments.

The Peening laser is a 15 J, 1053 nm Nd:glass laser with a typical pulse length of 15 ns.

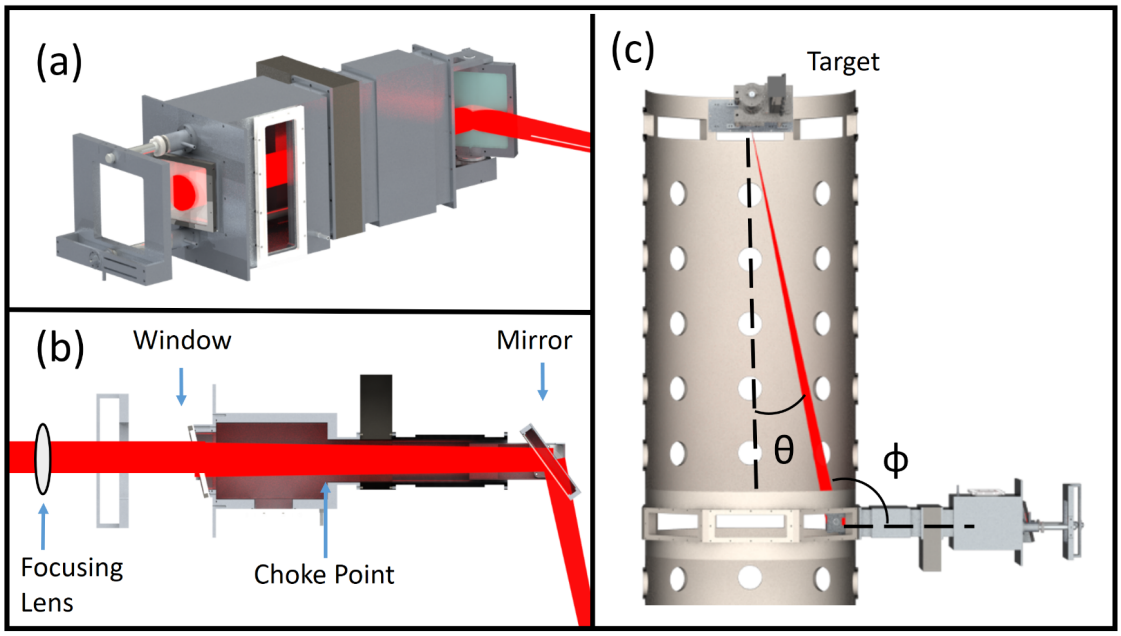

Figure 3.3: Three views of the final laser beam transport and steering interior mirror assembly: a) exterior, b) cross-section, and c) top-down with LAPD and target.

The Peening laser uses a unique design [56] to achieve a shot repetition rate of 1 Hz at these parameters. This design also inherently protects Peening against SBS backscatter, allowing it to be focused to a diffraction-limited spot on target. As a consequence, despite its lower energy, Peening is capable of achieving intensities (and therefore LPP velocities) comparable to Raptor.

3.2.2 Beam Transport

Creating a field-parallel LPP in the LAPD required the development of an assembly to position a final laser steering mirror inside the vacuum chamber. The mirror assembly is attached to the LAPD and brought to vacuum while within a large pumpdown box before being pushed into position. Once in place, the mirror is rotated using a 90:1 geared rotation stage to precisely position the beam on the target. In order to minimize the number of optics inside the vacuum chamber, the final focusing lens ($\sim$ 18 cm diameter, $f_L = 3.4$ m focal length, f/N $\sim$ 34) is placed immediately before the laser entrance window. The outside

surface of this window is coated with an anti-reflective coating and is angled by $\sim 16^\circ$ to prevent any retroreflection. The mirror itself is protected from the LAPD and LPP plasmas by a glass blast shield which is self-cleaned by the laser beam. The mirror is coated with an anti-reflective coating, but several ghost reflections are produced by the uncoated blast shield.

The interior dimensions of the mirror box are determined by the beam diameter such that the narrowest point along the beam line (the choke point, Fig. 3.3b) provides sufficient clearance. The initial beam diameter for the 200 J laser is $D_0 \sim 10$ cm (the 15 J laser has a smaller beam). The beam diameter at a distance x from the mirror along the beam path is therefore

$$D(x) = \frac{x}{f_L} D_0 \tag{3.1}$$

Since the beam is focused prior to the final steering mirror, the beam spot on the mirror is approximately half its initial diameter. The mirror therefore sees a substantially higher intensity than any other optic, and consequently the energy throughput of the system is limited by the damage threshold of the mirror (nominally 20 J/cm^2). A conservative estimate of the maximum allowable energy for the current design, including a safety factor for possible hot spots in the beam, is ~ 500 J.

3.2.3 Targets

The laser target is mounted on a motorized drive that allows it to be rotated and translated automatically between shots to ensure that the laser always illuminates a fresh surface. The targets are typically high-density polyethylene (HDPE, C_2H_4) plastic, although graphite (carbon) targets have also been fielded to produce an LPP with fewer protons (Sec. 4.3). Cylindrical targets (with an outer diameter of two inches) were used for the high-repetition rate Peening laser, while flat targets were used to accommodate the Raptor laser's larger spot size.

3.3 Diagnostics

A number of diagnostics are used to characterize the beam and core plasmas and to study the waves produced by their interaction. The core plasma density profile is characterized by a combination of microwave interferometry (Sec. 3.3.2) and voltage-swept Langmuir probes (Sec. 3.3.1). The LPP density is estimated using Langmuir probe ion saturation current measurements (Sec. 3.3.1), while its velocity distribution is characterized by time-of-flight with time-resolved fluorescence measurements (Sec. 3.3.3). Waves are measured using magnetic flux probes (Sec. 3.3.4).

Most signals are digitized using the LAPD's 10-bit data acquisition system (DAQ) at a bandwidth of either 100 MHz or 1.25 GHz. The exceptions are the time-resolved fluorescence and microwave interferometry measurements, which are recorded using 14-bit oscilloscopes to obtain higher dynamic range. Probes are initially aligned visually along the z-axis of the LAPD using a calibrated surveyor's transit (accuracy $\approx \pm 2$ mm). The probes are then moved either by hand (accuracy $\approx \pm 2$ mm) or by motorized probe drives (accuracy $\approx \pm 0.5$ mm). Corrections for changes in the orientation of a moving probe are applied in post-processing. Typical high repetition rate measurements comprise lines or grids of 100's to 1000's of points with spacing of 0.3-1.0 cm and 3-10 shots per position for statistics.

3.3.1 Langmuir Probes

A Langmuir probe consists of a small electrically biased conducting surface (of area A) exposed to a plasma that forms a Debye sheath [87, 24, 85]. The surface is connected to electrical ground through a measurement circuit, drawing a current. The amount of current collected is determined by the bias voltage (V_B) and the properties of the plasma near the surface. Sweeping the bias voltage produces a characteristic current vs. bias voltage curve (IV curve) as shown in Fig. 3.4. In order to form a usable sheath, the Langmuir surface must be much larger than the Debye length. In the LAPD, this condition is easily satisfied

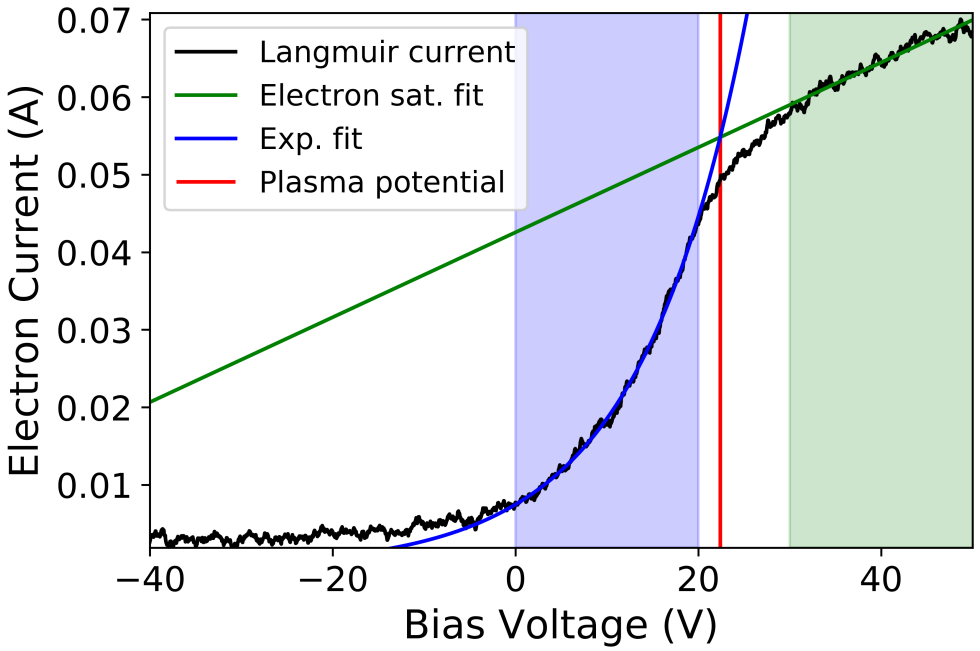

Figure 3.4: An example current trace from a swept Langmuir probe. The green and blue shaded areas indicate the electron saturation region and exponential region respectively, while the lines of the same color show the fits in those regions. The plasma potential is defined by the intersection of the two fits.

(Table 3.1).

A Langmuir probe can be used by either sweeping the bias voltage over a timescale in which the plasma is quasi-stationary or by collecting current at a fixed bias voltage as the plasma changes. In either case, the maximum temporal resolution of the probe is limited by the sheath formation time and the capacitance within the sheath and probe. With careful mitigation of these effects it may be possible to maintain accurate measurements into the several-MHz frequency range [83]. The Langmuir probes utilized in these experiments are estimated to have a frequency response in the hundreds of kHz.

The current collected by a Langmuir probe passes through three regimes as its bias voltage is swept. When a large negative voltage is applied, the probe repels electrons while collecting ions. This portion of the curve asymptotically approaches the ion saturation current, which is the theoretical ion current collected when $V_B = -\infty$. The magnitude of the ion saturation current collected by a probe with tip area A is determined by either the ion or electron temperature depending on the regime [85]

$$I_{sat} = \begin{cases} \frac{1}{4} e n_i A \sqrt{\frac{8kT_i}{\pi m_i}} & T_i \sim T_e \\ 0.6 e n_i A \sqrt{\frac{kT_e}{m_i}} & T_e \gg T_i \end{cases} \tag{3.2}$$

In either regime, time-resolved measurements of the ion saturation current at a constant bias voltage can be used to measure the ion density if the relevant electron or ion temperature is known. In practice, the time-resolution of this measurement is limited by the electrical response of the probe. If the sheath moves on the timescale of the measurements, an additional current is induced [28].

At large positive voltages the current does not asymptotically approach an analogous constant electron saturation current, but rather increases linearly indefinitely. Several effects contribute to this phenomenon including growth of the sheath region with increasing bias voltage and collisional effects [24]. Little information can be extracted from this region

without a sophisticated model.

These two regions are joined in the middle by an exponential transition region that extends from $V_B \approx 0$ to $V_B = V_{pp}$ (Fig. 3.4), where V_{pp} is the plasma potential. In a simple model, the plasma potential should be marked by an abrupt transition to the electron saturation regime. In practice the transition is rounded, and the plasma potential is estimated as the intersection of a linear fit to the electron saturation region and an exponential fit to the transition region. The current collected in the exponential region is [24]

$$I_{exp} = I_{esat} e^{\frac{e(V_B - V_{pp})}{kT_e}} \tag{3.3}$$

where I_{esat} is the ideal electron saturation current

$$I_{esat} = e n_e A \sqrt{\frac{kT_e}{2\pi m_e}} \tag{3.4}$$

The electron density can be estimated from Eq. 3.4 using the current collected at the plasma potential as I_{esat} and the electron temperature from the exponential fit.

3.3.2 Microwave Interferometry

An interferometer can be used to infer the density of a plasma by measuring the phase shift accumulated by a light wave propagating through it [71]. The resulting measurement is inherently line-integrated along the path of the wave's propagation. Interferomters are therefore only capable of measuring plasma densities up to the critical density n_c, above which light cannot propagate. The critical density is proportional to the frequency of the probe wave

$$n_c = \frac{\epsilon_0 m_e}{e^2}\omega^2 = 1.24 \times 10^{-8} [f \text{ in Hz}] \text{ cm}^{-3} \tag{3.5}$$

The LAPD facility includes a built-in array of 60 GHz interferometers. However, in the experiments described here the LAPD plasma density is close to the critical density ($n_c =$

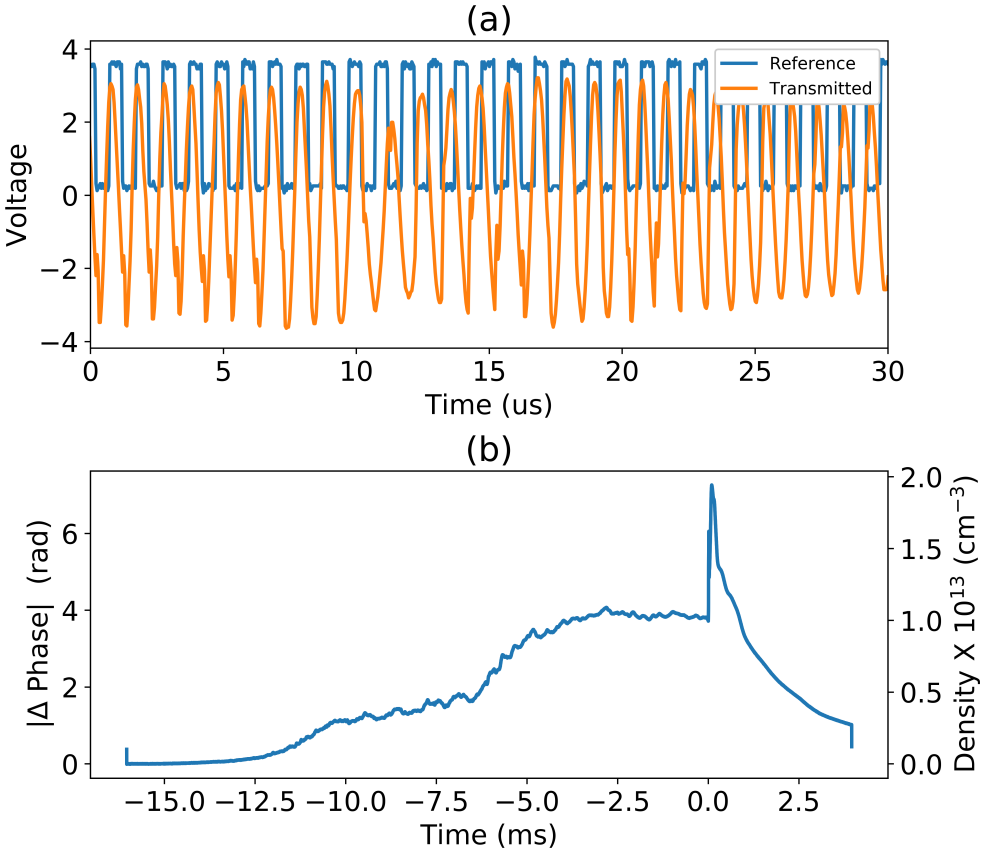

Figure 3.5: a) A short segment of the raw reference and transmitted signals from the LAPD 288 GHz interferometer. b) The phase difference computed from the signals in (a). An estimate of the density (right axis) is made assuming a 20 cm cylindrical plasma column of uniform density.

4×10^{13} cm^{-3}) for this frequency, causing frequent jumps in the wave phase that complicate analysis. Cleaner results are obtained using a 288 GHz interferometer whose critical density ($n_c = 1 \times 10^{15}$ cm^{-3}) is much higher than the densities produced in the experiment.

The interferometer used is heterodyne, employing a 288 GHz probe beam and a 750 kHz local oscillator. The effective temporal resolution is therefore limited by the local oscillator to (750 kHz)$^{-1}$, or approximately 1.3 μs [58]. The probe beam is $\approx$ 10 cm in diameter at its largest extent and converges as it makes a double pass through the plasma. The interferometer's effective spatial resolution is therefore limited to $\approx$ 10 cm. After passing through the plasma, the transmitted beam is mixed with the local oscillator to create a signal in a frequency range that can be readily digitized (Fig. 3.5a). A reference signal is similarly created by mixing the unperturbed probe beam with the oscillator. The total phase shift is in general much larger than 2π, so the raw difference in phase must be unwrapped to determine the absolute phase shift (Fig. 3.5b). The line-integrated density is then [71]

$$\int n_e dl = \frac{-2cn_c\Delta\phi}{\omega_{probe}} \tag{3.6}$$

An estimate of the plasma density can be made by approximating the plasma volume by a simple geometry such as a cylinder (Fig. 3.5b). However this is a poor approximation because the actual plasma profile resembles a flat-top Gaussian (Fig. 3.6a). A more accurate calculation of the density requires a measurement of the density profile of the path along which the interferometer line integrates. This information can be extracted from a Langmuir probe scan over a transverse plane. A lineout of Langmuir probe measurements oriented along the diagonal line-of-sight of the 288 GHz interferometer is shown in Fig. 3.6a. The line-integrated density (units of cm^{-2}) from the Langmuir probe is

$$\int n_e dl = \sum n_e dl \tag{3.7}$$

Where dl is the distance between measurement points. Taking the ratio of Eq. 3.6 to Eq. 3.7

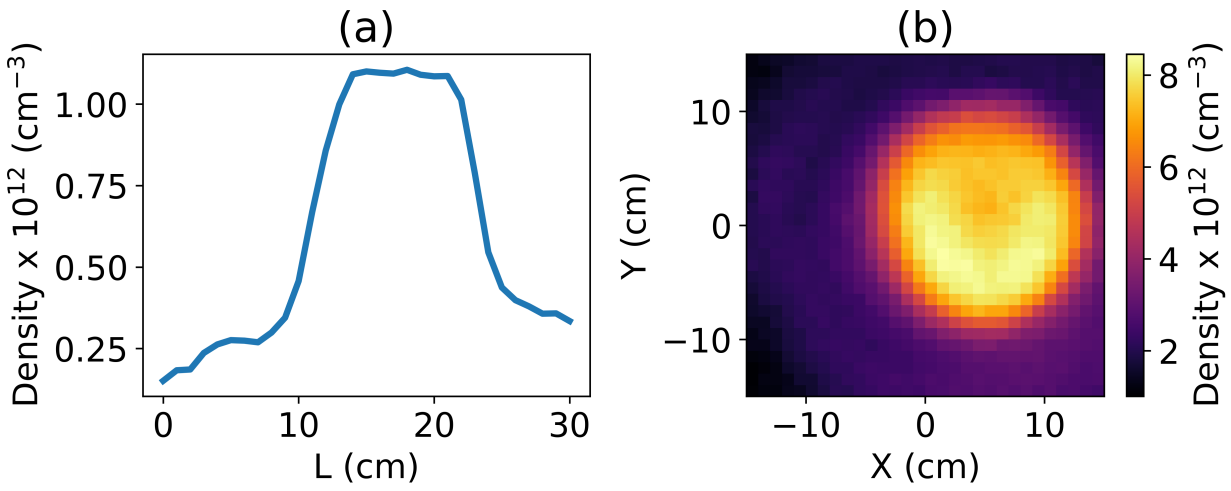

Figure 3.6: a) A density profile taken along a diagonal line across a transverse plane of poorly-calibrated Langmuir probe data (matching the line-of-sight of the interferometer). b) The full plane of Langmuir probe data, now correctly calibrated against the interferometer measurements.

gives a correction factor that can be applied to correctly calibrate the entire Langmuir plane (Fig. 3.6b). A corrected interferometer trace can be obtained by using an effective length in Eq. 3.6 such that

$$\int n_e dl = n_e L_{eff} = n_e \left(2 \int \bar{n_e} dl \right) \tag{3.8}$$

Where $\bar{n_e}$ is the Langmuir profile normalized to its maximum value.

3.3.3 Time-Resolved Fluorescence Monochromator

Time-resolved ion fluorescence measurements are used to characterize the velocity distribution of each LPP charge state (Sec. 4.1). A collection lens (focal length $\sim$ 200 mm) positioned outside of the vacuum chamber focuses fluorescence light onto the entrance slit of a single-grating monochromator with a 1800 g/mm grating, achieving a spectral resolution of 0.3 nm. Fluorescence is most efficiently captured in the image of the entrance slit, which is located on-axis ($x = 0$) in the plasma, and measures approximately 30 μm by 40 mm in the z and y directions. However light may be collected from anywhere in the slit's field-of-view.

Throughout the plasma the field-of-view is thin (< 1 cm) in the z-direction. The light exiting the monochromator is captured by a photomultiplier tube, and the resulting current is read out over a resistor by a dedicated oscilloscope. The effective time resolution of this setup, limited by the readout circuit, is ~ 10 ns.

The velocity of ions measured at a particular time can be calculated by time-of-flight using the distance between the collection lens axis and the target and assuming that the LPP is created at $t = 0$. Applying this method to the entire time trace produces an estimated velocity distribution. The thinness of the collection volume along the z-axis and high time resolution makes this a highly accurate measurement of field-parallel velocity, with estimated errors $< 1\%$ up to 1000 km/s.

3.3.4 Magnetic Flux Probes

A magnetic flux probe or 'bdot' comprises three coils wrapped around a plastic cube with the axis of each coil oriented along a different Cartesian direction [34]. A changing magnetic field will induce a voltage in the coil proportional to $\overrightarrow{dB}$ which is then amplified, numerically integrated, and multiplied by a calibration factor to obtain $\overrightarrow{\Delta B}$. Assuming the ambient magnetic field $\overrightarrow{B_0}$ is known at the beginning of the measurement (a valid assumption in the LAPD prior to the laser firing), $\overrightarrow{B} = \overrightarrow{dB} + \overrightarrow{B_0}$. A static electric field can also induce a voltage in the coil. This effect is removed by winding each coil with a pair of wires and subtracting the result using a custom-built 100 MHz differential amplifier, canceling out the electrostatic component.

The magnetic field measured by a single coil is computed from the measured voltage using the integration method described by Everson [34]

$$\overrightarrow{B} = \frac{A}{an_b g}\left[\int V_{measured}(t)dt + \tau_s V_{measured}(t) + V_0\right] + \overrightarrow{B_0} \tag{3.9}$$

Where g and A are the amplifier gain and an attenuation factor, n_b is the number of turns

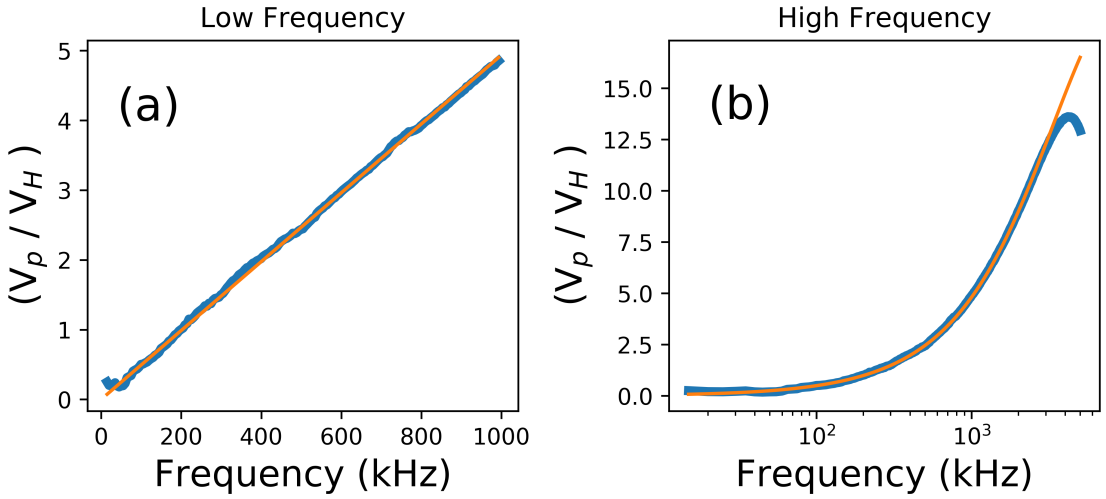

Figure 3.7: Frequency response of a 3 mm magnetic flux probe in a calibration Helmholtz coil. a) A linear fit in the low-frequency limit determines the area of the probe. b) The high-frequency behavior determines the inductance constant τ_s. At a frequency of several MHz, the Helmholtz coil is no longer consistent with the model.

in the coil, and a is the area of coil. $\overrightarrow{B_0}$ is a known constant, and the integration constant V_0 is assumed to be zero. τ_s is the time constant associated with the RL circuit formed by the internal inductance and resistance of the coil (neglecting its capacitance)

$$\tau_s = \frac{L + M}{R_b} \tag{3.10}$$

where L is the inductance of one coil, M is the mutual inductance between two halves of a differentially wound pair, and R_b is the resistance of the coil. The constants a and τ_s are determined empirically by calibrating the probe with a well-characterized magnetic field produced by a Helmholtz coil with a radius of r_H and n_H turns. The coil is driven at frequencies ranging from 10's of Hz to several MHz. Both the drive current (via a resistor R_p) and the induced voltage on the probe coil are recorded by a network analyzer. The theoretical response of the probe to the field is [34]

$$\frac{V_{measured}}{V_{Helmholtz}} = \left(\frac{4}{5}\right)^{3/2} \frac{\mu_0 n_H a n_b g}{r_H R_p} \frac{\omega}{1 + (\omega\tau_s)^2} [\omega\tau_s + i] e^{i\omega\tau} \tag{3.11}$$

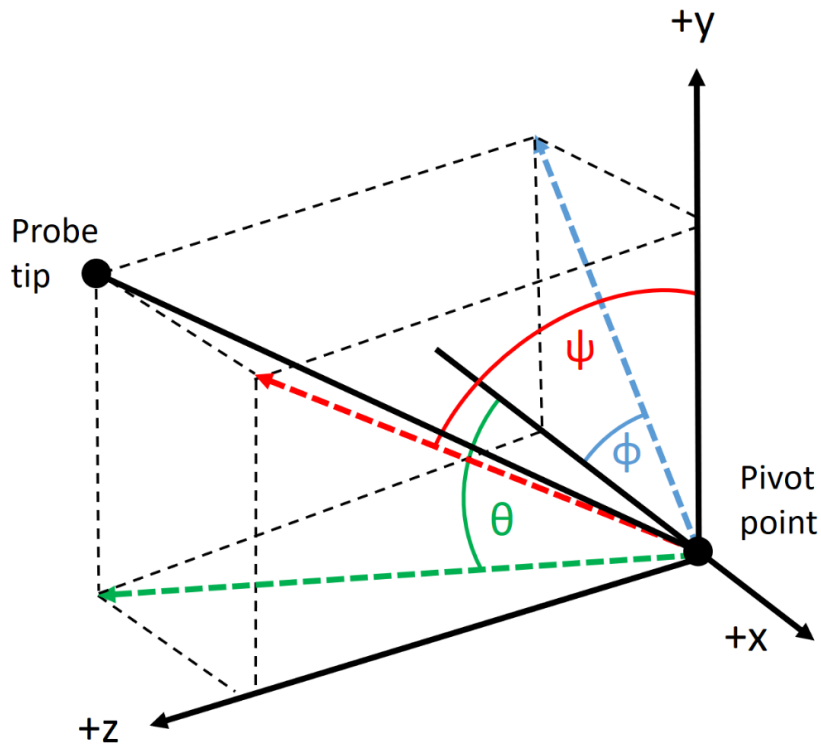

Figure 3.8: The rotation of a magnetic flux probe about a pivot point on its shaft is most naturally described in terms of the principal axes ψ (roll), ϕ (pitch), and θ (yaw), which are the angles made by the probe's projection on the yz, xy, and xz planes respectively.

where τ represents a cable time delay. In practice, this relation describes the Helmholtz field up to several MHz, above which self-resonant effects become important. A straight wire antenna can be used to check the calibration to higher frequencies. In the low-frequency ($\omega\tau_s \ll 1$) limit,

$$\frac{V_{measured}}{V_{Helmholtz}} = \left(\frac{4}{5}\right)^{3/2} \frac{\mu_0 n_H a n_b g}{r_H R_p}(\omega^2(\tau_s - \tau) + i\omega) \tag{3.12}$$

The imaginary part is independent of inductance effects in this limit, and can therefore be fit to determine the coil area (Fig. 3.7a). The area is then fixed and the full frequency range is fit to determine τ_s (Fig. 3.7b).

Magnetic flux probes are initially aligned such that each of the coils is perpendicular to one of the experimental Cartesian axes. However, when moved to different positions

as occurs while collecting a volumetric dataset, the probe axes are rotated relative to the experimental axes. This results in mixing of the magnetic field components between all three coils in different amounts at each position in the dataset.

This effect is purely geometric and can therefore be perfectly corrected during analysis. The probe is initially aligned such that its shaft lies along the x-axis. As the probe moves, it rotates around a point on the shaft that also lies on the x-axis. The natural coordinates to describe this motion are the principal angles ψ, ϕ, and θ, defined graphically in Fig. 3.8. In terms of these angles, if the field in the rotated probe coordinates is $\overrightarrow{B}' = B_x'\hat{x}' + B_y'\hat{y}' + B_z'\hat{z}'$, then the field components in the experimental coordinate system $\overrightarrow{B} = B_x\hat{x} + B_y\hat{y} + B_z\hat{z}$ are

$$B_x = \cos\phi\cos\theta B_x' - \sin\phi B_y' + \cos\phi\sin\theta B_z' \tag{3.13}$$

$$\begin{aligned} B_y = {} & (\sin\psi\sin\theta + \cos\psi\cos\theta\sin\phi)B_x' \\ & + \cos\psi\cos\phi B_y' \\ & + (\cos\psi\sin\phi\sin\theta - \cos\theta\sin\psi)B_z' \end{aligned} \tag{3.14}$$

$$\begin{aligned} B_z = {} & (\cos\theta\sin\psi\sin\phi - \cos\psi\sin\theta)B_x' \\ & + \cos\phi\sin\psi B_y' \\ & + (\cos\psi\cos\phi + \sin\psi\sin\phi\sin\theta)B_z' \end{aligned} \tag{3.15}$$

CHAPTER 4

Characterization of the Laser-Produced Plasma

The growth rates of the beam instabilities discussed in Chapter 2 depend strongly on the density and velocity of the LPP relative to those of the core plasma. It is therefore important to characterize these quantities in order to interpret the results of beam instability experiments. The LPP ion field-parallel velocity distribution is measured by time-of-flight (Sec. 4.1), while measurements of the LPP density are made using Langmuir probes and a microwave interferometer (Sec. 4.2).

Experiments show that while the LPP velocity distribution remains approximately constant throughout the experiment, the LPP density drops precipitously with distance from the target. This decrease is caused by a combination of spatial dispersion due to the LPP's wide velocity distribution and cross-field transport likely caused by beam ion/core electron Coulomb collisions (Sec. 4.4). The resulting evolution of the LPP density can be modeled with a Monte-Carlo calculation (Sec. 4.5).

4.1 LPP Velocity Distribution Measurements

The LPP velocity distribution can be estimated by time-of-flight from a time-series measurement of ion density. In general, measurements at two locations would be necessary to employ this technique. However, since all LPP ions begin at the target at $t \approx 0$, only one additional measurement is necessary in this case. If measurements are made on or near the z-axis, then the velocity calculated represents the velocity component parallel to the field.

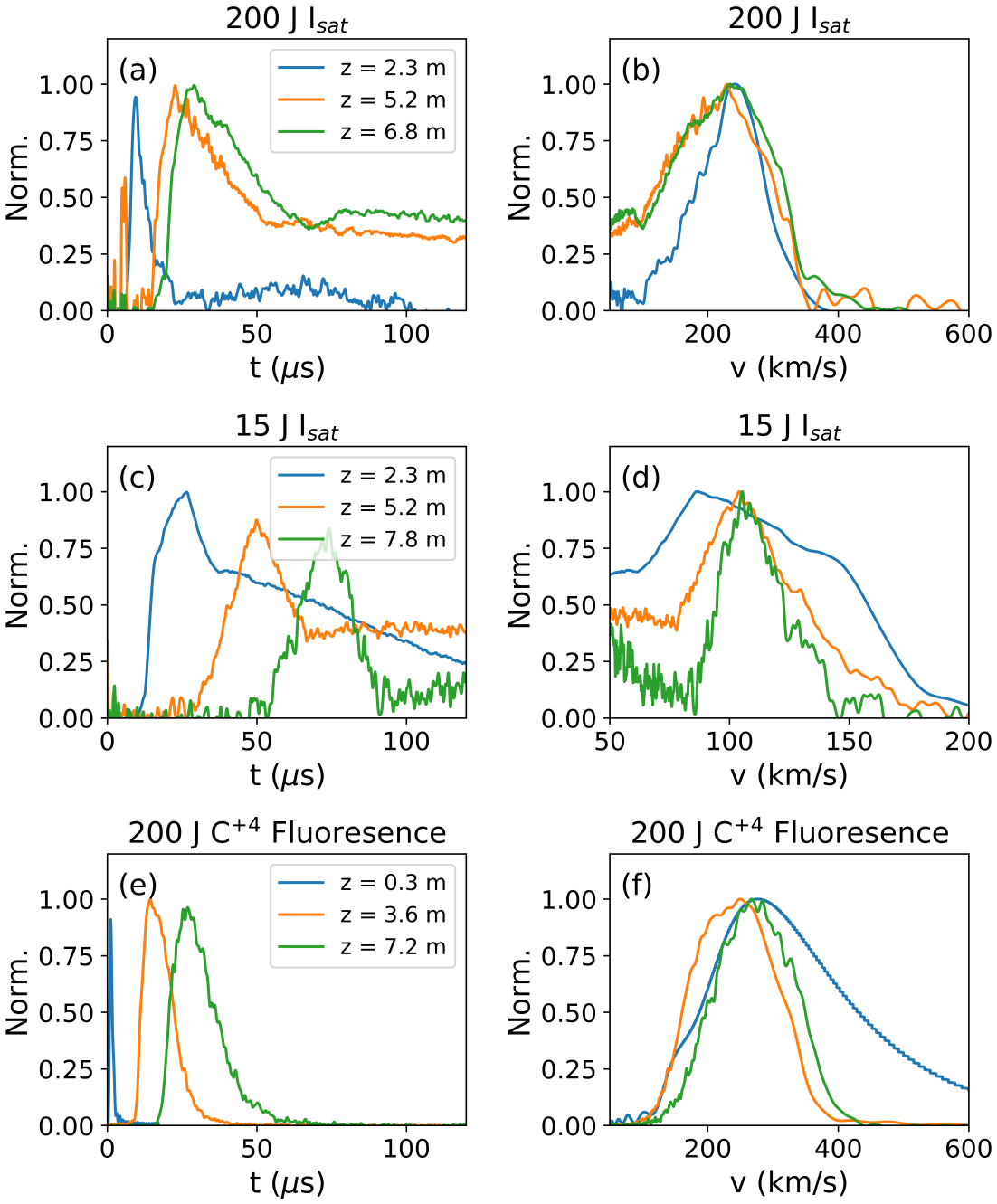

Figure 4.1: Ion saturation current time traces for the 200 J (a) and 15 J (c) lasers, and corresponding LPP velocity distributions inferred by time-of-flight (b,d) show that both lasers produce a super-Alfvénic LPP ($V_A \approx 100$ km/s) but that the 200 J LPP is somewhat faster. Both LPP's remain super-Alfvénic far from the target. Ion florescence measurements of the C^{+4} line in the LPP produced by the 200 J laser (e,f) corroborate the ion saturation current measurements. All time series and velocity distributions are normalized independently.

A Langmuir probe with a constant bias voltage collecting ion saturation current (Sec. 3.3.1) is one way to make an approximate time-resolved measurement of the ion density (Fig. 4.1a,c). This measurement is approximate because extracting the actual density requires additional knowledge of the distribution of charge states collected as a function of time (since the ion saturation current depends on the charge of the ions collected). Ions with higher velocities represent a larger current, so the associated velocity distributions (Fig. 4.1b,d) should be scaled by a factor of $1/v$. Including this factor dramatically enhances the number of slow LPP particles, but it is not included in Fig. 4.1 in order to make the distribution easier to display. The LPP carries a large current that can overwhelm the probe bias circuit, preventing the ion saturation current from returning to zero after the LPP has passed. This artifact translates to an inaccurate measurement of the slow ion velocities.

Ion saturation current measurements have been made at several distances from the target using both the 15 J and the 200 J lasers. The LPP produced by the 200 J laser is somewhat faster ($100-400$ km/s or $M_A = 1-4$) than the LPP produced by the 15 J laser ($100-200$ km/s or $M_A = 1-2$). With both lasers, the LPP velocity distribution remains approximately constant with increasing distance from the laser target.

A time-resolved ion fluorescence monochromator (Sec. 3.3.3) can be used to calculate a cleaner LPP velocity distribution (Fig. 4.1e,f). Light is collected in a relatively thin plane at a known distance from the target, allowing the velocity distribution to be calculated with high resolution. Since faster ions spend less time in the collection volume, this distribution should be weighted by a factor of v. This factor is neglected in Fig. 4.1 for the same display reasons discussed above. This method is sensitive to individual carbon charge states, allowing the velocity distribution for each charge state to be measured independently. Results from this diagnostic corroborate the results of the Langmuir probe measurements reported above.

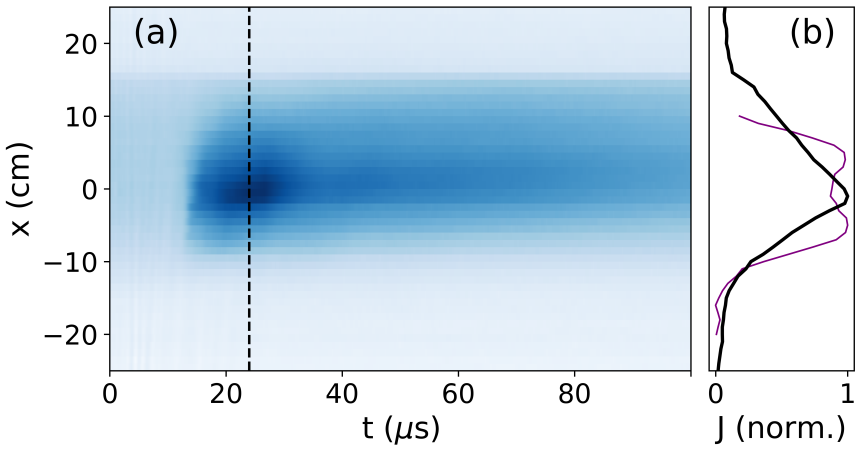

Figure 4.2: A streaked lineout of ion saturation current measurements (a) shows the spatial and temporal variation of the LPP. The time of maximum LPP density is marked by a dashed line. A spatial profile at the time of maximum LPP density (b) illustrates the cylindrical symmetry of the LPP. Comparison to a swept Langmuir probe measurement of the LAPD plasma density profile (purple) shows that the LPP has a similar diameter to the LAPD background plasma.

4.2 LPP Density Measurements

The LPP spatial density distribution can be reconstructed from a multi-shot lineout of many ion saturation current measurements. Fig. 4.2a shows that the LPP is axially symmetric and approximately 20 cm wide (similar to the LAPD core plasma). The sharp leading edge of the LPP is immediately followed by the maximum density. A spatial profile near the peak density is shown in Fig. 4.2b. Since the distribution of charge states being measured is unknown, there is substantial uncertainty in the densities calculated using this method.

A more accurate absolutely calibrated (but line-integrated) LPP density measurement can be made using a microwave interferometer. As with the measurements of the LAPD background plasma density described in Sec. 3.3.2, the normalized measured density spatial profiles are used to extract a peak on-axis density from the interferometer trace. Fig. 4.2 shows that the LPP density profile is relatively constant around the time of peak LPP density, and that the background plasma density profile is also constant over the timescales

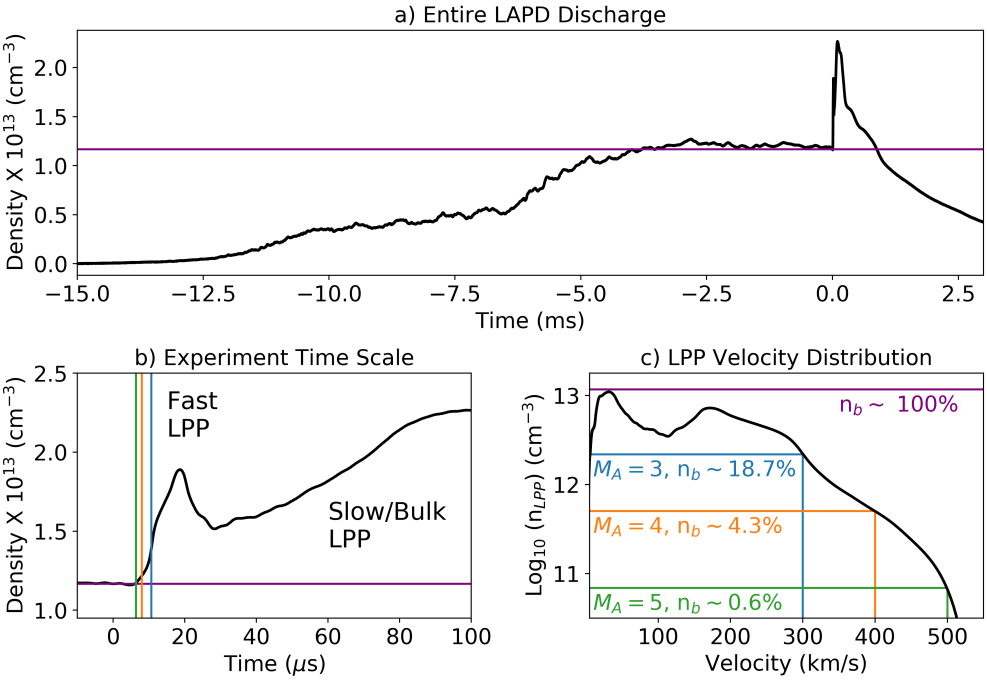

Figure 4.3: A microwave interferometer measurement over the entire duration of the LAPD discharge (a) shows that the LPP density is approximately equal to the LAPD LaB_6 density and dissipates slowly over ~ 1 ms. Looking more closely (b), the LPP is divided into a lower density burst of fast ions followed by a higher-density mass of slow ions (the "bulk"). An approximate velocity distribution calculated from these measurements (c) shows that the fastest LPP ions represent only a small fraction of the background density.

of the LPP. It is therefore a reasonable approximation to assume the same radial density profile over the entire duration of the LPP.

The microwave interferometer shows that two separate LPPs are produced (Fig. 4.3b). The "fast LPP" is a short-duration pulse of LPP that contains the super-Alfvénic ions that are the primary focus of these experiments. This is followed much later by a sub-Alfvénic but higher density "slow LPP" (or "bulk LPP") that persists for hundreds of microseconds. The observation of these two separate populations is consistent with previous fast-gated imaging of the LPP near the target [61]. It is possible that the slower bulk LPP is produced by shock reflection inside the thick plastic target. This hypothesis could be tested in future experiments by measuring the arrival times of both plasmas while varying the target thickness.

Although the maximum LPP density is comparable to the background plasma density (Fig. 4.3a), the quantity important for beam instability growth is the density of the fast ions. The density of the ions in a particular velocity range can be estimated by converting the interferometer measurement to a velocity distribution in the same manner as described in Sec. 4.1. This method has relatively low velocity resolution because of the monochromator's limited temporal resolution and large ($\sim$ 10 cm) beam. However, it suggests that by a distance of 3 m from the target, the density of the fastest ($M_A > 5$) LPP ions has dropped to less than 1% of the background plasma density, while the densities of the slower ions remain much higher (Fig. 4.3c).

4.3 Dependence of LPP on Target Material

The material composition of the laser target determines the atomic composition of the LPP. Both plastic (HDPE, C_2H_4) and pure carbon (graphite) targets were fielded in these experiments. Since the plastic targets contain $\sim$ 14% hydrogen by mass, the resulting LPP should contain a substantial number of protons. These protons should be accelerated to higher

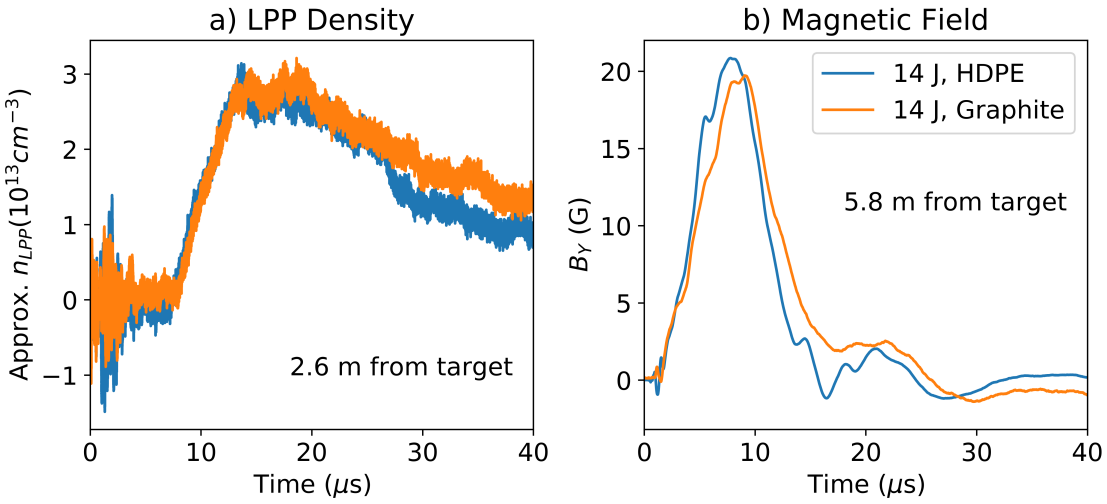

Figure 4.4: A comparison of LPP density (a) and simultaneously measured magnetic fields (b) between otherwise identical runs with different laser target materials. HDPE (plastic) contains hydrogen, and so should produce more fast protons than the pure carbon (graphite) target. However, no appreciable difference is observed between the two measurements. Both runs shown are an average over ten laser shots.

velocities than the heavier carbon ions, and could therefore also generate beam instabilities. However, measurements of both the LPP density and the magnetic fields it generates (Fig. 4.4) do not show a substantial difference between experiments with the two target materials. One possible explanation is that trace amounts of water could be absorbed into the surface of the graphite target, creating protons in that case as well. Another possibility is that the number and charge density of the protons may be too small compared to those of the carbon ions to substantially alter the measured ion density or drive competitive beam instabilities. A more thorough investigation of this topic is left for future work.

4.4 LPP Density Loss Mechanisms

The loss of beam density with increasing distance from the target is one of the fundamental limitations to the efficacy of LPPs as a collisionless shock driver. A number of possible processes were considered as possible mechanisms of density loss including ion-ion Coulomb

	$\nu^{b/c}$ (Hz)	λ_{mfp} (m)
Beam Ion/Core Ion	1.3×10^2	4.0×10^3
Beam Ion/Core Electron	2.4×10^4	20
Beam Electron/Core Ion	1.1×10^8	9.2×10^{-3}
Beam Electron/Core Electron	5.0×10^7	2.0×10^{-2}
Beam Ion/Beam Ion (Dense)	4.8×10^5	1.1
Beam Ion/Beam Ion (Tenuous)	4.8×10^3	1.1×10^2

Table 4.1: Coulomb collision frequencies and mean free paths calculated for a 500 km/s beam of C^{+4} ions and 1000 km/s electrons passing through a He^{+1} background plasma with $T_e = 5$ eV, $T_i = 1$ eV, and $n_c = 9 \times 10^{12}$ cm^{-3}. Intra-beam ion collision rates are calculated for a dense beam near the target ($n_b = 10^{13}$ cm^{-3}) and a more tenuous beam farther from the target ($n_b = 10^{11}$ cm^{-3}) both with $v_{th} = 50$ km/s. λ_{mfp} for the intra-beam collisions is calculated using the parallel streaming velocity $v_b = 500$ km/s.

collisions, recombination, and charge exchange with the core plasma. However, calculations show that none of these processes act fact enough to explain the observed decrease in LPP density. Ultimately, a combination of spatial dispersion due to the wide LPP velocity distribution and cross-field diffusion (likely due to beam ion/core electron Coulomb collisions) is found to be responsible.

4.4.1 Coulomb Collisions

The rate at which Coulomb scattering causes beam particles to lose momentum is [123, 68]

$$\frac{dv_b}{dt} = -\nu^{b,c} v_b = (1 + m_b/m_c)\psi(x^{b,c}) v_0^{b,c} v_b \tag{4.1}$$

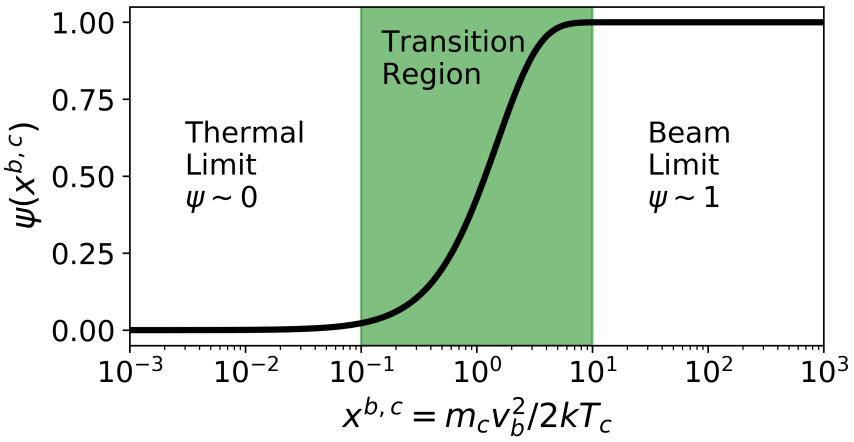

Figure 4.5: The Coulomb collision frequencies depend on the ψ function (Eq. 4.4) whose argument is the ratio between the plasma's directed (beam) and thermal kinetic energies (Eq. 4.2). For a fast beam $\psi = 1$ while for a thermal plasma $\psi = 0$. Simplified expressions for the collision frequencies can be written in either limit. In the intermediary range where the ratio between the beam and thermal energies is between 0.1 and 10, ψ must be calculated explicitly.

where ν^{bc} is the frequency of collisions between beam and core particles (ions or electrons) and

$$x^{b,c} = \frac{m_c v_b^2}{2kT_c} \tag{4.2}$$

$$v_0^{b,c} = \frac{1}{4\pi\epsilon_0^2} \frac{q_b^2 q_c^2 n_c \ln(\Delta)}{m_b^2 v_b^3} \tag{4.3}$$

$$\psi(x) = \frac{2}{\sqrt{\pi}} \int_0^x \sqrt{t} e^{-t} dt \tag{4.4}$$

where $\ln(\Delta) \sim 10$ is the Coulomb logarithm. The mean free path that a particle will travel before being scattered is then

$$\lambda_{mfp} = \frac{v_s}{\nu^{b,c}} \tag{4.5}$$

Where v_s is the streaming velocity of the particles along the field. In the fast-beam limit, $x^{b,c} \gg 1$, $\psi(x^{b,c}) \to 1$. In practice, $x^{b,c} > 10$ is sufficient for this to be an excellent approxi-

mation (Fig. 4.5). In this limit, the collision frequency is

$$\nu_{fast}^{b,c} = \left(1 + \frac{m_b}{m_c}\right) \frac{q_b^2 q_c^2 n_c \ln(\Delta)}{4\pi\epsilon_0^2 m_b^2 v_b^3} \tag{4.6}$$

leading to a mean free path, with $v_s = v_b$, of

$$\lambda_{mfp} = \frac{4\pi\epsilon_0^2 m_b}{\frac{1}{m_b} + \frac{1}{m_c}} \frac{v_b^4}{q_b^2 q_c^2 n_c \ln(\Delta)} \tag{4.7}$$

The strong dependence $\lambda_{mfp} \propto v_b^4$ is crucial for laboratory collisionless shock experiments because it means that fast ions are effectively collisionless over relatively long length scales.

When considering cross-field transport (Sec. 4.4.4), collisions within the LPP are also important. For a thermal plasma colliding with itself, $v_b = v_{th}$ in Eqs. 4.1- 4.4, and therefore $x^{b,c} = 1$ (Fig. 4.5). Since $\psi(1) \approx 0.43$, the thermal collision frequency becomes $\nu_{th}^{b,b} \approx 0.43\nu_{fast}^{b,b}$. When calculating the mean free path the relevant velocity remains the parallel streaming velocity, so $v_s = v_b \neq v_{th}$ in Eq. 4.5.

Table 4.1 presents calculate Coulomb collision frequencies and mean free paths for experimentally-relevant LPP beam and LAPD core plasma parameters. Collisions between beam and core ions are essentially negligible over the experiment length scale of $L \sim 10$ m, making the beam ion-core ion interactions effectively collisionless. Collisions between beam ions and core electrons are marginally collisional, and are the dominant type of collision far from the target. Beam electrons are highly collisional with both core ions and electrons, making the single shared electron fluid approximation appropriate for analytical theory and simulations. The intra-beam ion collision frequency depends strongly on the assumed v_{th} and beam density, so Table 4.1 includes values estimated in the dense plasma near the target ($n_b = 10^{13}$ cm^{-3}) and farther away ($n_b = 10^{11}$ cm^{-3}) with an estimate of $v_{th} = 50$ km/s in both cases. Intra-beam collisions occur more frequently near the target, but always occur more quickly than collisions with the core ions. Far from the target, beam ion collisions with core electrons become much more common than intra-beam collisions.

Z	α_R (s^{-1})	α_C (s^{-1})	τ (s)
1	-4.0E-2	-5.0E-6	25
2	-1.6E-1	-9.2E-5	6.2
3	-3.6E-1	-4.4E-4	2.7
4	-6.5E-1	-1.3E-3	1.5
5	-1.0	-2.9E-3	9.9E-1
6	-1.5	-5.6E-3	6.9E-1

Table 4.2: Recombination rates and timescales for each species of carbon assuming $n_e = 1 \times 10^{13}$ cm^{-3}, $n_b/n_e = 0.05$, and $T_e = 5$ eV.

4.4.2 Recombination

Recombination is the process by which electrons in a plasma recombine with electrons to neutralize or reduce their ionization. This occurs through two primary mechanisms

- Radiative Recombination (R_R): $e^- + X^{+1} \rightarrow X + \hbar\omega$
- Collisional Three-Body Recombination (R_C): $2e^- + X^{+1} \rightarrow X + e^-$

where $\hbar\omega$ is an emitted photon. The recombination rates for each processes are [55, 101]

$$R_R = -2.7 \times 10^{-13} Z^2 T_e^{-3/4} n_i \quad s^{-1} \tag{4.8}$$

$$R_C = -9.2 \times 10^{-27} Z^3 \ln\sqrt{Z^2+1}\, n_e n_i T_e^{-9/2} \quad s^{-1} \tag{4.9}$$

with n_e and n_i in cm^{-3} and T_e in eV. Higher charge states recombine more quickly, and both mechanisms are more efficient at lower temperatures and higher densities. Note that these equations depend on T_e rather than v_b because they are derived in the warm plasma regieme where $v_{th,e} \gg v_b$. Increasing v_b while keeping $v_{th,e}$ constant should further lower these recombination rates. Collisional recombination dominates over radiative recombination when [101]

$$n_e \gg 3 \times 10^{13} \frac{T_e^{3.75}}{Z} \quad cm^{-3} \tag{4.10}$$

The total recombination rate, including both processes, is

$$\frac{dn_e}{dt} = (R_R + R_C)n_e = Rn_e \tag{4.11}$$

Assuming an exponentially decaying density, $n_e \propto \exp[-t/\tau]$, allows the definition of a characteristic timescale for the recombination process

$$\tau = \frac{1}{R} \tag{4.12}$$

As the LPP expands, it carries with it a population of electrons that preserve quasi-neutrality. These electrons are hot and dense near the target surface ($n_e > 10^{16}$ cm^{-3}, $T_e \sim 15$ eV) but rapidly expand and equilibrate to the background LAPD plasma values ($n_e \sim 10^{13}$ cm^{-3}, $T_e \sim 5$ eV) after several centimeters [104]. Based on Eq. 4.10, we therefore expect collisional recombination to dominate near the target, but radiative recombination to dominate throughout the rest of the experiment.

Table 4.4.2 presents recombination rates and timescales for beams of different charge states of carbon with the LAPD background plasma far from the laser target. At these long time scales, recombination cannot explain the loss of LPP density observed in the experiments. Tables of carbon recombination coefficients calculated using more accurate models are available in the literature [88], and suggest even longer recombination time scales[1] than those predicted by Eqs. 4.8 and 4.9.

4.4.3 Charge Exchange

Charge exchange is the transfer of electrons from a neutral or partially ionized atom to an atom in a higher ionization state. The overall charge in the plasma remains constant, but charge may be transferred from one plasma component to another. If a beam ion is

[1]Note that the literature often uses the naming convention $\alpha_R = R_R/n_i$ and $\alpha_C = R_C/n_i n_e$.

Process	Cross Section (cm^2)	Mean Free Path (m)
$C^{+2} + He \rightarrow C^{+1} + He^{+1}$	5.7E-16	175
$C^{+3} + He \rightarrow C^{+2} + He^{+1}$	8.3E-16	120
$C^{+4} + He \rightarrow C^{+3} + He^{+1}$	1.4E-16	714
$C^{+5} + He \rightarrow C^{+4} + He^{+1}$	6.3E-16	159
$C^{+6} + He \rightarrow C^{+5} + He^{+1}$	8.5E-16	118

Table 4.3: Charge exchange electron capture cross sections [72] and associated mean free paths for ions with $v_b \approx 500$ km/s.

neutralized by charge exchange with a core ion or neutral atom, the beam density is reduced. There are several charge exchange processes that could transfer charge from the carbon LPP to the helium core plasma, but the most probable is single electron capture.

- Single Electron Capture: $C^{+q} + He \rightarrow C^{+(q-1)} + He^{+1}$

The cross-section $\sigma(v)$ for this interaction for a given carbon ion is velocity-dependent, and is related to an effective mean free path by the background neutral helium density

$$\lambda_{mfp} = \frac{1}{n_c \sigma(v)} \tag{4.13}$$

Charge exchange cross sections are often measured experimentally, although predictive empirical models have also been developed [38]. Table 4.3 reports experimentally-measured [72] charge exchange cross sections for single electron capture between carbon ions and a helium background with a relative velocity of ~ 500 km/s. The associated mean free paths demonstrate that charge exchange is not a significant LPP density loss process in the experiment.

4.4.4 Cross-Field Diffusion

The LPP ions are strongly magnetized ($f_{ci} \gg \nu_s^{bi,ci}$) and therefore follow helical trajectories around fixed magnetic field lines determined by their initial perpendicular velocity components. In this model there is no transport of LPP perpendicular to the field. However, in reality collisions within the LPP ions and with core plasma electrons (collisions with the

	D (m^2/s)
Beam Ion/Core Ion	12
Beam Ion/Core Electron	1.8×10^3
Beam Ion/Beam Ion (Dense)	4.3×10^4
Beam Ion/Beam Ion (Tenuous)	430

Table 4.4: Cross-field diffusion coefficients calculated for the four beam ion collision frequencies calculated in Table. 4.1.

core ions being rare) lead to diffusion across the field. The rate of diffusion is characterized by the diffusion constant D defined by Fick's law

$$n = -D\frac{\partial n}{\partial x} \tag{4.14}$$

or, qualitatively, in terms of a random walk process with step size δx and collision frequency $1/\delta t$

$$D = \frac{(\delta x)^2}{\delta t} \tag{4.15}$$

As shown in Table 4.1, $\nu^{bb} \ll \omega_{cb} \approx 1$ MHz. In this regime, the classical diffusion model applies, and the beam ion diffusion coefficient is [79]

$$D = \frac{\overline{v^2}}{3\omega_{cb}^2}\nu^{bb} \tag{4.16}$$

Where v is the velocity of the diffusing particles between collisions. This velocity may be the drift velocity v_b (for a cold beam) or the thermal velocity v_{th} (for a warm plasma). In either case, the velocity of any other components of the plasma is irrelevant. Beam ions can collide with multiple species, so the cumulative diffusion coefficient is

$$D = \sum_{s\in\{bi,ci,e\}} D_s \tag{4.17}$$

where bi, ci, and e represent the beam ions, core ions, and electrons respectively. Table 4.4.4 presents diffusion coefficients for each of these species calculated using Eq. 4.16 for the same

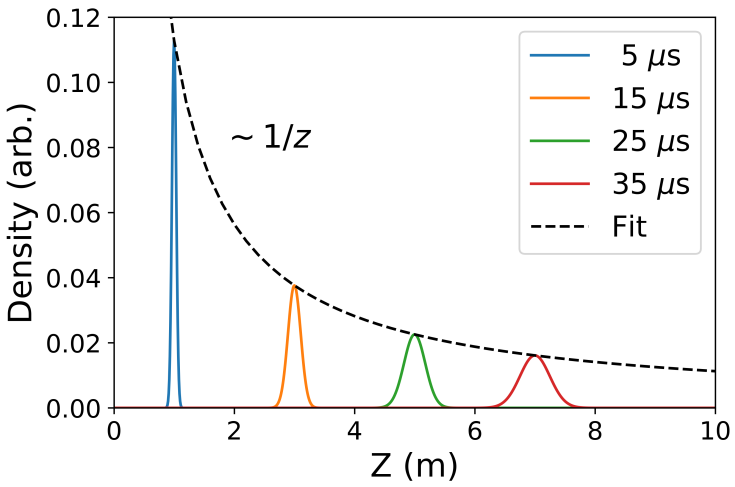

Figure 4.6: A 1D analytic example of spatial dispersion for a Gaussian velocity distribution with $v_0 = 200$ km/s and $v_{th} = 10$ km/s.

conditions as listed in Table 4.1 and with $B_0 = 300$ G.

The magnitude of the cross-field transport depends strongly the collision frequency and therefore on the plasma density and beam velocity relative to the scattering particles. Near the target, beam ion density and the relative velocity between adjacent beam ions is high, leading to a high intra-beam ion collision frequency and a correspondingly large diffusion coefficient. However, as the LPP expands the beam ion density decreases precipitously due to spatial dispersion (Sec. 4.4.5). The relative velocity between adjacent beam ions also decreases as the LPP spatially stratifies by velocity. Relatively quickly, the intra-beam ion collision frequency falls below the beam ion/core electron collision frequency and the diffusion coefficient associated with that processes becomes dominant. This is the case throughout most of the experiment, so to a reasonable approximation $D = D_e \approx 2000$ m^2/s.

4.4.5 Spatial Dispersion

Spatial dispersion is an inherent property of any particles with a velocity distribution of non-zero width. As the system evolves particles are spatially stratified by velocity, effectively lowering their density. This process can be simply illustrated in 1D for a Gaussian velocity

distribution

$$n(v) \propto \exp\left[-\left(\frac{v - v_0}{v_{th}} \right)^2 \right] \tag{4.18}$$

where v_0 and v_{th} are the distribution drift velocity and thermal velocity respectively and $\int n(v)dv = 1$. At a given time t, the spatial distribution of particles is then

$$n(x) \propto \exp\left[-\left(\frac{x/t - v_0}{v_{th}} \right)^2 \right] \tag{4.19}$$

Fig. 4.6 shows how the density of this distribution drops as different velocities separate. A fit to the maximum densities as the distribution evolves shows that the peak density decreases as $\sim 1/z$. This scaling is valid in the regime where $0.05 < v_{th}/v_0 < 0.5$ which is relevant to the LPPs produced in these experiments. Modeling this dispersion process in 3D for a realistic LPP velocity distribution requires a more sophisticated numerical model, as discussed in Sec. 4.5.

4.5 A Monte-Carlo LPP Density Dispersion Model

Accurate knowledge of the LPP density distribution is required to interpret beam instability growth measurements, but diagnostic limitations make completely spatially and temporally resolved measurements difficult to achieve. A numerical model for the LPP evolution is therefore necessary. The model chosen must be computationally tractable while retaining all of the relevant physical processes. Cyclotron motion is a dominant feature over the time scales of interest ($t \sim 1/\Omega_{ci}$) precluding the fluid approximation, while the experiment length scale ($L \gg \delta_i$) makes particle-in-cell (PIC) or 3D hybrid simulations prohibitively expensive. The large ion gyroradius (comparable to the diameter of the LAPD core plasma) rules out a gyrokinetic model. The problem can be greatly simplified by assuming that all interactions both within the LPP and between LPP ions and the core plasma can be cumulatively modeled as a single cross-field diffusion process with a diffusion coefficient that

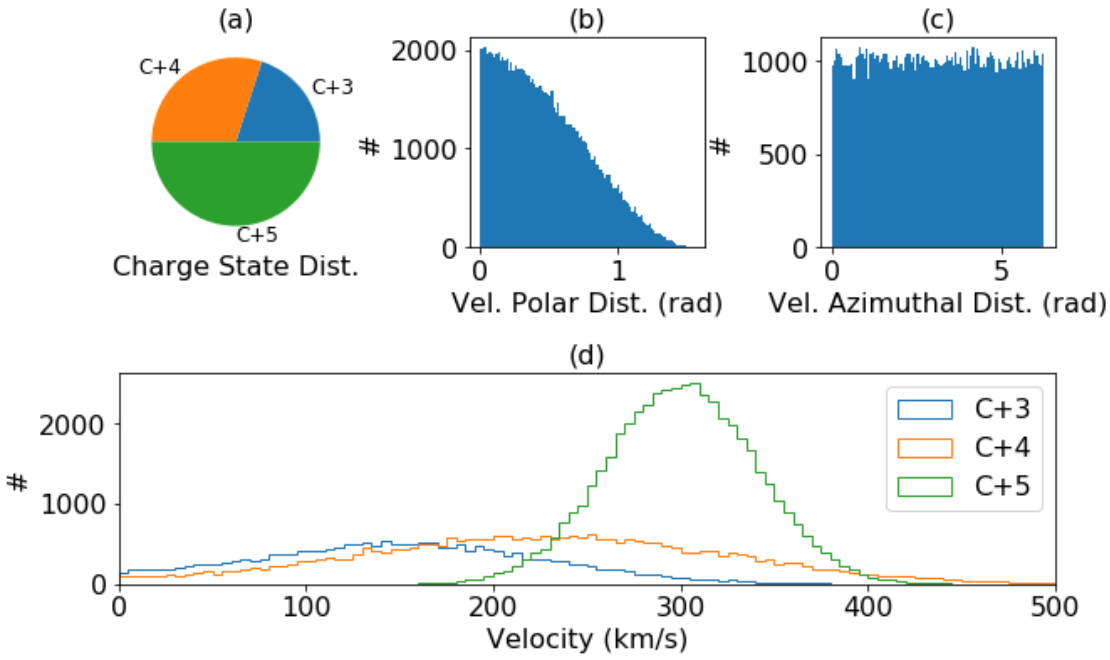

Figure 4.7: An example of the statistical distributions of approximately 10^5 particles used in a Monte-Carlo calculation of the LPP trajectories. a) The relative fractions of the three ion species. b,c) The polar and azimuthal velocity angle distributions. d) The velocity magnitude distributions for each ion species.

can be approximated as constant throughout the experiment. Under this assumption, the LPP ions follow single particle cyclotron orbit trajectories whose gyrocenters diffuse across the field, providing a set of equations that are easily analytically solvable given the initial ion positions and velocities. A Monte-Carlo calculation can then be used to estimate the spatial and temporal evolution of the LPP density distribution.

The relative numbers of different charge states in the LPP have been qualitatively assessed with ion fluorescence measurements, but have been more quantitatively determined with 1D radiative hydrodynamics (rad-hydro) simulations [104]. Several of the most prominent charge states are included in the Monte-Carlo distribution (Fig. 4.7a). The parallel velocity distribution of the LPP has been determined by both rad-hydro simulations and experimental measurements (Sec. 4.1). A qualitative comparison to this data was used to construct a similar Gaussian parallel velocity distribution for each charge state (Fig. 4.7d). In order to

determine the velocity vector components for each particle, distributions are generated for azimuthal angle ϕ and the polar angle $\theta = \vec{v} \cdot \hat{z}$. The ϕ distribution is uniform (Fig. 4.7c), reflecting the cylindrical symmetry of the LPP. The θ distribution is assumed to be of the form $\cos^2\theta$ (Fig. 4.7b), consistent with previous experimental measurements [61]. In practice, this distribution was assembled by normalizing the distribution over its range of $[0 - 2\pi]$ and computationally inverting the cumulative distribution function which was then used to translate uniformly distributed random values into the $\cos^2\theta$ distribution.

$$\text{CDF} = \frac{\int \cos^2\theta d\theta}{\int_0^{\pi/2} \cos^2\theta d\theta} = \frac{1}{2}(\theta + \sin\theta\cos\theta)/0.785 \tag{4.20}$$

The initial position of the LPP is the point where the laser hits the target, previously defined as the origin. The trajectory equations for a gyrating particle are then

$$\begin{aligned} x &= r_L \cos(\omega_{ci} t + \psi_0) + x_{GC} \\ y &= r_L \sin(\omega_{ci} t + \psi_0) + y_{GC} \\ z &= v_z t \end{aligned} \tag{4.21}$$

where r_L is the Larmor radius, ω_{ci} is the cyclotron frequency, ψ_0 is the gyrophase, and (x_{GC}, y_{GC}) is the center of gyration. The Larmor radius r_L and the cyclotron frequency can be calculated given the ion species and velocity distributions determined. The initial center of gyration for each particle is similarly calculated

$$\begin{aligned} x_{GC} &= r_L \cos(\phi) \\ y_{GC} &= r_L \sin(\phi) \end{aligned} \tag{4.22}$$

The initial phase of gyration ψ for each particle is then determined by requiring that the particle begin at the origin at $t = 0$, which leads to the condition that $\psi_0 = \phi + \pi$ (Fig. 4.8).

At the beginning of each time step t, the guiding centers are moved randomly to model

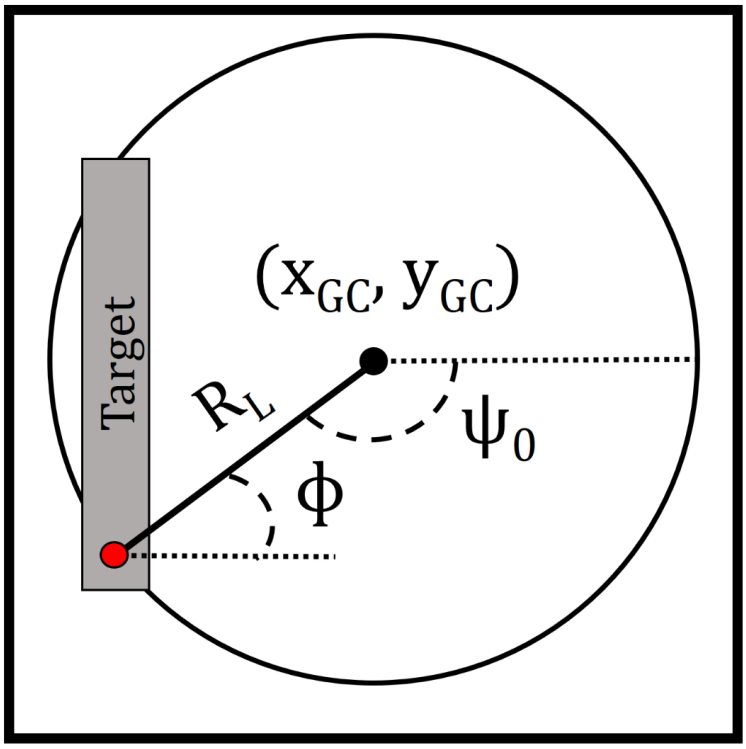

Figure 4.8: A schematic showing the relationship between the azimuthal velocity angle ϕ and the initial gyrophase angle ψ_0 for a particle with gyrocenter (x_{GC},y_{GC}).

cross-field diffusion. The updated guiding center positions are

$$x_{GC} = x_{GC,t-1} + \delta_D \cos\xi \tag{4.23}$$

$$y_{GC} = y_{GC,t-1} + \delta_D \sin\xi \tag{4.24}$$

where $\xi \in [0, 2\pi]$ is a random angle chosen from a uniform distribution. The diffusion step size is

$$\delta_D = \sqrt{Ddt} \tag{4.25}$$

where D is a diffusion coefficient with units of m^2s^{-1}. After updating the guiding centers of all the particles, the position of each particle at that time step is directly calculated using Eqs. 4.21. Estimates of the ion density are made by counting the number of quasi-particles in a defined volume (e.g. 1 cm^3) and then scaling the result by the ratio of the number of quasi-particles to the the estimated actual number of LPP ions. Previous laser plasma characterization experiments [104] have validated models for the number of particles produced as a function of laser and target parameters. These models predict $N_P = 5 \times 10^{15}$ for the 15 J laser and $N_P = 5 \times 10^{16}$ for the 200 J laser.

The diffusion coefficient and initial particle charge state and velocity distributions are adjusted by comparing "virtual" Langmuir probe measurements from the calculation to Langmuir probe density measurements from several positions in the experiment (Fig. 4.9). Virtual Langmuir probe traces are created by counting the number of quasi-particles in a small volume at each time step. Each particle is weighted by its charge state and velocity to match experimental measurements. The diffusion coefficient D is then chosen to match the calculation output to the experimental measurements. Based on Fig. 4.9, a value of $D \sim 5000$ m^2/s was chosen. This value is approximately consistent (within a factor of $\sim 2\times$) with the diffusion coefficient predicted for beam ion/core electron collisions in Table 4.4.4.

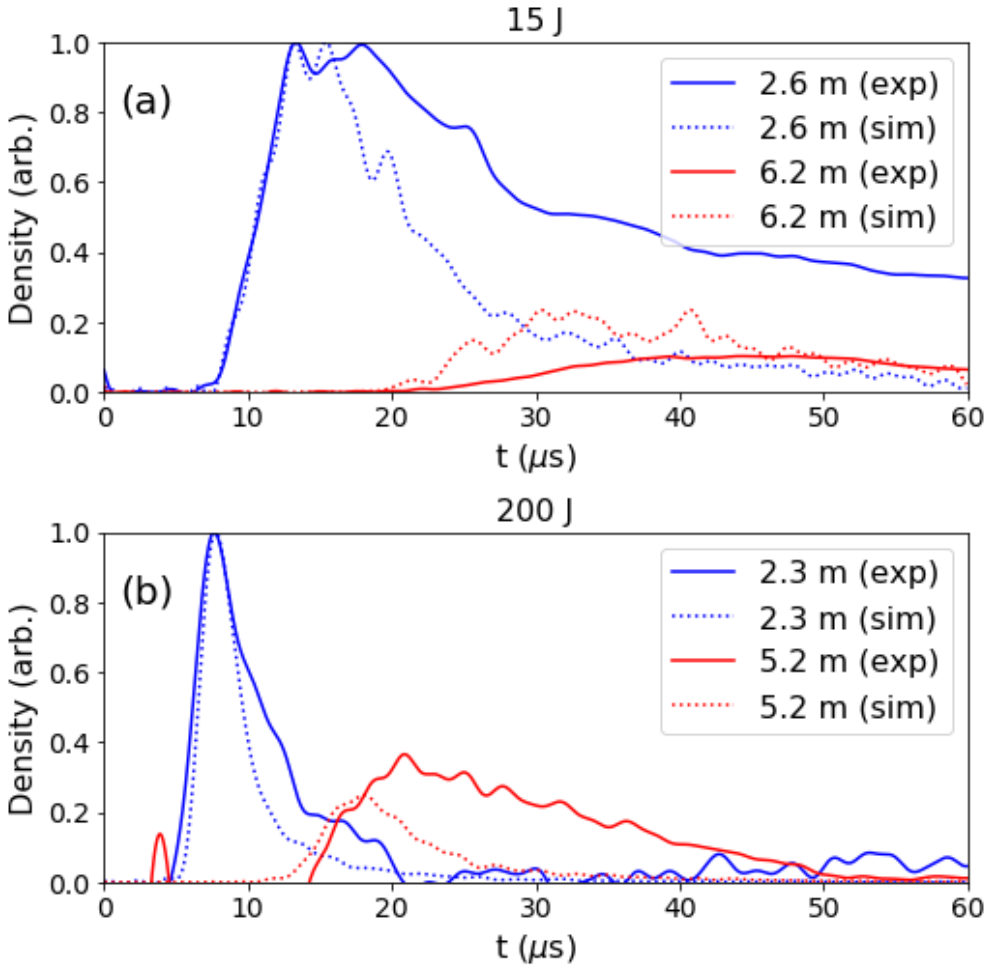

Figure 4.9: A comparison between two synthetic Langmuir traces created using results from the Monte-Carlo model and two experimental Langmuir ion saturation measurements recorded using the 15 J laser (a) and the 200 J laser (b). Each set of traces is normalized by the peak values of the probe closest to the target.

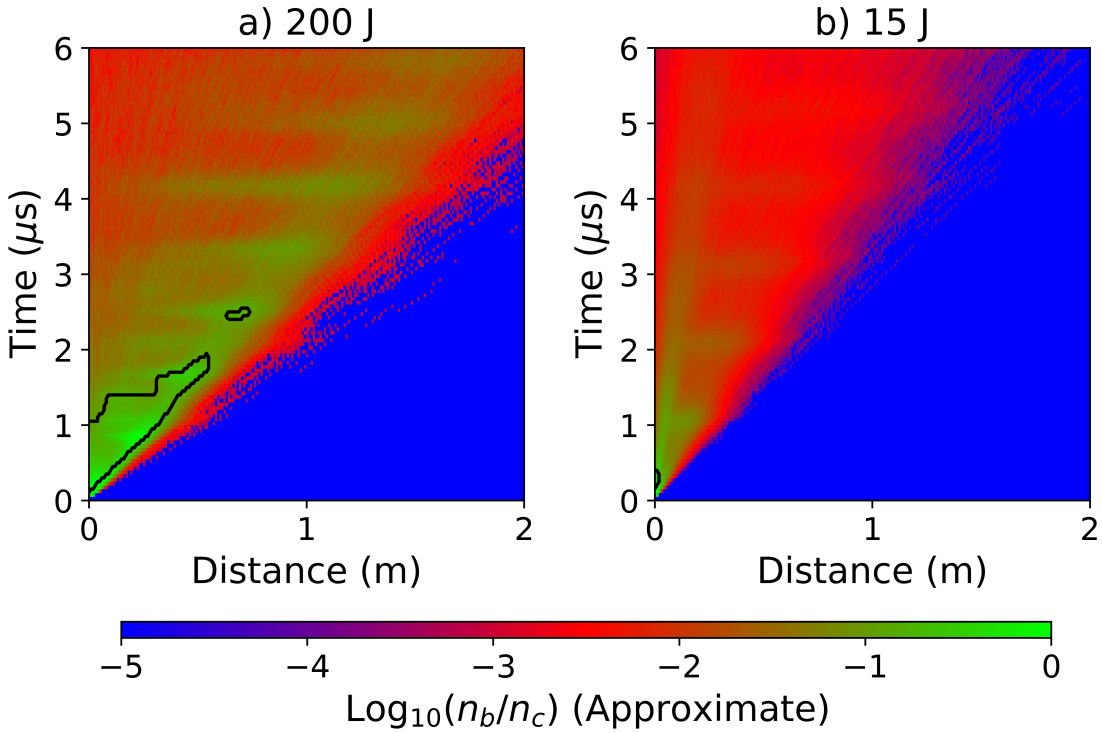

Figure 4.10: Approximate LPP density on-axis as a function of time and distance from the laser target for the 15 J and 200 J lasers. The black contour denotes the region where $n_b/n_c \geq 0.1$, corresponding to rapid growth of the RHI.

CHAPTER 5

Electromagnetic Wave Measurements

The growth of electromagnetic ion/ion beam instabilities, and ultimately the shock formation process, are most readily observable as oscillations in the magnetic field. In the experiment, these waves are measured by an array of magnetic flux probes (Sec. 3.3.4) which record a time series of the vector magnetic field (Sec. 5.1). Analysis of these time traces shows the arrival of several distinct waves, distinguished by their polarization (Sec. 5.2) and spectral characteristics (Sec. 5.3), including a group of waves consistent with excitation of the RHI. The distribution of the wave frequencies as a function of time suggests that the RHI waves originate in a small region near the laser target (Sec. 5.3.2), propagate through the LAPD, and undergo at least one reflection (Sec. 5.3.3). Spatially-resolved measurements collected over multiple laser shots support the conclusion that growth of the RHI occurs only in a small region near the target (Sec. 5.4.1) and reveal the wave's transverse spatial structure (Sec. 5.4.2). The dispersion relation of the RHI waves is estimated experimentally and suggests that the lower-frequency waves observed may propagate obliquely (Sec. 5.4.3). The wave amplitudes are found to vary with beam and background plasma parameters (Sec. 5.5) as predicted by linear theory for the RHI. Direct comparisons of laboratory measurements to 2D hybrid simulations (Sec. 5.6) show that the hybrid model accurately captures the beam instability physics occurring in the experiment, while comparisons to spacecraft observations (Sec. 5.7) show that the waves observed in the experiment are similar to those created by beam instabilities upstream of the Earth's quasi-parallel foreshock. Cumulatively, these observations constitute strong evidence that the waves observed in the experiment are generated by the RHI in a small region near the laser target.

5.1 Time Trace Observations

An array of magnetic flux probes (Sec. 3.3.4) are used to make temporally resolved vector measurements of magnetic fields in the experiment. Fig. 5.1 shows examples of the waves driven by both lasers. These waves originate near the laser target and disperse by frequency as they propagate through the LAPD (Fig. 5.2). Three separable wave features are observed, as shown in Fig. 5.3, with the parameters reported in Table 5.1. In ascending order of arrival time, these features are labeled here as 1) the lower hybrid wave, 2) the RHI waves, and 3) the shear Alfvén wave.

The lower hybrid wave is a high frequency ($\omega > 1$ MHz) low amplitude (~ 0.1 G) wave packet that blends into the beginning of the RHI waves in Fig. 5.1 but can more clearly be differentiated in Fig. 5.3. These waves appear to be linearly polarized at an angle of $\sim 45°$ below the x axis. The early arrival time of these waves corresponds to a velocity of 1000 - 1600 km/s ($M_A \sim 10 - 16$), which suggests that they are created by particles moving with comparable speeds. This range of velocities is consistent with laser-produced electrons [91]. Previous experiments on the LAPD [132] have shown that fast laser-produced electrons can drive quasi-electrostatic whistler waves (lower hybrid waves) near and above the background plasma lower hybrid frequency

$$\omega_{LH}^2 = \Omega_e \Omega_i / (1 + \Omega_e^2 / \omega_{p,e}^2) \tag{5.1}$$

where $\omega_{p,e}$ is the electron plasma oscillation frequency. At these experimental parameters (Table 3.1), $\omega_{LH} = 1.5$ MHz. The approximate match between ω_{LH} and the frequency of this wave suggests that it is a lower hybrid wave [132].

The RHI waves arrive shortly after the lower hybrid waves with slightly lower frequencies ($0.2 - 2$ MHz) but are distinguished by their clear circular polarization (Sec. 5.2). These waves are dispersive (consistent with the whistler wave dispersion relation) and therefore form a chirp in frequency space as the propagate (Sec. 5.3). The group velocities ($200 - 600$

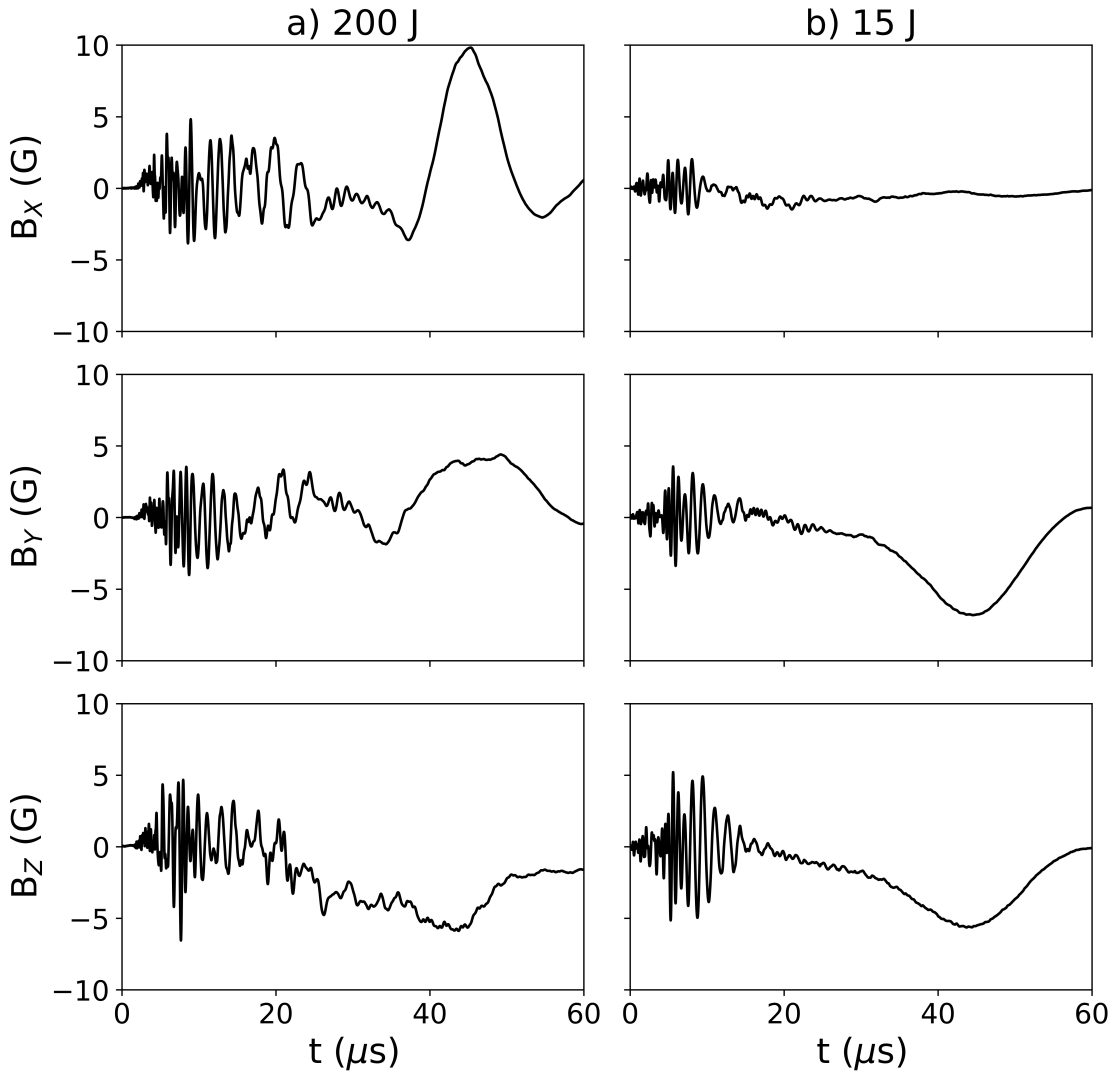

Figure 5.1: Time traces of the vector magnetic field recorded by a magnetic flux probe 7.5 m from the laser target show waves driven by the 200 J (a) and 15 J (b) lasers. These measurements show a chirp of high-frequency waves generated by the RHI, followed by a slower low-frequency shear Alfvén wave. The waves observed using the 15 J laser are similar but lower amplitude than those driven by the 200 J laser.

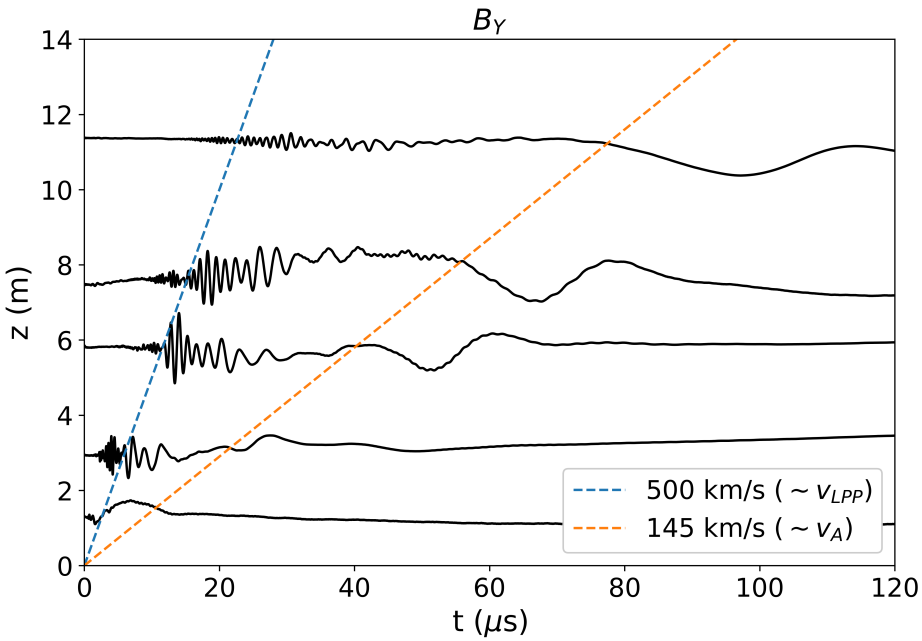

Figure 5.2: Measurements from an array of magnetic flux probes show a packet of waves propagating away from the laser target at a speed comparable to the super-Alfvénic LPP. A shear Alfvén wave follows, propagating at the Alfvén velocity.

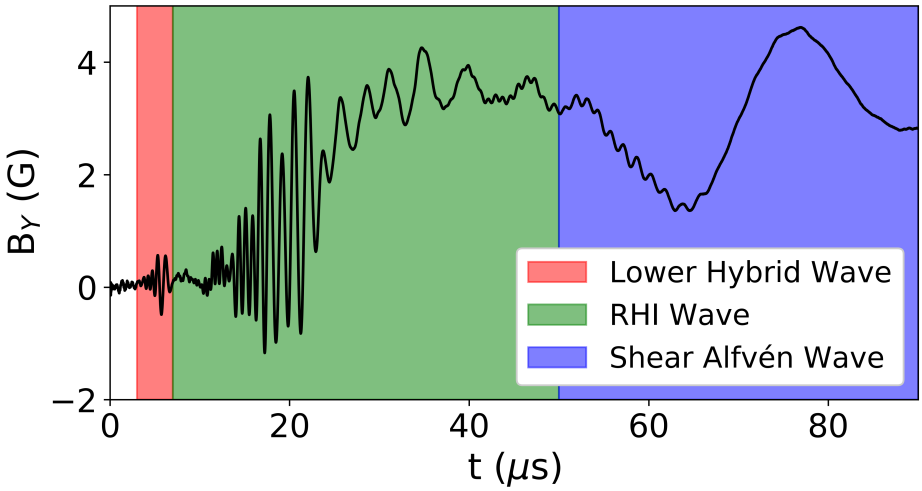

Figure 5.3: Three separable wave features are observed in the experiments: the lower hybrid wave, the RHI waves, and the shear Alfvén wave. These features travel through the LAPD with group velocities of approximately 1000 km/s, 400 km/s, and 150 km/s respectively.

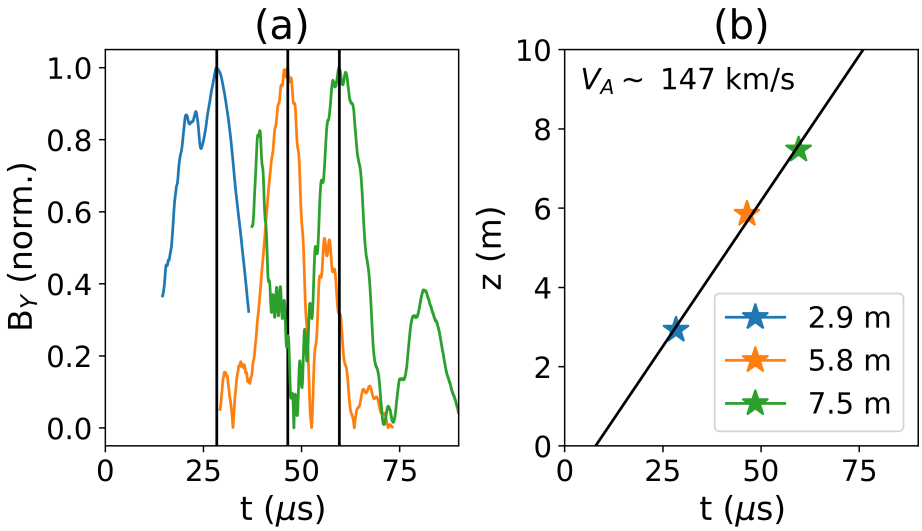

Figure 5.4: The Alfvén velocity (in the center of the LAPD plasma) is experimentally determined by measuring the arrival time of the shear Alfvén wave peak on several magnetic flux probes (a) and then applying a linear fit (b).

km/s) and frequencies of these waves are consistent with the theoretical description of the waves generated by the RHI (Sec. 2.1). The amplitudes of the waves are similar on all three components of the magnetic field, suggesting that they may be propagating oblique to the background magnetic field.

The low frequency ($\omega < \Omega_c$) shear Alfvén wave propagates at the Alfvén speed, providing a convenient means of experimentally determining this parameter by comparing the arrival time of the wave on different probes (Fig. 5.4). The Alfvén velocity varied throughout the experiments (primarily due to changes in the background density) with a typical value being $\sim$ 145 km/s. The shear Alfvén wave is predominantly measured on the transverse components of the magnetic field, consistent with a shear wave propagating parallel to the background magnetic field. Shear Alfvén waves have been previously studied in the LAPD [131, 129, 48, 122]. In the current experiments the wave continues to grow in amplitude as it propagates, reaching a maxima slightly off axis (x = 5 cm) of $\delta B/B_0 = 0.13$ ($\delta B = 40$ G) with the 200 J laser and $\delta B/B_0 = 0.03$ ($\delta B = 8$ G) with the 15 J laser. The polarity of the shear wave ($+\hat{y}$ for negative x, $-\hat{y}$ for positive x) is consistent with Ampere's

	Freq. (MHz)	Polarization	15 J Amp. (G)	200 J Amp. (G)
Lower Hybrid Wave	~ 1.5	Linear ($\sim 45°$)	$\ll 1$	< 1
RHI Waves	$0.2 - 5$	RCP	2	10
Shear Alfvén Wave	< 0.1	LCP	8	40

Table 5.1: Typical parameters for each of the three groups of waves observed in the experiment. The lower hybrid wave is either not generated in the 15 J experiment or is too weak to be distinguished from noise.

Law for a beam of positive ions moving in the negative z direction. This suggests that the shear wave may be driven by the slower expanding LPP bulk ions (Sec. 4.2).

5.2 Wave Polarization

The polarization of a wave, or the phase difference between the vector components of its electromagnetic fields, contains useful information. The handedness of a wave can sometimes be used to discriminate between different wave modes (Sec. 2.1), while the degree of ellipticity gives information about the wave's direction of propagation relative to the background magnetic field (only parallel-propagating waves are perfectly circularly polarized in the transverse plane). The most direct way to determine the polarization of a wave from a measured time trace vector magnetic field is with a hodograph plot. For each time t, the vector $\vec{B}(t) - \vec{B}(t - dt)$ is plotted on axes of B_X vs. B_Y, generating a circle or spiral pattern that shows the polarization and the degree of ellipticity of the wave. Fig. 5.5 shows a hodograph for a portion of the magnetic field signal shown in Fig. 5.1a. Over the time range shown, the wave is nearly perfectly RCP.

Hodographs offer the most direct visualization of polarization, but they quickly become cluttered when viewing many wave periods. An alternative visualization technique is a polarization decomposition, in which the measured magnetic field is represented in a basis of LCP and RCP basis vectors [118]. These basis vectors can be defined in terms of the

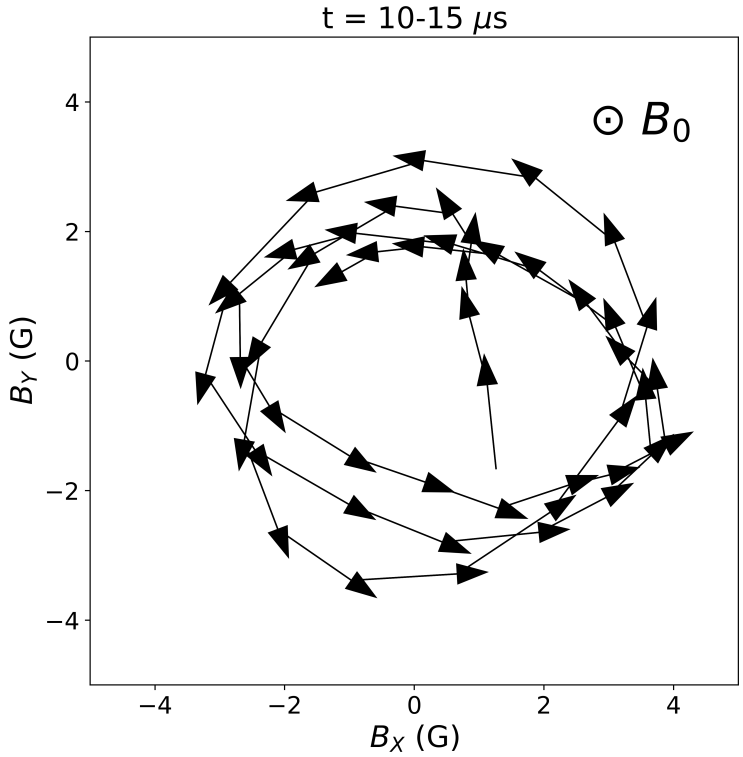

Figure 5.5: A hodograph of a portion of the transverse magnetic field signal shown in Fig. 5.1a shows that the sense of rotation is counter-clockwise and therefore that the wave is right-hand circularly polarized. Note that the background magnetic field is pointing out of the page.

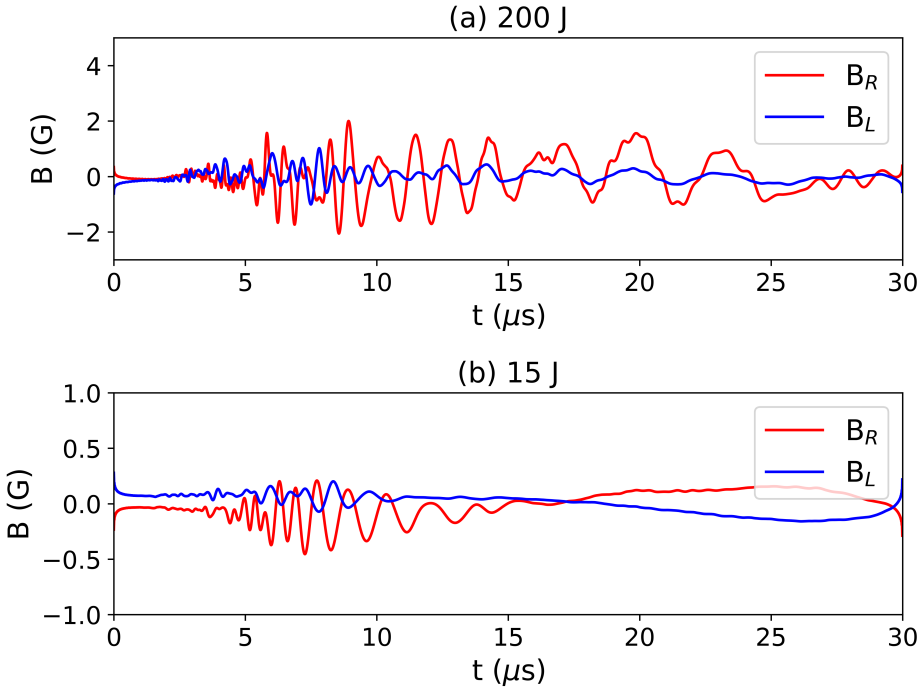

Figure 5.6: A polarization decomposition of the transverse magnetic field signals shown in Fig. 5.1 shows that the waves produced by both the 200 J (a) and 15 J (b) lasers are dominantly right-hand circularly polarized.

Cartesian basis vectors in frequency space

$$|RCP\rangle = \hat{x} + i\hat{y} \tag{5.2}$$

$$|LCP\rangle = \hat{x} - i\hat{y} \tag{5.3}$$

This relationship only holds for positive wave frequencies. It is also only possible in the frequency domain, since in the temporal domain the phase relationship between $\hat{x}$ and $\hat{y}$ depends on the wave frequency. If the Fourier transform of the measured transverse magnetic field is

$$F(B) = \tilde{B} = \tilde{B_X}\hat{x} + \tilde{B_Y}\hat{y} \tag{5.4}$$

then the RCP and LCP components of the magnetic field can be written

$$\tilde{B_R} = \frac{1}{2}(\tilde{B_X} + i\tilde{B_Y})|RCP\rangle \tag{5.5}$$

$$\tilde{B_L} = \frac{1}{2}(\tilde{B_X} - i\tilde{B_Y})|LCP\rangle \tag{5.6}$$

Applying the inverse Fourier transform (setting all negative frequencies to zero) then produces a signal in the time domain separated into RCP and LCP components. The relative magnitude of the signals corresponds to the ellipticity of the wave: for a perfectly RCP wave $\mathrm{Max}(B_R) = \mathrm{Max}(B_X) = \mathrm{Max}(B_Y)$ and $B_L = 0$.

Fig. 5.6 shows a polarization decomposition of the signals from Fig. 5.1. The waves generated by both lasers are predominantly RCP with a non-zero LCP component that may due to an oblique propagation angle. In both cases (but most notably for the 200 J measurement) the waves are not perfectly circularly polarized early in time but become almost entirely RCP at later times.

	200 J
$q_c/\|e\|$	+1
m_c/m_p	4
v_A (km/s)	100
n_c/n_e	0.935
q_b/q_c	3,4,5,6
m_b/m_c	3,3,3,3
n_b/n_e	0.02, 0.03, 0.01, 0.005
v_b/v_A	2, 3.5, 4.1, 4.65

Table 5.2: Parameters for the multi-species dispersion relation solution overplotted on Fig. 5.7a.

5.3 Spectral Analysis

The frequency spectrum of the waves can be determined from the measured time traces using the Fast Fourier Transform (FFT) algorithm [99]. The measured spectrum is directly compared to predictions from linear theory and is found to be consistent with waves generated by the RHI (Sec. 5.3.1). The time dependence of the spectrum is determined using the moving-window Fourier transform technique and the resulting arrival times measured for each frequency are used to validate the wave dispersion relation (Sec. 5.3.2). The arrival times of each frequency also contain evidence of wave reflection occurring near the end of the LAPD (Sec. 5.3.3).

All of the spectra presented here are most accurate far from the target where frequency dispersion has temporally separated the frequency components. The wave frequencies are close to the maximum frequency response of the magnetic flux probes, so aliasing effects may be present closer to the target where waves of different frequencies more closely overlap.

5.3.1 Frequency Spectra: The Fast Fourier Transform

For a time series of N points recorded with a $1/dt$ sampling frequency, the FFT algorithm provides the signal spectrum from $f_{min} = 0$ to the Nyquist frequency $f_{max} = 1/2dt$ with a spectral resolution of $\delta f = 1/Ndt$. Measurements digitized with the LAPD's high-resolution

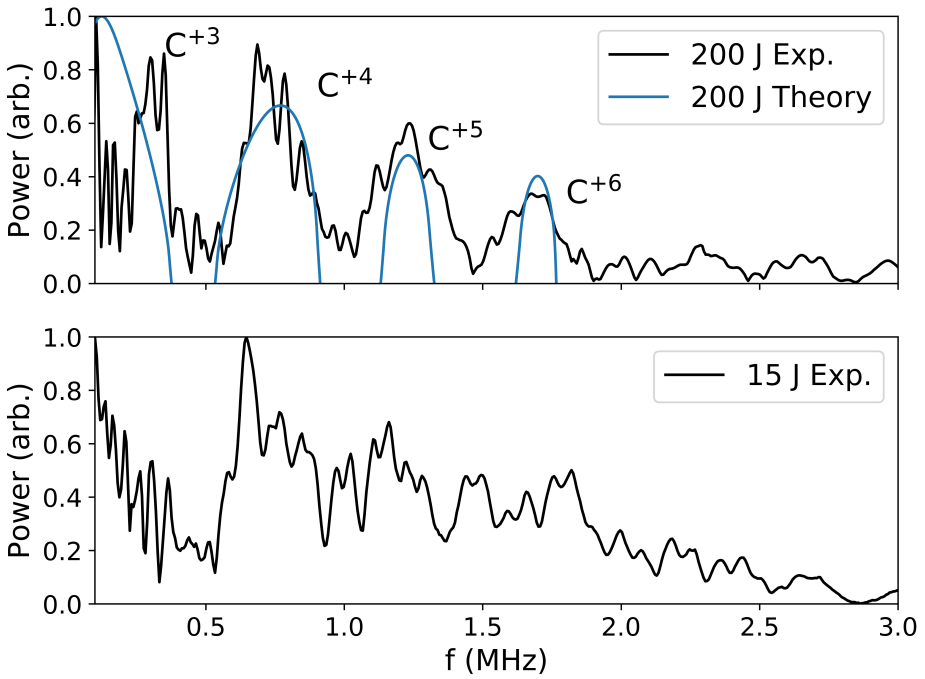

Figure 5.7: Fourier spectra of the B_Y signals shown in Fig. 5.1 show waves over a range of frequencies in both experiments. Predicted growth rates from linear theory (overplotted) show that these measurements are consistent with excitation of the RHI by various carbon charge states.

digitizer ($N \sim 10^5$, $dt = 0.8$ ns) can therefore nominally provide a spectral resolution of $\delta f \sim 12$ kHz up to $f_{max} \sim 600$ MHz. However, the magnetic flux probes used to make these wave measurements respond linearly only up to several MHz, so measurements at higher frequencies are difficult to interpret. Since the phenomena observed are transitory, the theoretical lowest non-zero frequency resolved is greater than δf. The duration of the wave features observed is approximately $\Delta t < 10$ μs, so an actual reasonable lower frequency bound is $1/\Delta t \sim 100$ kHz (since different wave features have different durations, the actual lower-bound frequency depends on the the signal being analyzed).

Figure 5.7 shows the output of this algorithm for the example magnetic field traces displayed in Fig. 5.1. Measurements made with both lasers show several peaks in the frequency range $0.5 - 3$ MHz. Comparison of the spectrum from the 200 J laser experiment to a theoretical prediction shows that each of the peaks corresponds to a different charge state of carbon present in the LPP. The theoretical wave spectrum (Fig. 5.7a, blue) is calculated by solving the multi-species dispersion relation (Eq. 2.9) with a set of reasonable plasma parameters estimated from experimental measurements (Table. 5.2) to calculate the RHI growth rate as a function of frequency. Since the RHI only grows where the growth rate is positive, the frequencies corresponding to maxima in the growth rate should correspond to the frequencies of the waves generated in the experiment. Since larger growth rates lead to higher amplitude waves (assuming that the times over which waves can grow at each frequency are similar), the relative amplitudes of peaks in the measured spectrum should also be correlated to the relative amplitude of peaks in the theoretical growth rate. The agreement between the maxima of the predicted growth rate and the peaks of the measured frequency spectrum in Fig. 5.7a is strong evidence that these waves are created by the RHI.

5.3.2 Time-Dependent Spectra: The Moving-Window Fourier Transform

The time dependence of the wave frequency spectrum can be studied using a moving-window Fourier transform (MWFT) and displayed as a spectrogram (Fig. 5.8). To create a MWFT,

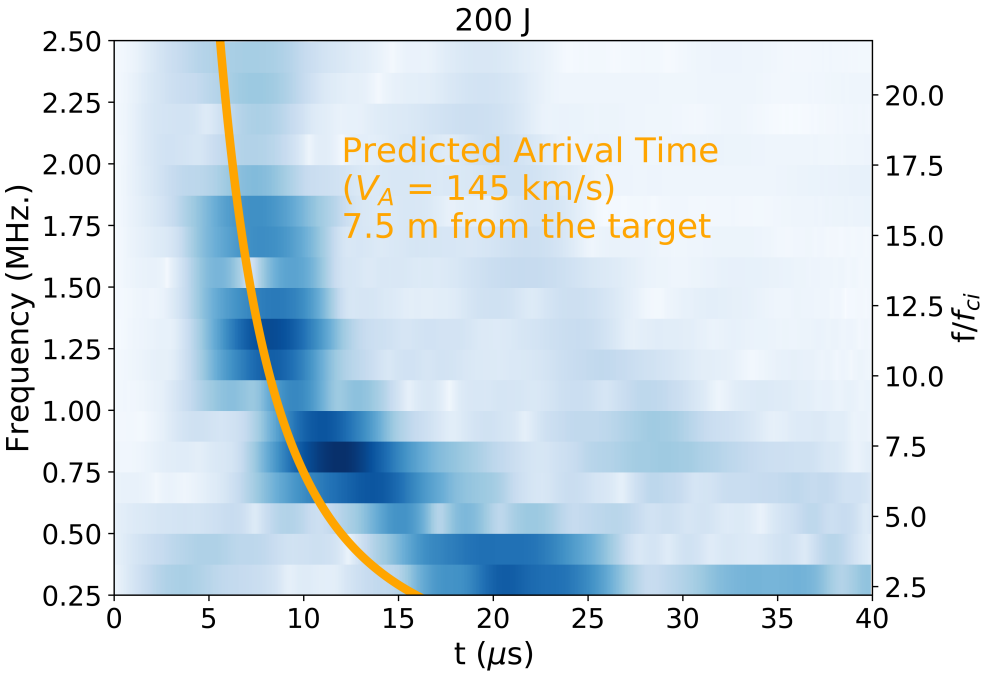

Figure 5.8: A spectrogram of experimentally-measured waves in the transverse magnetic field calculated using a moving-window Fourier transform (MWFT) (blue) shows a chirped wave packet. The MWFT window is 10 μs wide and moved in increments of 100 ns. The arrival time of the chirp matches the predicted group velocity determined from the dispersion relation (orange) for higher frequencies, but lower-frequency waves arrive more slowly than expected.

a window of width w in time is moved across the time series in increments of Δw, where typically $\Delta w \ll w$. The FFT is then calculated at each time step after a Gaussian mask is applied to the window to minimize artifacts due to spectral leakage at the window edges.

Choosing the window width requires a compromise between the minimum resolved frequency and the spectrogram temporal resolution. Since the window includes only a subset of the time series, the spectral resolution (and therefore the lowest resolved non-zero frequency) achieved is lowered to $\delta f = 1/wdt$. Larger windows are therefore required to resolve lower frequencies. On the other hand, smaller windows increase the temporal resolution of the spectrogram. The temporal resolution δt is technically wdt but may be somewhat higher in practice due to the Gaussian window profile. A reasonable approximation based on the $1/e$ width of the Gaussian mask is therefore $\delta t \approx dtw/3$

For the wave measurements presented here in the range $0.1 - 3$ MHz with $dt = 0.8$ ns, a window size of $w = 10^4$ is used, corresponding to a lowest resolved frequency of 125 kHz and a temporal resolution of $\delta t \approx 3$ μs. The window is moved in steps of $\Delta wdt \sim 100$ ns. The resulting spectrogram is shown in Figure 5.8. The spectrogram shows a chirp that begins at $\omega \approx 10\ \Omega_c$ then approaches $\omega = \Omega_c$ over a period of ~ 30 μs. The leading edge of the chirp arrives at the same time as the fastest LPP ions. Several peaks are observed at different frequencies, which correspond to the peaks generated by different LPP charge states described in Sec. 5.3.1.

The arrival time of each frequency of wave can be predicted using the dispersion relation for a wave carried by the core plasma (Eq. 2.16). The group velocity of a wave is $d\omega/dk$, and therefore the arrival time at a probe a distance d from the laser target (assuming the wave begin at the target at t=0) is

$$t_{arr} = d\left(\frac{d\omega}{dk}\right)^{-1} \tag{5.7}$$

A best fit prediction using this model with $v_A \sim 145$ km/s (estimated experimentally) and

$d = 7.5$ m is overplotted on Fig. 5.8. The arrival time of higher-frequency waves ($f/f_{ci} > 10$, arrival time < 8 μs) agree well with theoretical predictions, suggesting that the waves are in fact generated in a small region near the target and propagate dispersively as described by Eq. 2.16. The lower-frequency waves arrive slightly later than predicted, which could be explained if these waves propagate obliquely (leading to a longer effective propagation path).

5.3.3 Isolating Frequencies: Fourier Filtering

Another way of studying the time dependence of different frequency components is to apply a narrow bandpass filter to a signal in frequency space, then transform back into the time domain by applying the inverse FFT. This process is called a Fourier Filter. The bandpass filter shape (or "mask") used must be smooth to prevent broadband spectral leakage associated with sharp edges. Common choices include the Hanning or Hamming windows.

An example wave measurement FFT-filtered around 1 MHz is shown in Fig. 5.9a. This measurement shows both the primary packet of waves and a secondary packet of lower amplitude. The arrival time of both packets varies as a function of distance from the laser target (Fig. 5.9b), and the pattern of those arrival times suggests that the secondary wave packet is a reflection of the primary wave packet. Extrapolating from these measurements shows that the reflection occurs approximately 14 m from the laser target, which is approximately coincident with the anode for the LAPD's LaB_6 cathode.

5.4 Spatially-Resolved Measurements

Spatially-resolved measurements can be made using an array of many probes on a single laser shot or by scanning one or more probes through different positions across multiple shots. The latter method can provide higher spatial resolution, but is only possible for highly repeatable phenomena. Both techniques are used to study the RHI waves generated in these experiments.

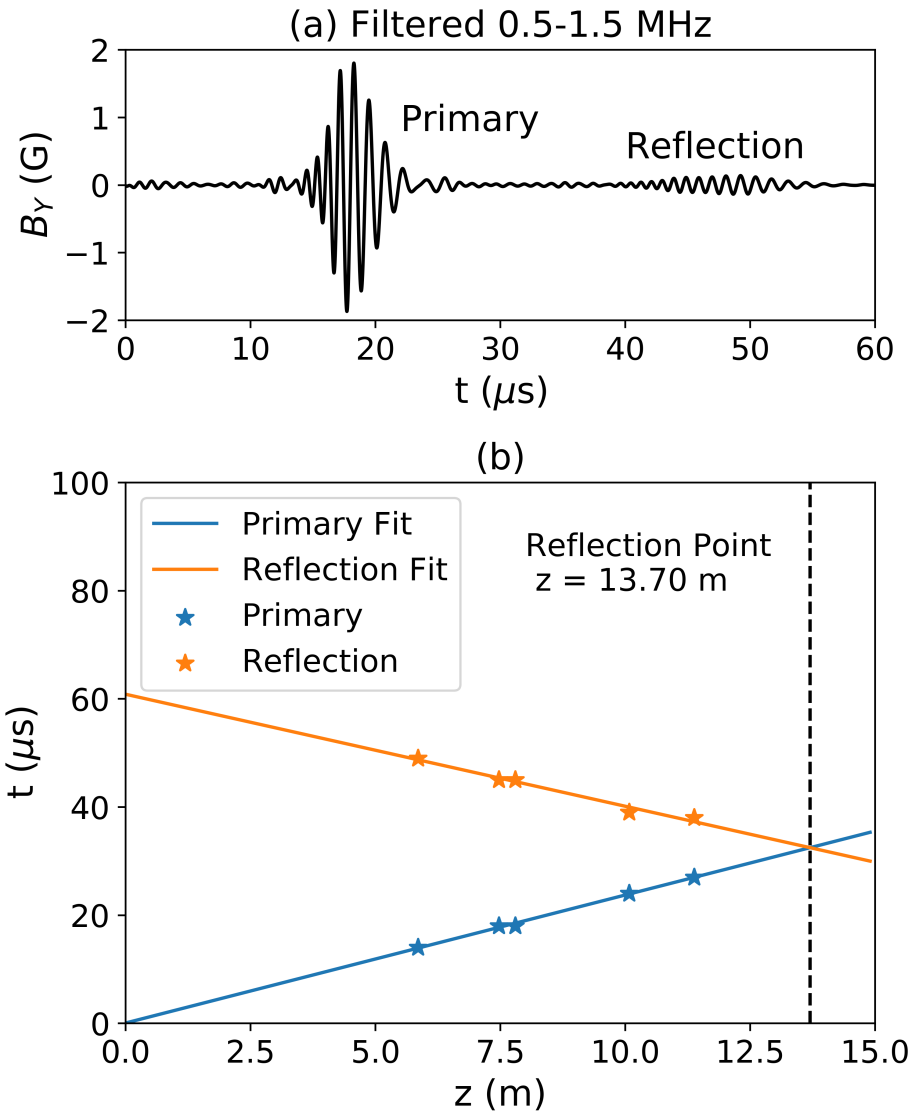

Figure 5.9: a) An example magnetic flux probe signal FFT-filtered to include only frequencies in the range 0.5-1.5 MHz. Two separate pulses are observed, corresponding to an initial wave packet and its reflection. b) Arrival times of the primary wave packet (blue) and its reflection (orange) are used to infer a reflection point of $z \approx 14$ m from the laser target, which is consistent with the location of the anode for the LAPD's LaB_6 cathode.

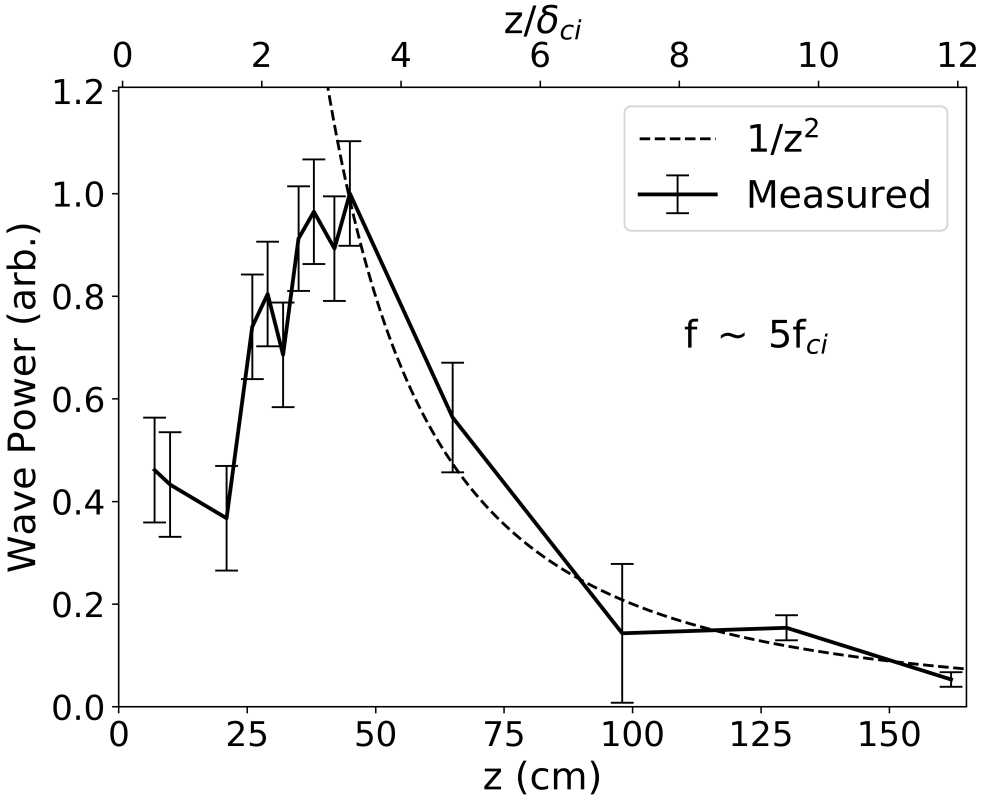

Figure 5.10: Spatially-resolved measurements of the maximum wave amplitude achieved around one of the RHI frequency peaks show that growth of the RHI is constrained to a region of $\sim$ 50 cm near the laser target. After this region, the wave amplitude decays as approximately $1/z^2$ consistent with spatial dispersion of the waves.

Measurements from an array of probes across multiple laser shots show that the growth of RHI waves is limited to a small region near the laser target (Sec. 5.4.1). Transverse planes comprising thousands of individual magnetic field measurements show that spatial structures in the transverse magnetic field and field-parallel current are associated with the observed waves (Sec. 5.4.2). A correlation analysis of two adjacent probes provides an experimentally-determined wave dispersion relation (Sec. 5.4.3).

5.4.1 Determining the Wave Growth Region

The times at which the RHI waves arrive at a distant probe suggest that the growth of the beam instability is limited to a small region near the laser target (Sec. 5.3.2). This hypothesis is confirmed by direct measurement of the wave amplitude at one of the RHI frequency peaks at increasing distances from the target (Fig. 5.10). An array of magnetic flux probes provides measurements farther from the target, while a single probe is moved between shots to obtain higher spatial resolution near the target. The RHI wave power is defined for each shot as the maxima of the signal in the RHI frequency band around $f \sim 5f_{ci}$. Shot-to-shot errors are quantified by repeating five shots at a each set of positions.

The RHI may be stabilized if the LPP density drops far below the background density (in which case the growth rate becomes negligible but remains non-zero) or when all of the free energy from sufficiently fast beam ions has been depleted. In these experiments, super-Alfvénic LPP ions are still observed far from the laser target [62], indicating that the LPP density is the factor limiting wave growth. The measured spatial dependence of the RHI wave amplitude is consistent with this explanation. The RHI wave amplitude begins low, then increases quickly between 25-50 cm ($2-5\delta_{ci}$) from the target. After this region the wave amplitude falls off as approximately $1/z^2$ as the waves spatially disperse. This observation can be explained by considering the density of the LPP as it expands away from the target. Near the target, the LPP is far more dense than the background plasma. In this region the roles of the beam and core plasma are effectively reversed (since by definition $n_b < n_c$), and the effective beam density is too low to appreciably drive the RHI. Between $25-50$ cm, the LPP has become less dense than the background plasma but is still dense enough for the RHI growth rate to be non-negligible, and substantial growth of the RHI is observed. After 50 cm the LPP has become too tenuous and the RHI stops growing, leaving the existing waves to slowly disperse.

5.4.2 Transverse Structure

The high repetition rate 15 J laser can be used to map the spatial structure of the vector magnetic field in planes transverse to the background magnetic field by moving the magnetic flux probes between shots (Fig. 5.11, arrows). Multiple shots (in the example shown, five) are averaged at each position. Some shot-to-shot variation in the wave amplitudes remains after averaging, manifesting as apparent spatial structures with spatial frequencies above the spatial sampling Nyquist frequency ($1/2\Delta x$ where Δx is the grid resolution). These structures are unphysical, and can be removed by applying a 2D low-pass spatial frequency filter to eliminate frequencies above the Nyquist frequency. It is notable that although there is shot-to-shot variation in the wave amplitudes, the phase of the waves is very nearly constant relative to the laser. This means that measurements from multiple shots can be averaged constructively without requiring a phase correction. The reason for this phase-locking is unknown, but may be related to the fact that the laser pulse (15 or 25 ns) is much shorter than the period of the observed waves ($0.1 - 1$ μs).

Measurements of the vector magnetic field can be used to calculate the plasma current. Ampere's law states that

$$\mu_0 \vec{J} = \nabla \times \vec{B} - c^{-2} \partial \vec{E} / \partial t \tag{5.8}$$

However, the displacement current (second term on the right) proves to be negligible. This simplification is essentially identical to the Darwin approximation [80] commonly made in electrodynamics. At a characteristic length scale L and time scale T, Faraday's law states that $E \approx -BL/T$. The ratio between the first and second terms can then be approximated as

$$\frac{c^{-2} \partial E / \partial t}{\nabla \times \vec{B}} \approx \frac{L^2}{c^2 T^2} \tag{5.9}$$

Characteristic length and time scales for the waves observed are their wavelengths ($\lambda \sim 1$ m) and periods ($T \sim 1$ μs), implying that the displacement current will be smaller than $\nabla \times \vec{B}$

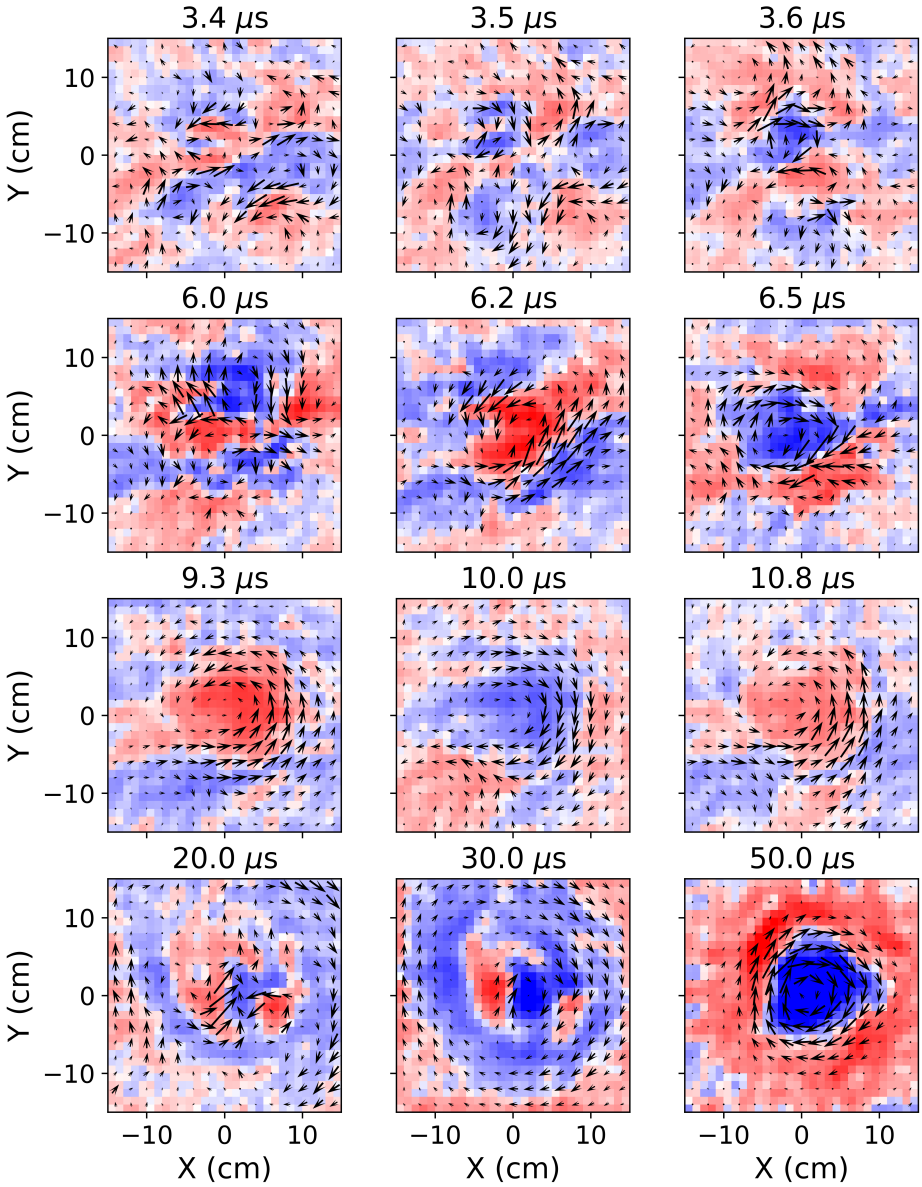

Figure 5.11: Full transverse planes of magnetic field (vectors) and derived field-parallel current (contours) recorded 7.5 m from the laser target at different times highlight different wave regimes. At early times (e.g. 3.4-3.6 μs) high frequency waves dominate and a number of current 'filaments' are observed which gyrate with the same sense as the electron gyromotion. Slightly later (e.g. 6.0-6.5 μs) the filaments grow larger. Eventually the filaments merge together to form a coherent axial cavity mode (e.g. 9.3-10.8 μs). After the RHI waves pass, a shear Alvfén wave is observed (20-30 μs) followed finally by a return current structure (50 μs).

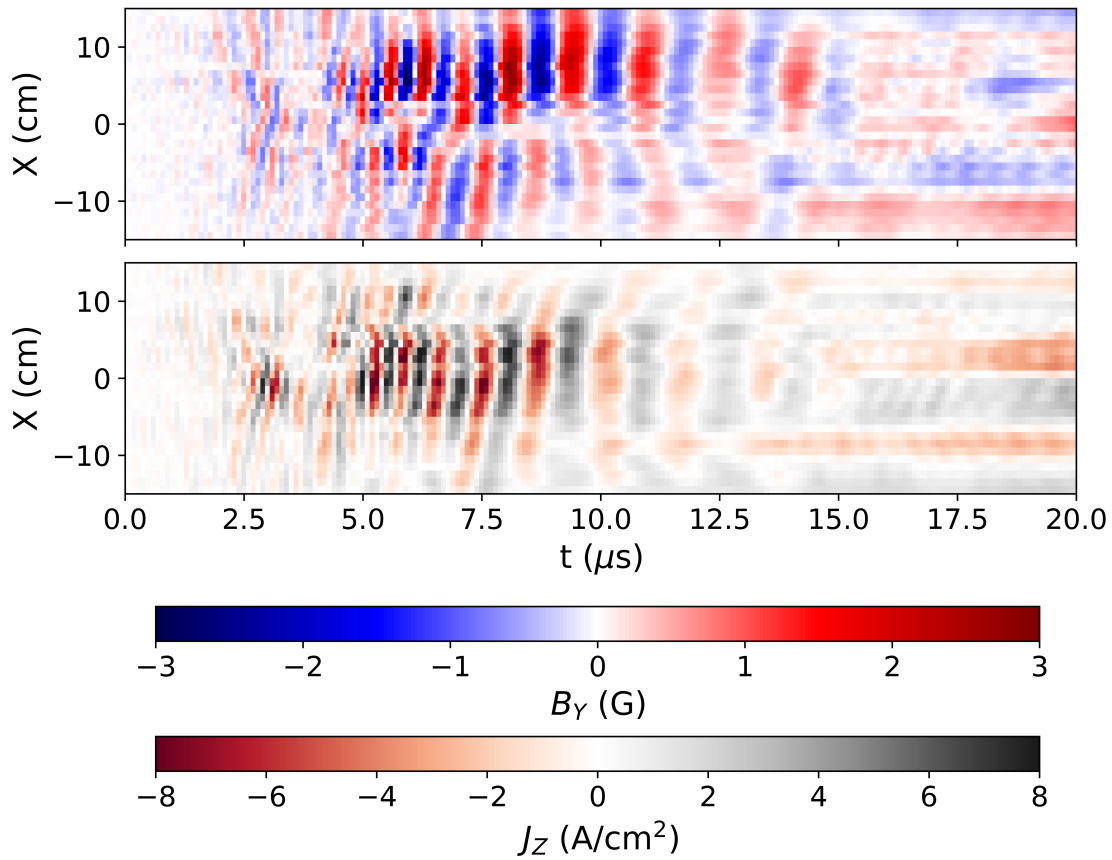

Figure 5.12: A transverse lineout at $y = 0$ streaked in time shows the temporal evolution of the wave magnetic field (top) and derived field-parallel current (bottom).

by a factor of $\sim 10^5$ and can therefore be safely neglected. In this case, the current is then

$$\vec{J} = \frac{1}{\mu_0} \nabla \times \vec{B} \tag{5.10}$$

The only component of J that can be calculated from a 2D plane of magnetic field measurements is the current normal to the plane. The transverse planes of measurements presented here can therefore be used to calculate the current parallel to the background field. It is important that unphysical high frequency structures from shot-to-shot variations be removed from the magnetic field measurements with a low-pass filter (as discussed above) prior to computing the curl to obtain physically meaningful results.

Figure 5.11 displays transverse planes of measured magnetic field (arrows) and calculated field-parallel current J_Z (contours) recorded 7.5 m from the laser target. Figure 5.12 shows a lineout of both B_Y and J_Z at $y = 0$ in the same plane streaked in time to show the temporal variations. Several distinct wave regimes are observed.

The first, from $2 - 8$ μs corresponds to the highest frequency RHI waves (if the lower-hybrid wave is produced by the 15 J laser at all, its amplitude is too low to be seen here). The spatial structure during this time is characterized by multiple current filaments. As time progresses, these filaments rotate in the plane in the direction of the electron gyromotion in the lab frame. As the wave frequencies arriving at the probe decrease, the filaments merge together and become larger. These filaments resemble those which have been predicted to form near quasi-parallel bow shocks [133, 92].

The second regime, from $8 - 14$ μs, corresponds to the arrival of lower frequency RHI waves. The spatial structure of the waves now resembles a coherent axial current that oscillates along the magnetic field. Although the direction of the current structure alternates at the frequency of the wave, the magnetic field polarization of the wave at a given spatial location is always right-handed. This structure may be explained by a cavity resonance [86] or ducting phenomenon [116] with a frequency cutoff possibly related to the diameter of the

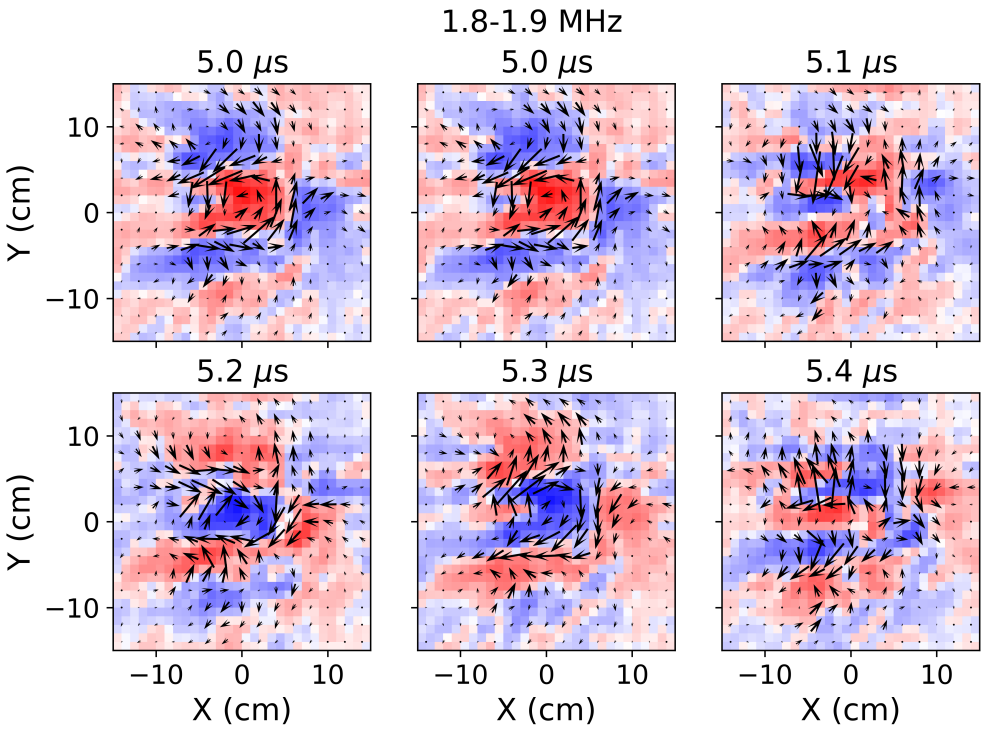

Figure 5.13: Applying a frequency-filter (1.8-1.9 MHz) to the transverse planes presented in Fig. 5.11 isolates the gyrating current filament regime.

background plasma.

The final wave regime observed from 30-50 μs corresponds to the shear Alfvén wave. The spatial structure of this wave is also an axial current channel, but since the Alfvén wave observed is a soliton, the structure does not oscillate. This pattern is consistent with previous measurements of Alfvén waves driven by expanding LPPs [131].

The spatial structures shown in Fig. 5.11 are a combination of waves at many different frequencies. The dominant frequency slowly changes throughout the measurement, accounting for the change in spatial structure. However, the spatial structure due to a single frequency band can be isolated by FFT filtering the time traces at each point. In practice the current must be calculated from the unfiltered magnetic fields and FFT filtered separately, as the current due to a single frequency component is not guaranteed to be self-consistent. The results, shown for the high frequency current filament regime and the low frequency axial

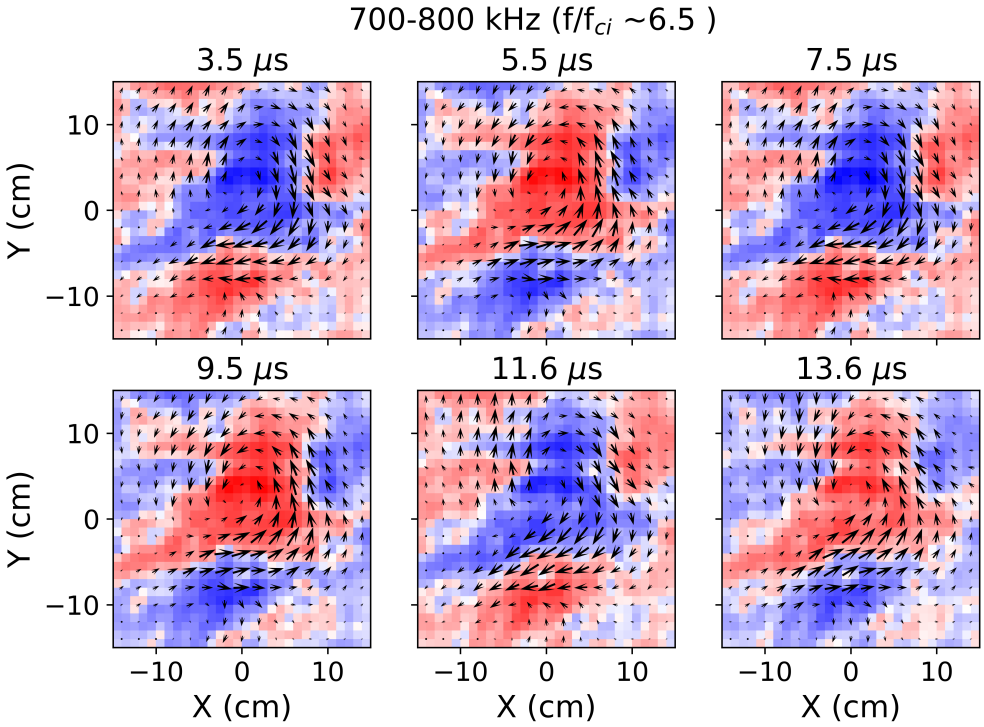

Figure 5.14: Applying a frequency-filter (700-800 kHz) to the transverse planes presented in Fig. 5.11 isolates the axial cavity mode regime.

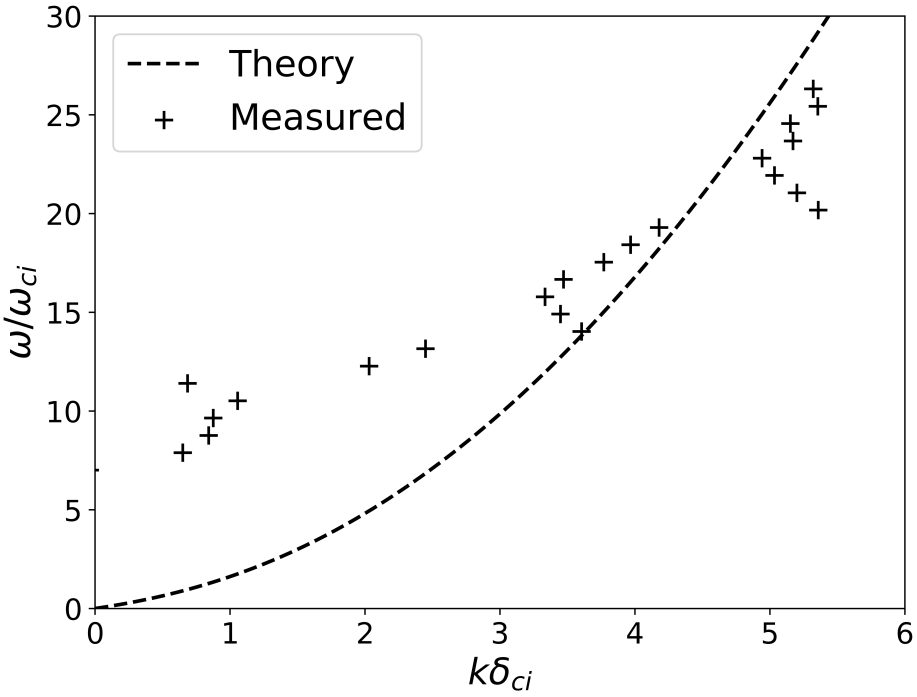

Figure 5.15: Experimental measurements of a parallel-propagating wave's dispersion relation can be made by comparing measurements from two probes separated in z. The discrepancy between this measurement and the theoretically predicted curve at lower frequencies ($\omega/\omega_{ci} < 15$) suggests that the low-frequency waves are obliquely propagating.

cavity mode regime in Fig. 5.13 and Fig. 5.14 respectively, show that the wave structure is constant in a given frequency band.

It is notable that all of the spatial features discussed here would be difficult to observe with a single spacecraft (or even a small cluster of spacecraft) as the time traces measurements throughout these planes are similar except for their phase. These types of measurements illustrate the potential for laboratory measurements to complement spacecraft observations.

5.4.3 Measuring Wavenumbers

Calculating the wavenumber $\vec{k}$ of waves measured over a range of frequencies allows an experimental dispersion relation to be calculated that can then be compared to theory to confirm the nature of the wave mode being observed. Measuring the vector components

of the wave number also gives information about the direction of propagation. The wave number can be calculated from the relative phase of waves observed by two or more probes separated by a distance $\vec{d}$ [111]. If only two probes are used, only the component of the wave vector parallel to $\vec{d}$ can be determined.

Consider two monochromatic time series with frequency ω_0 measured by probes separated by a distance $\vec{d}$. These time series can be expressed as

$$f_1(0,t) = A_1(t)e^{i(\omega_0 t)} \tag{5.11}$$

$$f_2(d,t) = A_2(t)e^{i(\omega_0 t - \vec{k}\cdot\vec{d})} \tag{5.12}$$

where $A_1(t)$ and $A_2(t)$ are arbitrary envelope functions. The phase of the signals differs by a phase shift

$$\phi_0 = \vec{k}\cdot\vec{d} = k_{\|}|\vec{d}|\cos(\theta) \tag{5.13}$$

where $k_{\|}$ is the component of the wave vector parallel to $\vec{d}$ and θ is the angle between $\vec{k}$ and $\vec{d}$. The phase shift ϕ can be can be calculated by computing the cross-correlation coefficient either in the time or frequency domain [111]. In practice this computation is most easily done in the frequency domain, where

$$C(\omega) = F_1(0,\omega)F_2^*(d,\omega) = \kappa^2 e^{i\phi(\omega)} \tag{5.14}$$

where $F_1(0,\omega)$ and $F_2(d,\omega)$ are the Fourier transforms of the time series, * denotes the complex conjugate, κ is the coherence length scale, and $\phi(\omega)$ is the phase difference between the signals as a function of frequency. The phase difference $\phi(\omega)$ can then be expressed as

$$\phi(\omega) = \arctan\left(\frac{\mathrm{Im}(C(\omega))}{\mathrm{Re}(C(\omega))}\right) + n2\pi \tag{5.15}$$

where $n = 1, 2, 3....$ For a monochromatic wave, the phase shift $\phi_0 = \phi(\omega_0)$. If ω_0 is unknown,

it can be calculated as

$$\omega_0 = \mathrm{Max}(|C(\omega)|) \tag{5.16}$$

since for a monochromatic wave $C(\omega) = \delta(\omega_0)$. Equation 5.13 can then be used to calculate ϕ_0 and, given $\vec{d}$, $k_\parallel$.

In practice, wave measurements are typically not monochromatic and must therefore be FFT-filtered around a narrow frequency band before applying this technique. If a signal does contain a wide band of frequencies, this method can be repeated to determine the wavelengths at a variety of frequencies and therefore an experimentally-measured dispersion relation from a single set of time series. Observing phase discontinuities due to the 2π ambiguity in Eq. 5.15 also allows the phase measurements to be "unwrapped", allowing measurements of waves with $\lambda < |\vec{d}|$ that would otherwise be ambiguous. No phase jumps should occur for $\lambda > |\vec{d}|$. The unwrapping process is cumulative, so a single incorrect phase will affect all subsequent values.

An experimentally-determined dispersion relation for the RHI waves is shown in Fig. 5.15. Time series measurements of magnetic field fluctuations were made using two magnetic flux probes separated by $\vec{d} = 32.5$ cm $\hat{z}$ at a distance of 7.5 m from the laser target. The resulting waves are observed in the band 0.5-3 MHz, which were Fourier filtered into 400 kHz wide bands prior to calculating the wavenumber. Comparing the results to the dispersion relation derived from linear theory (Fig. 5.15, dashed) shows that the experimental measurements agree with theoretical predictions at higher frequencies ($\omega/\omega_{ci} > 15$) but consistently show smaller wavenumbers than predicted at lower frequencies ($\omega/\omega_{ci} < 15$). This observation suggests that the lower-frequency waves are obliquely propagating, so that $|\vec{k}| \neq k_\parallel$ in Eq. 5.13. If the entire discrepancy is explained by oblique propagation, than these results are consistent with a propagation angle of $\theta \sim 70^\circ$ for the low frequency waves.

The observation of such highly oblique waves so far from the target would imply that the waves undergo reflection as they propagate, possibly off of the density gradients at the edges

of the core plasma. A wave following such a path would travel more slowly along the machine (since the effective wave propagation path is longer), corresponding to a slower arrival time than expected on probes far from the target. This is consistent Fig. 5.8, in which the arrival times of high frequency waves agree well with theoretical predictions, while lower frequency waves ($f/f_{ci} < 10$, observed after ~ 8 μs) arrive more slowly than expected. The separation between these high and low frequency regimes corresponds to the transition between the gyrating current filament regime and the axial cavity mode regime shown in Fig. 5.11. The wavenumber separating these regimes, $k\delta_{ci} \sim 2.5$, corresponds to a wavelength of $\lambda \sim 50$ cm, which is approximately the diameter of the LAPD core plasma. This observation further supports the interpretation that the change in spatial structure and wave propagation angle at low frequencies is due to interactions with LAPD plasma density gradients.

5.5 Parametric Variations

The growth rates of ion/ion beam instabilities, and the frequencies and wavelengths of the waves they generate, depend on the velocities and densities of the beam plasma and core plasma as well as the strength of the background magnetic field (Sec. 2.2.1). These parametric dependencies have been investigated experimentally by measuring the RHI wave amplitude while varying the parameters of the core plasma (Sec. 5.5.1) and the beam plasma (Sec. 5.5.2).

5.5.1 Core Plasma Parameters

The growth rates, frequencies, and wavenumbers predicted for the RHI by linear theory are scaled to the core ion cyclotron frequency and ion inertial length. Varying the core plasma parameters will therefore change the properties of the observed waves. This is accomplished experimentally by changing the core plasma density and magnetic field magnitude. However, varying these parameters also changes other aspects of the experiment. Varying the core

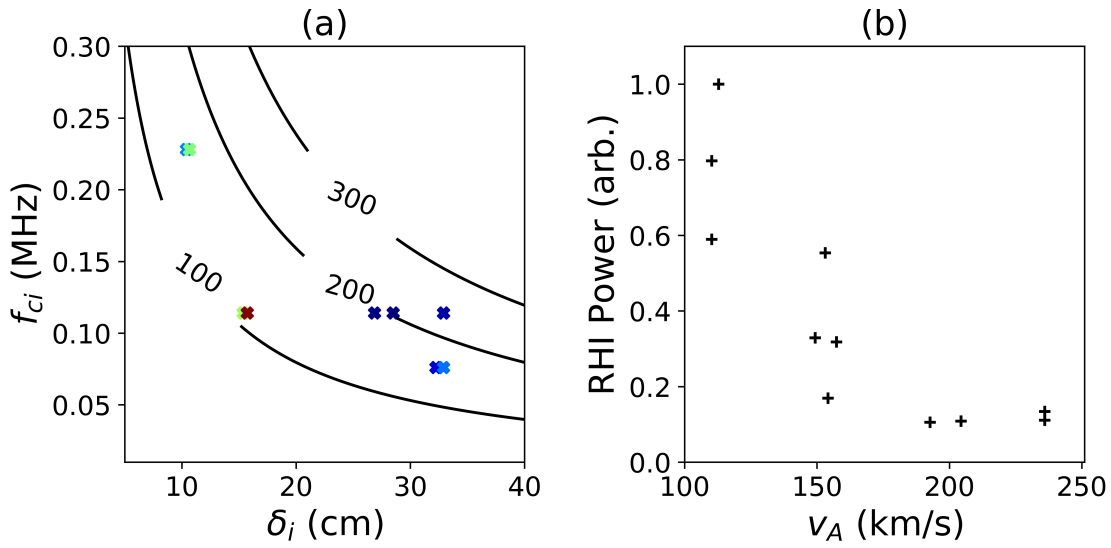

Figure 5.16: a) The maximum wave amplitude (marker colors) within the RHI frequency range measured for individual 200 J laser shots over a range of dimensionless core plasma parameters f_{ci} and δ_i. Contours of v_A are included for reference. b) Sorting the points by v_A shows that higher wave amplitudes are broadly correlated with lower v_A and therefore, since v_b was not varied, higher M_A.

density changes the beam density relative to the core density (which also changes the RHI growth rate) and changing the Alfvén velocity in the core plasma changes the beam's Mach number.

Figure 5.16a shows the amplitude of the RHI waves (in a narrow frequency band $f \sim 5f_{ci}$) driven by the 200 J laser at different core plasma densities (ion inertial lengths) and magnetic fields (ion cyclotron frequencies). Varying either of these parameters changes the Alfvén velocity, the value of which is plotted as contours.

For each shot the nominal ambient magnetic field magnitude in the experimental region was recorded. The ion density was calculated using the LAPD's microwave interferometer array. However, measurements of the core plasma profile, and thus the effective interferometer path length, l_{eff}, were not made at each density. The core plasma radial density profile is expected to become smaller as the magnetic field in the experimental region is increased (because the magnetic field at the cathodes is kept the same). Since $l_{eff} \sim 25$ cm was mea-

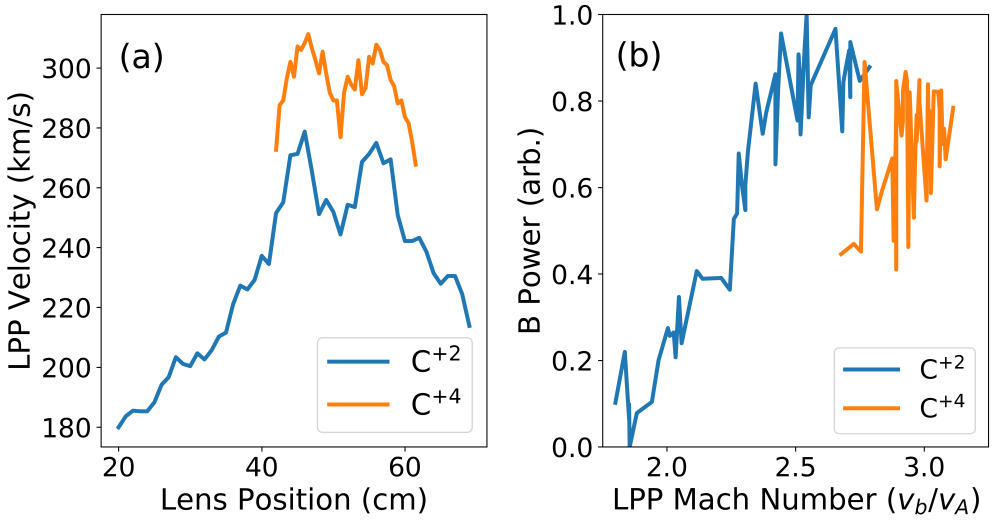

Figure 5.17: Scanning the position of the final laser focusing lens varies the peak LPP velocity as shown by time-of-flight ion fluorescence measurements (a). Two separate runs were conducted measuring C^{+2} and C^{+4} ion velocities. The final focusing lens is angled to control surface reflections, introducing an astigmatism that creates two separate foci. Over the range of velocities measured, the power in the RHI frequency band is approximately linear with the leading edge beam velocity (b).

sured with a background field of 300 G, we assumed the following scaling for the remaining magnetic fields

$$l_{eff} \approx 25 \text{ cm} \left(\frac{B}{300 \text{ G}} \right) \tag{5.17}$$

The results show substantial variability even between shots which should be nominally identical. This shot-to-shot irreproducibility could be due to the estimation of the core plasma density, or to shot-to-shot variations in the laser energy and/or intensity. However, a correlation does appear to hold between the RHI amplitude and lower Alfvén velocities (Fig. 5.16b). Since v_b was not varied, this observation is consistent with the expectation that higher Mach numbers should lead to a higher RHI growth rate.

5.5.2 Beam Plasma Parameters

Linear theory shows that the growth rate of the RHI depends strongly on the velocity and density of the beam ions relative to the core ions (Sec. 2.2.1). These parameters can be varied experimentally by changing the intensity of the laser (primarily controlling the LPP velocity) or the energy of the laser (primarily controlling the number of LPP particles, and therefore the density) [54, 104]. The current series of experiments have focused on the former.

To measure the dependence of the RHI growth rate on the LPP velocity, the wave amplitude at a fixed location and frequency is measured while the focal spot size is systematically varied (to change the laser intensity on target) by translating the final focusing lens. At the same time, the velocity distribution of a single beam ion species is independently measured for each shot by time-of-flight (assuming the LPP starts at the target at $t = 0$) using time-resolved monochromator measurements of ion fluorescence. The focusing lens is intentionally angled to control lens ghosts, introducing some astigmatism. As the lens translates, the intensity therefore passes through two maxima corresponding to separate horizontal and vertical foci (Fig. 5.17a). The measurement shown at each lens position is an average over ten laser shots.

For each velocity distribution, a characteristic maximum velocity is defined by the leading edge at 25% rise. Fig. 5.17a shows the velocity of two species of carbon as a function of lens position, clearly showing the two separate foci. The velocities of both species have a similar dependence on intensity, though the higher charge state is always faster. This result is consistent with the findings of previous LPP characterization experiments [104].

The waves generated during the same shots are measured by a magnetic flux probe. Fig. 5.17b shows the maximum wave amplitude in one of the RHI frequency bands ($3.5 - 5.5 f_{ci}$) sorted by and plotted against the corresponding measured leading-edge LPP velocities. In this regime the maximum RHI amplitude is proportional to v_b. For the velocity ranges measured this scaling is consistent with the growth rate predicted by solving the lin-

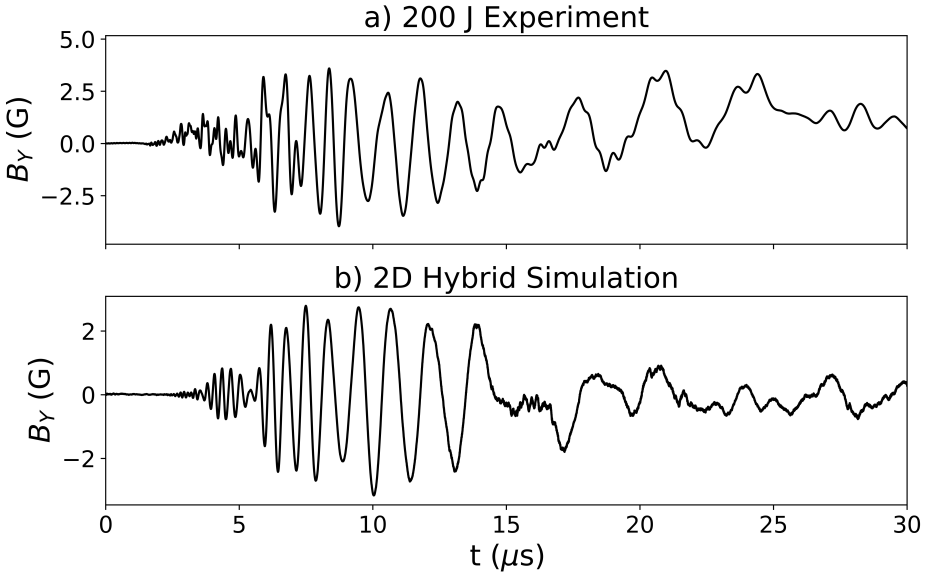

Figure 5.18: a) A measurement of B_Y from a magnetic flux probe 7.5 m from the target in the 200 J experiment. b) B_Y recorded by a corresponding virtual magnetic flux probe in the 2D hybrid simulation of the experiment. Simulation results provided by Martin Weidl.

ear dispersion relation (Eq 2.15). The LPP density in the growth region was not measured, but linear theory predicts a relatively weak dependence on density at low Mach number and densities $\geq 5\%$ [62].

5.6 Comparison to 2D Hybrid Simulations

The formation of parallel shocks in space is often simulated using a hybrid model, which models ions kinetically with a particle-in-cell approach while approximating electrons as an inertia-less fluid. This approximation is necessary to make the simulation of kinetic ion dynamics computationally feasible over the long length scales ($100\delta_{ci}$'s) required for parallel shock formation, and is valid for the frequency and length scales of interest (near ω_{cc} and δ_{ci}). In order to further reduce computational requirements, such simulations are often run in 1D or 2D, neglecting one or both of the dimensions transverse to the background magnetic field.

One goal of the experiments presented here was the validation of a 2D hybrid code discussed in detail in previous work [135, 134, 137]. In order to make a direct comparison, the code was used to run a simulation of the experiment that included a beam of two carbon charge states (C^{3+}, C^{4+}) interacting with a helium background plasma.

The laser-target interaction is not simulated: instead, the LPP is initialized as it appears shortly after ablation. Each beam quasi-particle is initially randomly placed in a 'target area' of 0.5 $\delta_{ci} \times 0.3\ \delta_{ci}$. In addition to a component derived from an isotropic Maxwellian distribution, the initial beam velocity includes a random 'blow-off' component $\vec{v}_{b0}$. The azimuthal angles (ϕ, around the z axis) of these velocities are uniformly distributed, while the polar angles are distributed with a probability distribution such that $p(\phi)d\phi \propto \cos^4\phi d\phi$. The magnitude of the velocity is then chosen such that $|\vec{v}_{b0}| \propto \cos^2\phi$ and $\langle \vec{v}_{b0} \rangle = v_b \hat{z}$ where v_b is the desired LPP velocity. This approach is chosen to generate a simulated LPP velocity distribution consistent with previous characterization measurements [104, 61, 62]. The background plasma ions are uniformly distributed with zero bulk velocity (the density gradients of the LAPD background plasma are not modeled in the simulations presented here).

The simulation domain has a high aspect ratio (4 $\delta_{ci} \times 192\ \delta_{ci}$) to match the experiment geometry and is described here in the same coordinate system used to describe the experiment. The spatial and temporal resolutions are $\Delta x = \delta_{ci}/16$ and $\Delta t = \omega_{cc}^{-1}/2000$ respectively. The $\pm x$ boundaries are periodic for core ions but absorb beam ions to model beam losses to the vacuum chamber walls. Beam ions that cross these boundaries are not evolved on subsequent timesteps. Periodic boundary conditions for both beam and core ions are imposed at the $\pm z$ boundaries, although the simulation domain is chosen to be sufficiently long to prevent the fastest particles from reaching the boundary during the time range of interest. The simulation is performed in the laboratory reference frame (core ion velocity $v_c = 0$).

The magnetic field at several points throughout the simulation is recorded at each time

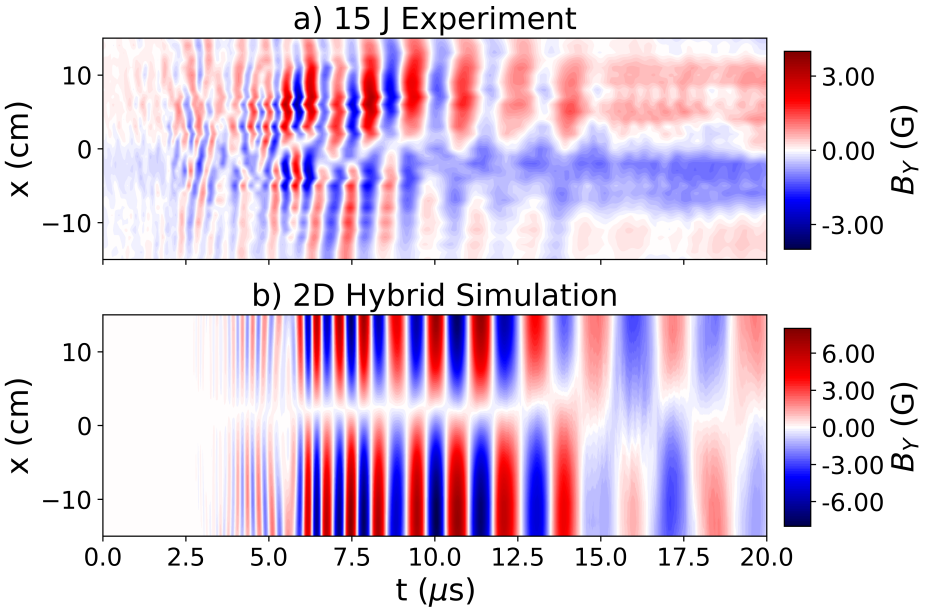

Figure 5.19: a) A transverse magnetic flux probe lineout made by a magnetic flux probe 7.5 m from the target during an experiment with the 15 J laser. b) A lineout from a corresponding virtual magnetic flux probe in the 2D hybrid simulation. Simulation results provided by Martin Weidl.

step to produce a time trace corresponding to that which would be measured by a probe at that location. The location of these 'virtual probes' is chosen to correspond to physical probes in the experiment. A comparison between a magnetic flux probe 7.5 m from the laser target and a corresponding virtual probe in the experiment 2D hybrid simulation is shown in Figure 5.18. The frequency, time-of-arrival, amplitude, and polarization (not shown) of the simulated waves agrees well with the experimental measurement. Some of the highest frequency waves observed in the experiment ($\omega \sim 15\ \omega_{cc}$) are not resolved by the simulation grid, which explains the absence of those waves in the simulated signal.

In order to compare the spatial structure of the waves in the simulation to the experiment, an array of virtual magnetic flux probes can be used to make a virtual transverse lineout. Virtual probes are positioned every 1 cm over a 30 cm distance centered at $x = 0$ and located 7.5 m from the laser target. This virtual lineout is compared to a corresponding experimental measurement in Figure 5.19. The simulation broadly correctly predicts the

frequencies and time-of-arrival of the waves. The wave amplitude is lower because the simulation was performed with a LPP corresponding to the 200 J laser. The spatial structure of the waves is similar until ~ 15 μs. At this point the structure of the wave in the experiment changes, while that of the simulated wave does not. This likely corresponds to the same cavity mode type structure seen in Fig. 5.11, which is not reproduced in the simulation because it does not model the density gradients at the edges of the background plasma. Note that the full transverse spatial structure of the waves is not simulated, so a direct comparison to a measurement like Fig. 5.11 is not possible without a full 3D simulation.

The conclusion of this comparison is that the relevant beam instability physics is well-reproduced by the hybrid code, provided sufficient grid and temporal resolution to resolve the wavelengths and frequencies of the waves.

5.7 Comparison to Spacecraft Measurements

Spacecraft passing through planetary bow shocks observe a wide variety of wave modes. In particular, a type of ultra-low frequency (ULF) wave, called 30-second waves based on their characteristic period in the Earth's bow shock, are often observed upstream of quasi-parallel shocks in the foreshock region. A sample of a 30-second wave recorded by the Wind spacecraft [141, 142] on 2002-08-10 at 19:01:40 Universal Time far upstream in the Earth's quasi-parallel foreshock at GSE (longitude, latitude, radius) = (5°, 2°, 20 R_E), where R_E is the radius of the Earth, is plotted in Figure 5.20. The wave's frequency and right-hand circular polarization are consistent with linear theory for the RHI.

These waves are qualitatively similar to the experimentally measured RHI waves presented here. However, a quantitative comparison is complicated by the fact that the carbon/helium interaction in the experiment produces waves with higher frequencies (scaled to ω_{cc}) than the proton/proton interaction present at the foreshock (Sec. 2.2.2). This discrepancy cannot be easily resolved by scaling [63, 64]. Future experiments utilizing a hydrogen

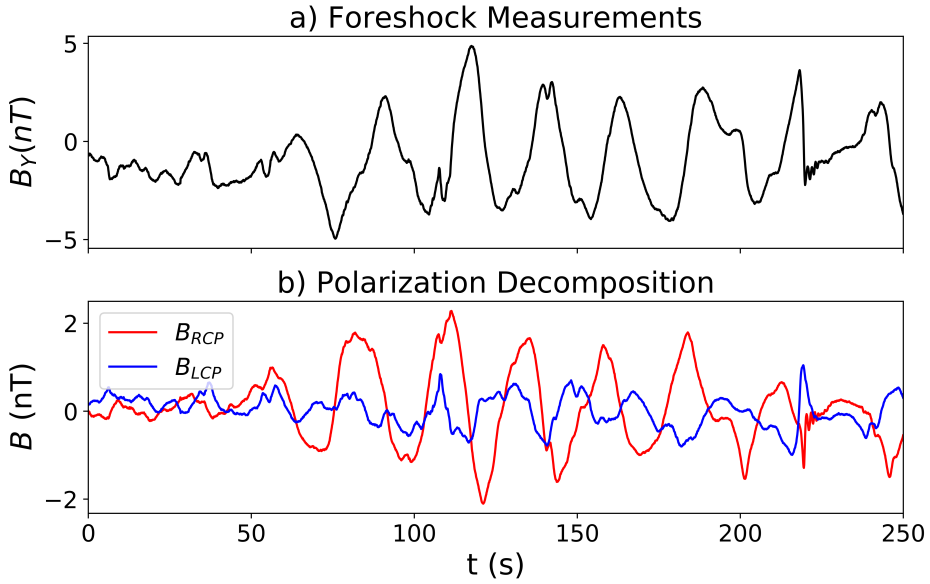

Figure 5.20: A sample of 30-second waves observed by the Wind spacecraft [78] in the Earth's foreshock far upstream of the quasi-parallel bow shock. The waves are named for their period (around 30 s) (a) and are right-hand circularly polarized (b). The wave are consistent with theoretical predictions for the RHI.

background plasma and LPP are the ideal solution to this problem, but present technical challenges. At present, this problem is best resolved by quantitatively comparing both spacecraft and laboratory measurements to corresponding simulations.

For this purpose, a simulation was run using the 2D hybrid code previously validated by the experimental measurements (Sec. 5.6). This simulation represents a small region ($20\ \delta_{ci} \times 256\ \delta_{ci}$) far upstream in the terrestrial quasi-parallel foreshock containing a proton beam plasma and a proton core plasma. The simulation parameters are chosen to match local plasma parameters as measured by the instruments on the Wind spacecraft [142]. Within this region, the beam and core plasmas are assumed to be spatially uniform and all boundaries are periodic. The beam quasi-particles are initially uniformly distributed with a drifting thermal/Maxwellian velocity distribution. The spatial and temporal resolutions are $\Delta x = \delta_{ci}/8$ and $\Delta t = \omega_{cc}^{-1}/1000$ respectively. The simulation is run in the spacecraft frame, in which both beam and core ions are moving to the right relative to the simulation window.

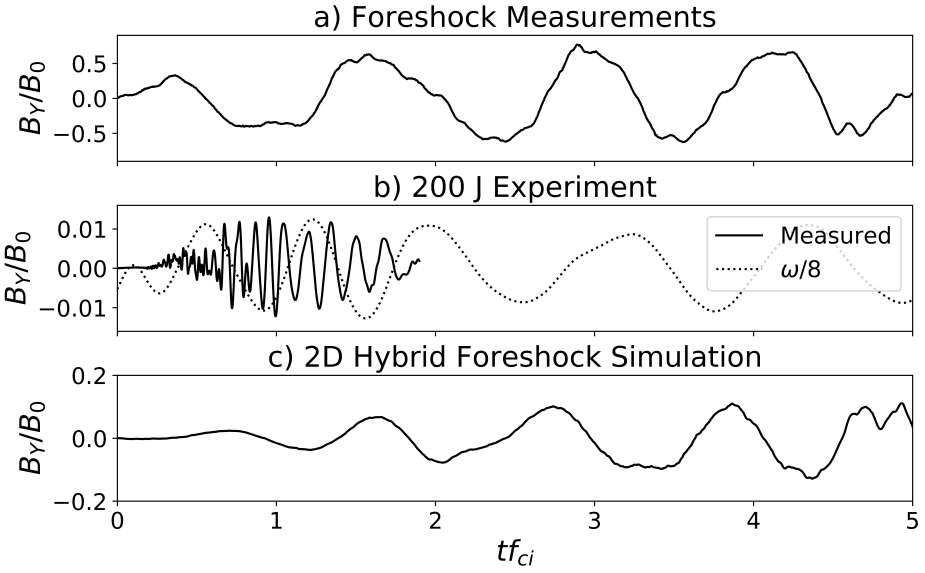

Figure 5.21: Samples of waves from the terrestrial foreshock [78] (a), the 200 J laser experiment (b,solid) and the 2D hybrid foreshock simulation (c) all normalized to the local core ion cyclotron frequency. The waves produced in the experiment are qualitatively similar but have $\sim 8\times$ higher frequencies due to the different ion species used.

Virtual magnetic flux probes are situated throughout the simulation domain to provide wave measurements that can be directly compared to spacecraft observations.

The resulting simulated waves are compared to measurements from the Wind spacecraft and the experiment in Figure 5.21. The simulation reproduces the waveform and frequency of the foreshock measurement. As predicted by linear theory, the experiment produces waves with a higher dominant frequency than those observed in space (when scaled to f_{ci}). However, re-scaling the time axis of the experimental data to correct for this factor shows that the waveform is otherwise similar.

The waves observed in the foreshock reach much higher amplitudes than those observed in the experiment. The foreshock simulation reaches larger amplitudes than the experiment, but also saturates before matching the amplitude of the spacecraft measurements. This occurs at a level determined by the starting energy of the system: in the foreshock inflowing particles continuously contribute additional energy, allowing wave growth to continue longer

than it does in the simulation. Incorporating these inflowing particles into the simulation to drive higher amplitude waves presents challenges and remains a subject for future work.

The agreement between the foreshock simulation and the spacecraft observations suggests that the RHI is responsible for driving the waves in both cases. Mutual comparison with the experiment simulations therefore leads to the conclusion that the waves created in the laboratory are created by the same physical mechanism as those produced far upstream in the terrestrial quasi-parallel foreshock.

CHAPTER 6

Directions for Future Work

Two primary challenges must be overcome in order to drive a quasi-parallel shock with a LPP. First, the LPP must remain dense and spatially uniform over a much longer length scale than achieved in the current experiments (100's δ_{ci} vs. $1-2\delta_{ci}$, Sec. 5.4.1) to allow more time for beam instabilities to develop and grow waves to non-linear amplitudes. Second, a sufficiently long core plasma (100's δ_{ci}) must be created to allow these waves the space to develop into a shock.

Improved laser drivers may be able to create better LPPs for parallel shock experiments by employing novel pulse shapes such as pulse trains (Sec. 6.1). Monte-Carlo calculations (Sec. 6.1.1) suggest that these pulse shapes can create more spatially uniform LPPs that maintain their density over longer temporal and spatial scales, providing more space for beam instabilities to grow. Simulations using the 2D hybrid code previously described in Sec. 5.6 show that applying this technique to the current experiments should substantially increase the amplitude of the waves generated into the nonlinear regime (Sec. 6.1.2). Attempting to better collimate the LPP using techniques such as shaped targets may also results in increased wave amplitudes, but Monte-Carlo calculations predict that only modest gains can be made with this approach (Sec. 6.2).

Improvements to the core plasma may also be able to contribute to LPP cohesion: heating the relatively cool LAPD electrons would reduce collisions with the beam ions and may substantially reduce beam ion cross-field transport (Sec. 6.3). Improvements that result in increased core plasma density would also reduce the core plasma ion-inertial length, effec-

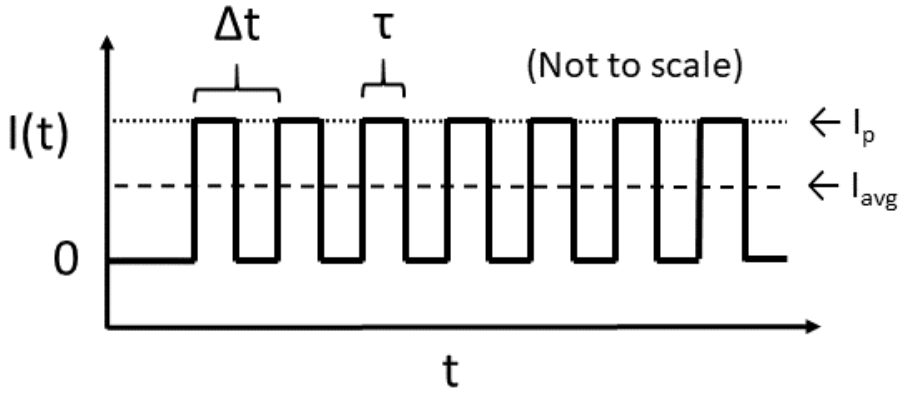

Figure 6.1: A conceptual "pulse train" pulse shape with $N = 7$ square pulses τ long separated by Δt each.

tively lengthening the experiment to allow sufficient space for shock formation.

Even if the combination of these approaches is not successful in creating a fully-formed quasi-parallel shock, some futher experiments could be conducted in the current linear regime (Sec. 6.4.1). A further set of experiments would be enabled by the ability to create large-amplitude non-linear waves without requiring a fully-formed shock. Measuring wave-particle scattering (Sec. 6.4.2), density fluctuations in the beam or core plasmas associated with these waves, or non-linear wave-wave interactions (Sec. 6.4.3) would all have direct relevance to the physics of quasi-parallel shock formation.

6.1 Laser Pulse Trains

An ideal laser driver for field-parallel beam instabilities (and therefore shocks) would produce a uniform and dense LPP that is extended in both space and time. In principle this could be achived by employing a long pulse length $\tau \geq 10$ μs with the same (or higher) intensity as the the experiments reported here ($I \geq 10^{12}$ W/cm^2). However, since the total laser energy is the time integral of the intensity, such a pulse would require a very energetic laser. Decreasing the intensity is not acceptable because this would reduce the LPP velocity [53],

which is also a critical requirement for beam instability growth and shock formation. A possible solution is the use of pulse shaping to produce a train of laser pulses separated in time [11, 121]. Using a series of short pulses rather than a continuous long pulse maintains high instantaneous intensity and therefore keeps the LPP velocities comparable to those achieved in the current single-pulse experiments.

A laser pulse shape can be described by an intensity function $I(t)$ that determines the amount of laser intensity as a function of time. A conceptual pulse shape of this type with $N = 7$ square pulses of width τ and a peak intensity of I_p separated by Δt is shown in Fig. 6.1. If the pulses are spaced sufficiently close together, their velocity distributions will cause them to merge together to form a quasi-continuous LPP: fast particles from one pulse will catch up with the previous pulse, while slower particles will fall back into the following pulse. The ideal pulse separation Δt therefore depends on the velocity distribution of the LPP created by each pulse.

In addition to extending the LPP in space, spreading the energy out in time may also allow the total laser energy, $E_{tot} = NI_p\tau$, to be increased. The maximum laser energy is limited by the damage thresholds of its optical components, which depend on the laser intensity. Experimental measurements show that the optical damage threshold D scales with the pulse width as $D \approx \alpha\tau^{0.5}$ where α is a proportionality constant [21, 102]. This empirical model has been developed for single pulses with widths in the nanosecond regime and wavelengths between $0.35 - 1$ μm (damage thresholds are higher at longer wavelengths).

If interactions between successive pulses can be neglected, a train of pulses can be considered as either a series of separate pulses, with width τ and intensity I_p or a single time-averaged pulse of width $\tau_{tot} \approx\sim N(\tau + \Delta t)$ and intensity

$$I_{avg} = \frac{E_{tot}}{N(\tau + \Delta t)} = I_p D_C \tag{6.1}$$

where D_C, the pulse train duty cycle, is defined as

$$D_C = \tau/(\tau + \Delta t) \tag{6.2}$$

Which of these timescales dominates the optical damage processes therefore depends on which of these intensities first exceeds the corresponding damage threshold. Since $D_C \leq 1$ and $\tau_{tot} \geq \tau$, the result is that optical damage is always dominated by the single pulse timescale. In other words, a single pulse always has higher intensity than a time-averaged sequence of identical pulses, so if a given pulse is below the damage threshold a train of such pulses should be safe as well. Under the assumption that successive pulses do not interact, the maximum laser energy is therefore only limited by the energy stored in the laser amplifiers and the number of pulses that fit in the time during which the laser amplifier is active. For the 200 J laser (Raptor) described here, this may allow up to 1 kJ of energy to be directed over a maximum pulse train length of ~ 10 μs.

It is unfortunately likely that the effect of multiple pulses in rapid succession on the optical damage threshold are not negligible, because the optical system may neither return to its initial conditions nor reach a steady state in between pulses. For example, the optical coatings may retain heat longer than the separation between pulses. This subject has not been well-explored in the literature, especially in the laser and pulse shape regime discussed here. Determining how the optical damage threshold behaves for such pulse shapes is therefore an interesting question in its own right, in addition to being centrally important to evaluating the technical feasibility of the pulse train concept.

6.1.1 Monte-Carlo Pulse Train Calculations

The Monte-Carlo model described in Sec. 4.5 can be used to illustrate the benefits of pulse trains. Like the single pulse calculations presented previously, pulse trains are modeled under the assumption that all laser-produced ions are produced instantaneously ($\tau \to \delta(t)$) by each

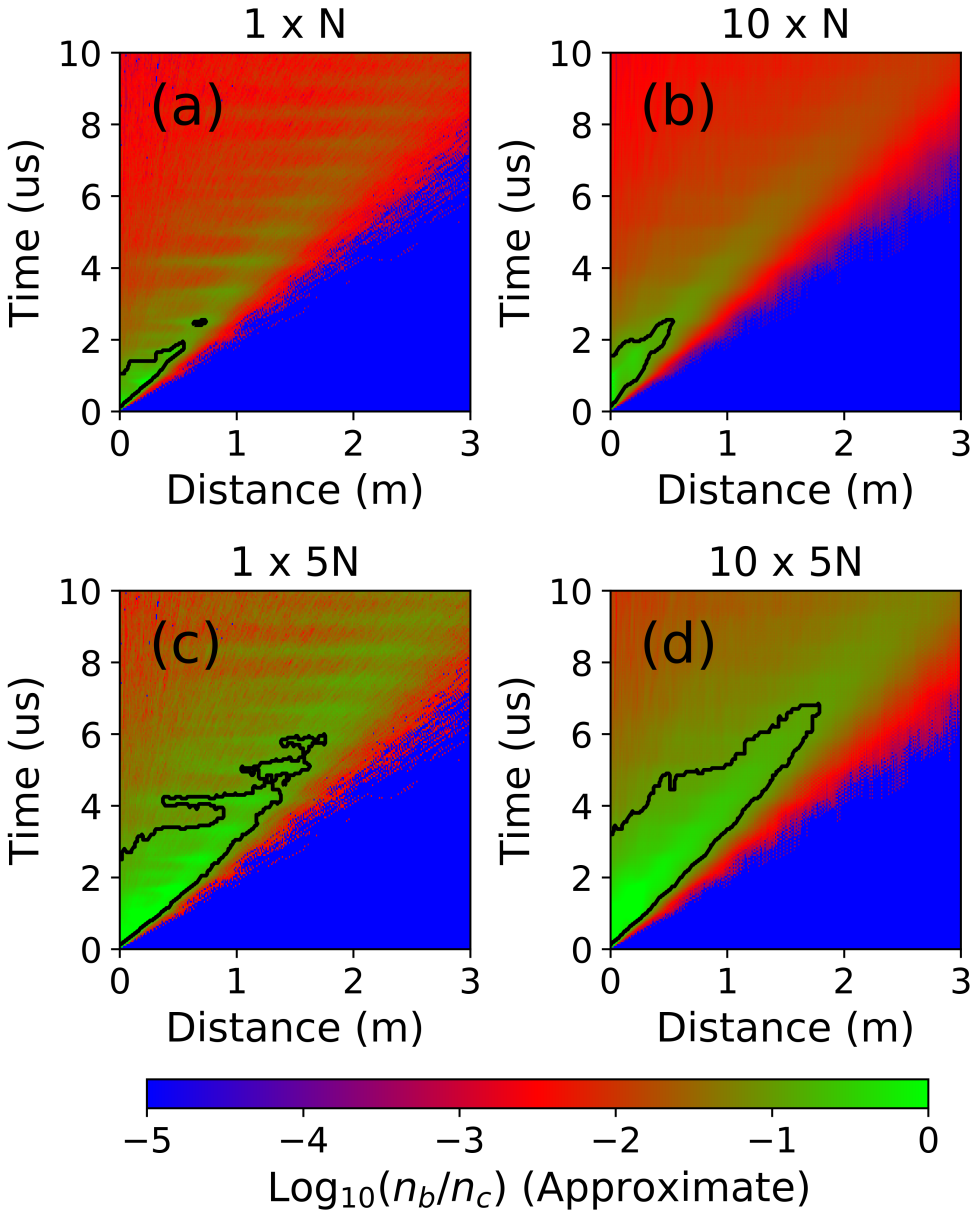

Figure 6.2: Calculated axial density distributions ($x = y = 0$) displayed as a function of distance from the laser target and time with a contour (black) marking the edge of the instability growth region where $n_b/n_c \geq 10\%$. Six cases are shown: a) N_p particles in a single pulse b) N_p particles distributed between ten pulses each separated by 100 ns c) $5N_p$ particles in a single pulse d) $5N_p$ particles in ten pulses separated by 100 ns. Adding multiple pulses slightly increases the extent of the high density region, but increasing the number of particles has a much larger effect.

laser pulse, and that the density distributions created by separate pulses add linearly. If the axial density distribution created by a single pulse is $n(z,t)$, then the density created by a train of N pulses with separation Δt is then

$$n_{pulses}(z,t) = \sum_{i=0}^{N-1} n(z, t + i\Delta t) \tag{6.3}$$

Figure 6.2a shows the same calculation discussed in Sec. 4.5 corresponding to a single pulse of N_p particles equivalent to a shot with the current 200 J laser. A black contour marking $n_b/n_c \sim 10$ % bounds the region in which the RHI growth rate is non-negligible. This region extends to ~ 50 cm, consistent with the results of Sec. 5.4.1. Figure 6.2b shows the same number of particles divided into ten pulses with a pulse separation of 100 ns. In this case the resulting RHI growth region extends slightly farther in space, and is also more uniform as the series of pulses smooths out spikes caused by ions gyrating back onto the axis. Figure 6.2c shows a single pulse with $5N_p$ particles, corresponding to approximately five times the incident laser energy. This creates a much larger initial density and therefore a much larger region where the density is above the RHI growth threshold. Finally, Figure 6.2d shows ten laser pulses with $\Delta t = 100$ ns and $5N_p$ particles. This creates the the largest and most uniform RHI growth region.

These calculations demonstrate that a series of sufficiently closely-spaced pulses will merge to produce a long, relatively homogeneous extended LPP ideal for beam instability growth. The Monte-Carlo model can also be used to estimate the ideal pulse separation. Calculations for several values of Δt, each with ten pulses and $5N_p$ particles, are shown in Fig. 6.3. Too long of a pulse separation (Fig. 6.3d) results in separate LPPs that do not merge together, while too short of a separation (Fig. 6.3a) is indistinguishable from a single pulse (compare to Fig. 6.2c). Between these extremes, choosing a pulse separation requires prioritizing extent of the LPP in either time (Fig. 6.3c) or space (Fig. 6.3b). Future experiments and/or simulations are necessary to determine which of these contributes more

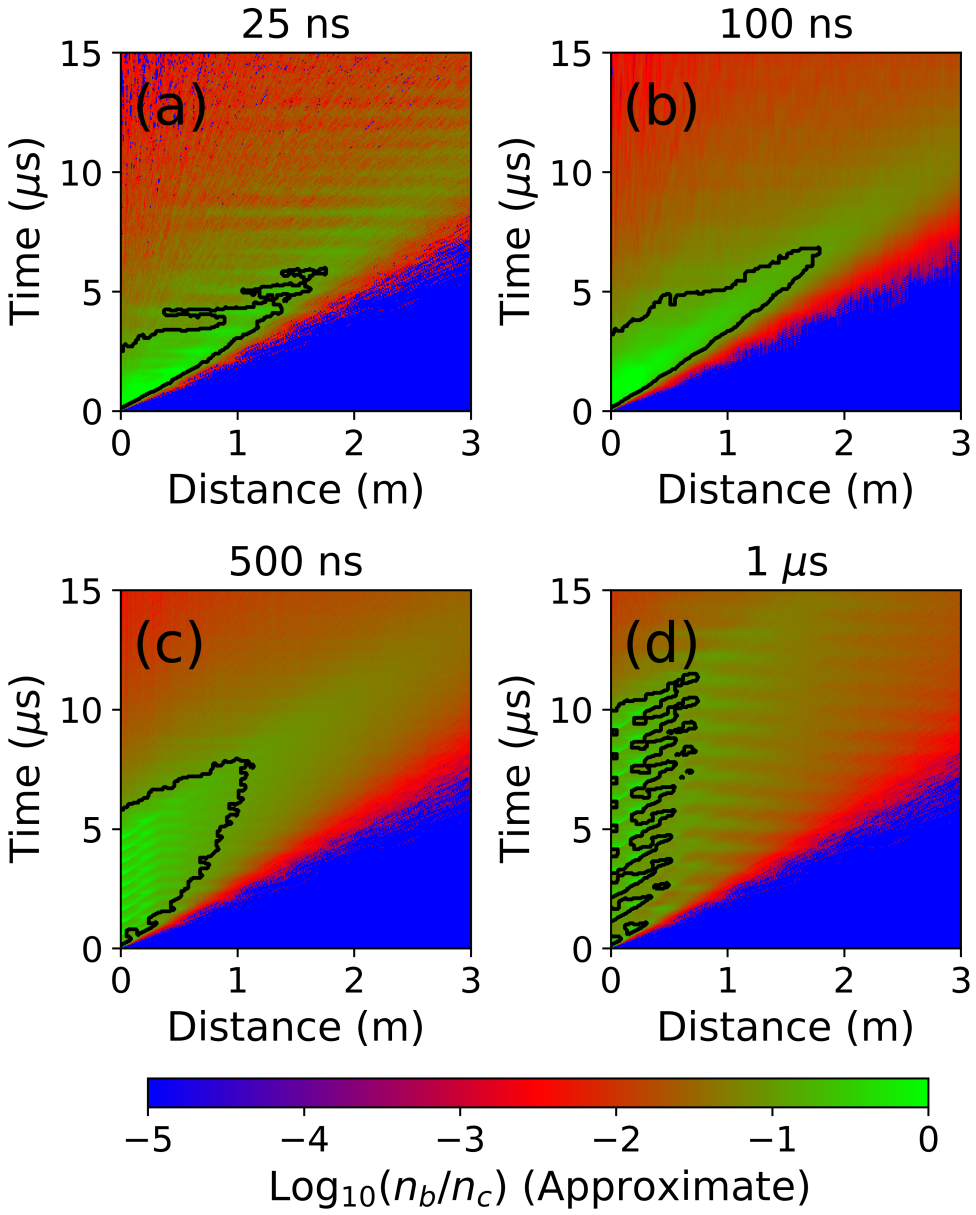

Figure 6.3: Predicted LPP axial density distributions are displayed for pulse trains of ten pulses and $5N_p$ particles (identical to Fig. 6.2d) for various pulse separations. A given laser driver has an ideal pulse separation that depends on its velocity distribution. Pulse separations that are too short are similar to a single pulse (a), while pulses that are too long do not merge together (d). In between, the pulse length can be optimized to extend the RHI growth region in space (b) or in time (c).

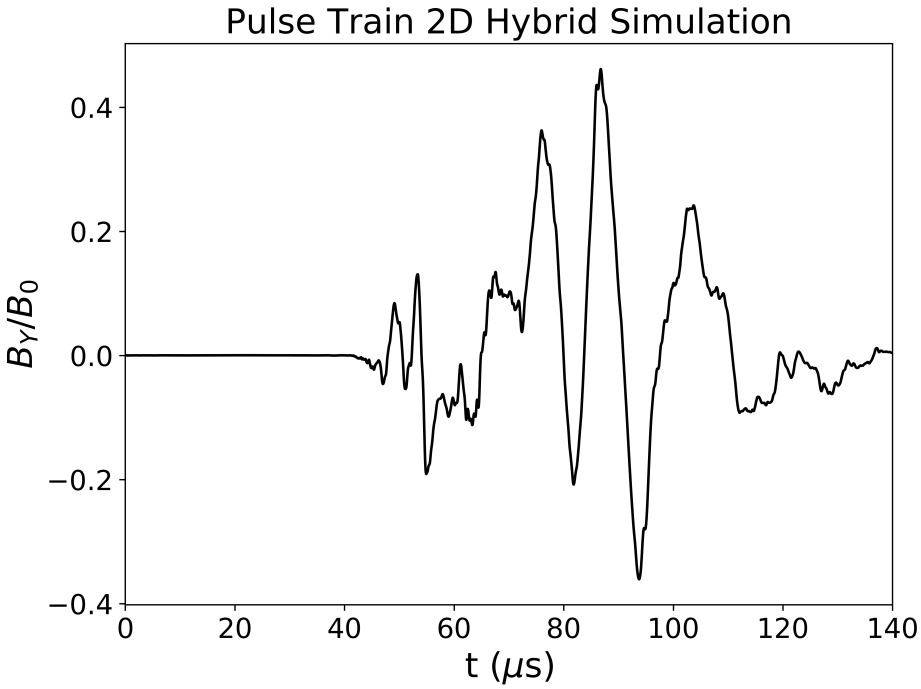

Figure 6.4: A virtual magnetic flux probe time trace from a 2D hybrid simulation of an experiment driven by ten laser pulses (each identical to a single pulse of the 200 J laser in the current experiments) and with $\delta t = 140$ ns. The probe is located approximately 7.5 m from the laser target and 7 cm off-axis. This simulation also includes a Gaussian background plasma distribution that reproduces the radial density variation in the LAPD. The result shows waves of substantially higher amplitude approaching $dB/B_0 \sim 0.5$. Simulation results provided by Martin Weidl.

to the growth of beam instabilities.

6.1.2 2D Hybrid Pulse Train Simulation

The Monte-Carlo calculations discussed in Sec. 6.1.1 show how the pulse trains affect the LPP density distribution, but they cannot demonstrate that these changes to the density distribution result in the development of larger-amplitude waves. For this purpose, a single simulation was run using the 2D hybrid code that has previously been validated using experimental measurements (Sec. 5.6). This simulation included ten pulses identical to the 200 J experiment simulation discussed previously (each separated by $\Delta t = 140$ ns) corresponding

to a total laser energy of $\sim$ 2 kJ. This simulation also included a Gaussian background plasma distribution to model the LAPD's radial density gradient. The simulation domain is $192\delta_{ci} \times 7\delta_{ci}$ with a grid resolution of $\Delta x = \delta_{ci}/8$ and a temporal resolution of $dt = 10^{-4}\omega_{cc}^{-1}$. Results are normalized to the background magnetic field of 300 G.

Results from a virtual magnetic flux probe in the simulation show much larger waves than in the 200 J single pulse simulation, with amplitudes as high as $dB/B_0 \sim 0.5$. A polarization decomposition of these signals shows that while some parts of the signal are right-hand circularly polarized, others are dominantly left-hand circularly polarized. This observation is consistent with growth of the NRI. These results suggest that the larger instability growth region and higher beam density predicted by the Monte-Carlo model do in fact lead to higher wave amplitudes.

6.2 Collimated Laser-Produced Plasmas

Previous experimental results have shown that the distribution of the LPP velocity as a function of polar angle is approximately $v(\theta) \propto \cos^2(\theta)$ [104, 61]. These measurements were made using a flat target (or a round target effectively flat on the scale of the laser spot). Modifying this distribution to create a more collimated LPP (closer to $v(\theta) \propto \delta(\theta)$) would direct more of the particle energy into field-parallel velocity, increasing its effectiveness as a quasi-parallel shock driver. Shaped targets are a possible approach to achieving this experimentally.

A more collimated LPP may have a velocity distribution like $v(\theta) \propto \cos^n(\theta)$ where $n > 2$. To explore the possible benefit of this type of driver, several Monte-Carlo calculations were run with different values of n ranging from 2 to 12. The results of these calculations, several of which are plotted in Figure 6.5, show a marginal improvement in the RHI growth region (black contours) when $n = 4$, but little further improvement is found for $n > 4$. As the LPP becomes more collimated, its divergence eventually becomes negligible compared to cross-

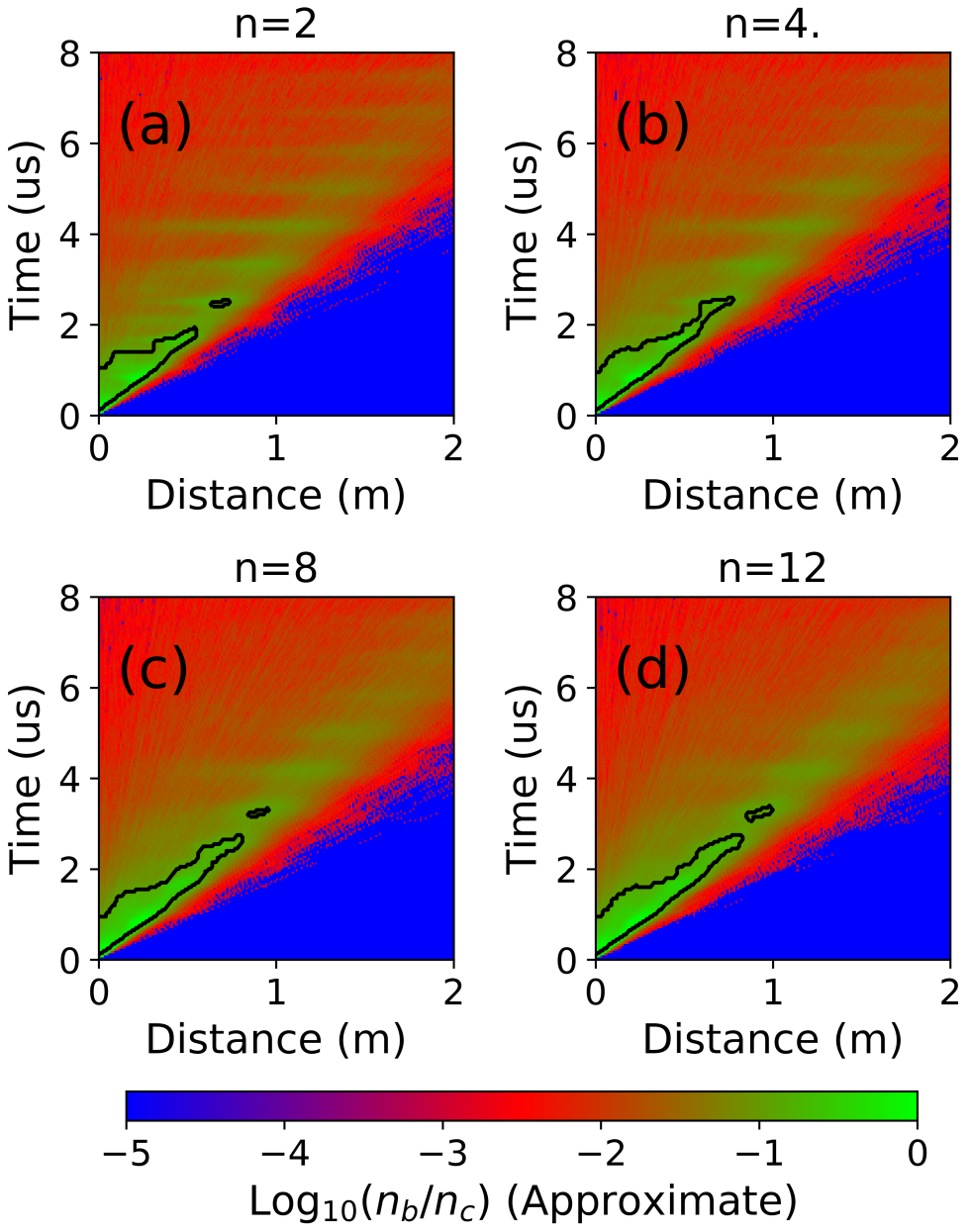

Figure 6.5: Monte-Carlo calculations for different values of n show that collimating the LPP somewhat extends the RHI growth region, but that diminishing returns set in after $n \sim 4$ as other diffusion and dispersion effects become dominant. The velocity distribution of the LPP as a function of polar angle is assumed to vary as $v(\theta) \propto \cos^n(\theta)$.

field diffusion and parallel velocity dispersion. This result suggests that shaped targets may provide a small benefit to performance, but that they are less effective than pulse trains.

6.3 Reducing Cross-Field Diffusion

Comparisons of Monte-Carlo calculation outputs to Langmuir probe ion saturation current measurements in Sec. 4.5 show that a substantial cross-field diffusion coefficient is necessary to correctly model the evolution of the LPP density distribution. The value of this coefficient was found empirically to be $D \sim 5000$ m^2/s, which is approximately consistent with the primary diffusion process being Coulomb collisions between the beam ions and core plasma electrons. This process is responsible for approximately half the measured decrease in LPP density throughout the experiment (the other half being due to field-parallel velocity dispersion).

Reducing the diffusion coefficient could therefore substantially extend the region of dense LPP where beam instabilities can grow. Figures 6.6a and 6.6b show the predicted density evolution for a single pulse of N_p particles and ten pulses with a total of $5N_p$ particles each separated by 100 ns. These calculations are identical to those presented in Fig. 6.1.1, and include cross-field diffusion modeled as a random walk with $D \sim 5000$ m^2/s. Fig. 6.6c and 6.6d present corresponding calculations which are identical except for a lower diffusion coefficient of $D \sim 200$ m^2/s. Both low-diffusion cases include an extended RHI growth region, but the improvement in the pulse train case shown in Fig. 6.6d is particularly striking.

Since beam ion/core electron Coulomb collisions seem to be primarily responsible for the cross-field diffusion, it may be possible to decrease the diffusion coefficient experimentally by heating the LAPD electrons prior to the laser shot, possibly through electron cyclotron heating. Calculations presented in Sec. 4.4.4 show how the diffusion coefficient depends on the electron temperature. These calculations suggest that increasing the LAPD electron temperature from 5 eV to ~ 25 eV would be sufficient to decrease the cross-field transport

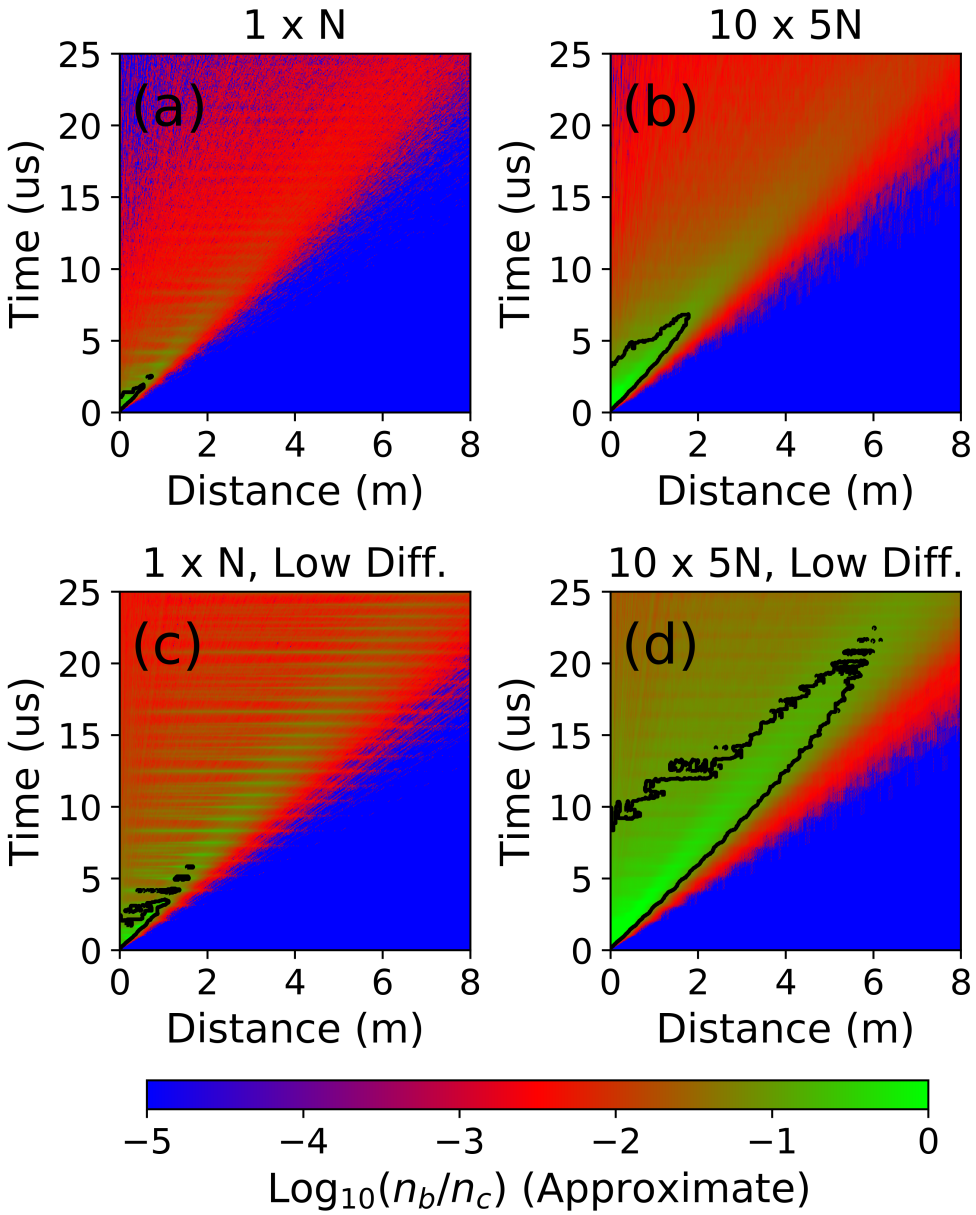

Figure 6.6: A cross-field diffusion coefficient of $D \sim 5000$ m^2/s is found to be necessary to reproduce experimental results. Predicted LPP density distributions including this diffusion are shown for the current 200 J experiment (a) and a train of ten pulses (b). Reducing this diffusion coefficient to $D \sim 200$ m^2/s substantially increases the RHI growth region in both cases (c,d). Decreased cross-field diffusion also leads to more pronounced "gyro-spikes" in the density as the LPP gyrate back onto the axis every gyroperiod.

to the value of $D \sim 200$ m^2/s assumed in Fig. 6.6c,d. The results of the Monte-Carlo calculation suggest that this approach may be worth exploring, particularly in conjunction with the pulse train concept.

6.4 Possible Future Experimental Topics

The scientific goals attainable by future experiments will depend on the success of the technical methods discussed above in creating larger-amplitude waves, reaching parameter regimes to excite new beam instabilities like the NRI, and ultimately driving an actual quasi-parallel shock. Some experiments are already possible, such as further spatially resolved measurements of the linear RHI waves already produced (Sec. 6.4.1). If larger-amplitude waves can be produced, experiments could be conducted on wave/particle scattering (Sec. 6.4.2) and nonlinear wave/wave interactions (Sec. 6.4.3). The creation of a fully-formed quasi-parallel collisionless shock would allow countless experiments on particle acceleration, shock reformation, and many other subjects, but speculation on these topics is left for future work.

6.4.1 Improved Spatially Resolved Measurements

Further experiments at low (linear) wave amplitudes could continue to take advantage of high-repetition rate measurements to study the spatial structure of the waves. Possible experimental directions include the following

- Combine measurements of multiple transverse planes of magnetic field measurements to follow the observed filamentary current structures [63] in 3D and study how they merge together as the wave frequencies decrease.
- Directly observe the wave reflection/refraction process hypothesized in Chapter 5 that allows oblique waves to be observed far away from the laser target. These measurements may be directly relevant to observations of whistler wave ducting in the magne-

tosphere [115, 116, 146]. Refraction of ULF waves in the quasi-parallel foreshock may also be an important process that could be investigated [57].

- Apply spatially-resolved measurements of LPP velocity within the instability growth region to conclusively demonstrate that the LPP is providing the free energy to drive the beam instability. The number of fast LPP ions should decrease throughout the growth region, then remain constant.

6.4.2 Wave-Particle Scattering

An important consequence of the growth of electromagnetic beam instabilities is pitch angle scattering of ions by the associated electromagnetic waves. This process can thermalize incoming particles, as observed in the foreshock where growth of the RHI and associated ULF waves produce a diffuse ion distribution. Reproducing this scattering process in the laboratory would allow an experimental measurement of the effective diffusion coefficient due to wave/particle interactions that could then be compared to spacecraft measurements and simulations. In order to determine the wave amplitudes necessary to observe this process over experimentally feasible length scales, it is helpful to examine a theoretical model for particle pitch-angle scattering through an arbitrary spectrum of waves.

The cumulative pitch-angle scattering of particles passing through a region of electromagnetic turbulence can be modeled as a stochastic diffusion process [75]. For a particle with pitch angle α, with velocity $v^2 = v_\perp^2 + v_\parallel^2$ defined as

$$\tan(\alpha) = -v_\perp / v_\parallel \tag{6.4}$$

the pitch-angle diffusion coefficient can be approximated by [75]

$$D \approx \omega_{c,0}^2 \frac{\delta B^2 / \Delta k}{B_0^2} \frac{1}{v|\cos(\alpha)|} \tag{6.5}$$

where $\omega_{c,0}$ is the background ion cyclotron frequency in a background magnetic field B_0, δB is the wave amplitude, and Δk is the difference between the wavenumber of the wave k and the wavenumber for which the particle would be resonant with the wave in accordance with Eq. 2.2 for $m = 1$. In the limit where the particle is close to resonance, $\Delta k \to 0$, we can write $\delta B^2/\Delta k \to \mu_0 u_B(k)$ where $u_B(k)$ is the wave's spectral energy density per unit volume defined such that

$$u_{tot} = \int u_B(k) dk \tag{6.6}$$

If the wave spectrum can be approximated as a delta function, $u_B = \delta(k)$, then it follows that δB is the wave amplitude at that wave number and

$$u_{tot} = \frac{\delta B^2}{\mu_0} = u_B(k) k \tag{6.7}$$

And so the diffusion coefficient can be approximated as

$$D \approx \frac{4\pi^2 q^2}{m^2} \frac{\delta B^2}{kv|\cos(\alpha)|} \tag{6.8}$$

The pitch-angle diffusion coefficient has has units of radians per second, so the characteristic time scale over which a large-angle ($\sim \pi$) deflection will likely occur can be approximated as $\tau = 1/D$. The corresponding effective mean path is

$$\lambda = v\tau = \frac{m^2}{4\pi^2 q^2} \frac{kv^2|\cos(\alpha)|}{\delta B^2} \tag{6.9}$$

This equation can be used to estimate the wave amplitude that the experiment must achieve in order to observe substantial pitch-angle scattering. For example, waves with a wavelength of $\lambda = 1$ m would require an amplitude of $\delta B \approx 50$ G to substantially scatter a beam of C^{+4} ions moving at $v = 350$ km/s over a length of ~ 1 m.

6.4.3 Nonlinear Wave Experiments

Many of the interesting and poorly understood aspects of quasi-parallel shock formation and structure relate to nonlinear wave evolution and wave/wave interactions. What plasma quantities must become nonlinear to enter this regime is itself at question, as $dB/B_0 \sim 1$ is not necessarily required to observe nonlinear dynamics [148]. This question could be addressed experimentally by determining what parameters are required in order to violate the predictions of linear theory. Experiments could observe the steepening of waves generated by beam instabilities [3] to produce shocklets [108, 76, 140] or SLAMs [31] leading to the radiation of whistler precursors [142]. Ion trapping in large-amplitude waves forms density compressions [57], while nonlinear wave/wave interactions may also play a role in the formation of density structures such as hot flow anomalies [96] and foreshock bubbles [127]. The production of nonlinear beam instability waves in the laboratory would allow experiments on all of these topics.

CHAPTER 7

Conclusions

Generating a quasi-parallel collisionless shock in a repeatable and well-diagnosed laboratory environment would complement spacecraft measurements and improve our understanding of their formation and structure. A recent experimental campaign has been conducted at UCLA to investigate the potential of laser-produced plasmas (LPPs) as drivers of such experiments. These experiments combined one of two high-energy lasers with the magnetized background plasma of the Large Plasma Device (LAPD) to drive the electromagnetic ion/ion beam instabilities responsible for shock formation. The results are consistent with the very early stages of quasi-parallel shock formation, but the process is terminated by the dispersal of the LPP below the required density threshold for beam instability growth. Along with comparison to theory and simulations, these results can now inform the design of future laboratory quasi-parallel shock experiments.

The key conclusions of this work are as follows:

- Quasi-parallel shock formation requires the excitation of several electromagnetic ion/ion beam instabilities including the right-hand resonant instability (RHI) and the non-resonant instability (NRI). Exciting these instabilities requires a core plasma and a highly super-Alfvénic and uniform beam plasma with a density of at least 5-10% of that of the core plasma. Both beam instabilities grow slowly, so a fully-formed quasi-parallel collisionless shock requires a length of ~ 500 ion-inertial lengths to develop.

- LPPs are capable of achieving the beam velocities required for shock formation but have an inherently non-uniform density distribution. Velocity dispersion and cross-field

diffusion cause the LPP to expand, decreasing its density. In the experiments described here, cross-field diffusion is primarily caused by beam ion/core electron collisions.

- A Monte-Carlo calculation employing a free-streaming model of particle motion (including only cyclotron gyration and random walk cross-field diffusion) and initialized with parameters based on experiments provides a reasonable approximation of the LPP density evolution.

- Right-hand circularly polarized electromagnetic waves are observed in the experiment at frequencies consistent with excitation of the RHI. Waves at several separate frequencies are observed, corresponding to different carbon charge states present in the LPP.

- The frequencies, wavelengths, and group velocities (measured by their arrival time at a distant probe) of the measured waves are consistent with their theoretical linear dispersion relation at high frequencies, while a discrepancy at lower frequencies is consistent with those waves propagating obliquely. The observation of oblique waves far from the laser target would imply geometrically that the waves are not propagating straight from their growth region near the target. The waves may be reflecting or refracting through radial density gradients at the edges of the LAPD background plasma, but this process has not been directly observed.

- The amplitude of the observed waves is low ($dB/B_0 \sim 0.01$), and the waves are therefore well described by linear theory. Much higher amplitude nonlinear waves ($dB/B_0 \sim 1$) are required for shock formation, and are commonly observed by spacecraft. The wave amplitudes in the experiment are low because wave growth is limited to a small region near the target (~ 20 cm). Outside of this region, the density of the LPP is insufficient to excite the RHI.

- High repetition rate experiments reveal that the spatial structure of the observed waves

changes in different frequency regimes. At high frequencies, a number of current filaments are observed rotating in the transverse plane with the same sense as the electron gyromotion. At lower frequencies these filaments coalesce to form an axial cavity mode. Interactions between the waves and radial density gradients at the edges of the core plasma are likely involved in this process.

- Comparisons of experimental measurements with simulations and spacecraft measurements supports the conclusion that the waves observed in the experiment are created by the same mechanism as ultra-low frequency (ULF) waves observed upstream of the Earth's quasi-parallel bow shock. The use of heavier ion species in the experiment (carbon and helium) compared to the terrestrial foreshock (primarily protons) means that the dimensionless frequencies of the waves are not directly comparable, but mutual comparison of both experimental and spacecraft measurements to corresponding simulations confirms that waves in both cases are consistent with the RHI.

- Future experiments could employ sequences of laser pulses to increase the high-density region of the LPP suitable to beam instability growth. Simulations suggest this technique could lead to substantial increases in wave amplitude. Heating background electrons could also increase LPP density by reducing cross-field transport due to beam ion/core electron collisions.

In summary, LPPs are promising drivers of laboratory quasi-parallel collisionless shocks. Current experiments are capable of creating conditions relevant to quasi-parallel foreshocks, including the generation of waves analogous to the ULF waves observed upstream of planetary bow shocks. However, decreasing LPP density due to velocity dispersion and cross-field transport terminates the growth of electromagnetic beam instabilities long before a fully-formed shock can develop. Future experiments will require technical innovations such as laser pulse trains or reduced LPP cross-field transport in order to achieve a fully-formed quasi-parallel collisionless shock.

APPENDIX A

Field-Parallel Diamagnetic Cavity Formation

A diamagnetic cavity is formed when a magnetized plasma expands rapidly within a pre-magnetized background plasma. Charge separation at the edge of the expanding plasma creates an ambipolar electric field which drives an azimuthal $\vec{E} \times \vec{B}_0$ drift. At the same time, gradients in the electron pressure drive a $\nabla P \times \vec{B}_0$ current. Since $\vec{E}$ and ∇P in this configuration are approximately parallel, these currents add together to expel the ambient magnetic field.

Diamagnetic cavities have been observed in heavy-ion release experiments [143] and high-altitude nuclear explosions [32]. Hot diamagnetic cavities (HDCs) are also observed upstream of the terrestrial bow shock, where they are theorized to be caused by strong bursts of reflected ions [120]. Diamagnetic cavities can be produced experimentally using laser-produced plasmas (LPPs) [25, 143]. The structure of $\vec{E}$ and ∇P in a LPP plume is typically axisymmetric: isobars can be approximated as ellipsoids [6, 104] with typical aspect ratios of 1.5-3 [104]. The major axis of the ellipsoid is aligned with the LPP bulk velocity, which itself is parallel to the target surface normal. The result is that the shape of the diamagnetic cavity depends strongly on the orientation of the LPP bulk velocity relative to the ambient magnetic field. This concept is illustrated in Fig. A.1 and Fig. A.2, which show the $\nabla P \times \vec{B}_0$ currents calculated using the ellipsoidal isobar approximation (aspect ratio ~ 2) for both field-perpendicular and field-parallel orientations of the LPP. In both cases, the resulting bubble is spatially extended in the direction of the ambient magnetic field and more confined across the ambient magnetic field.

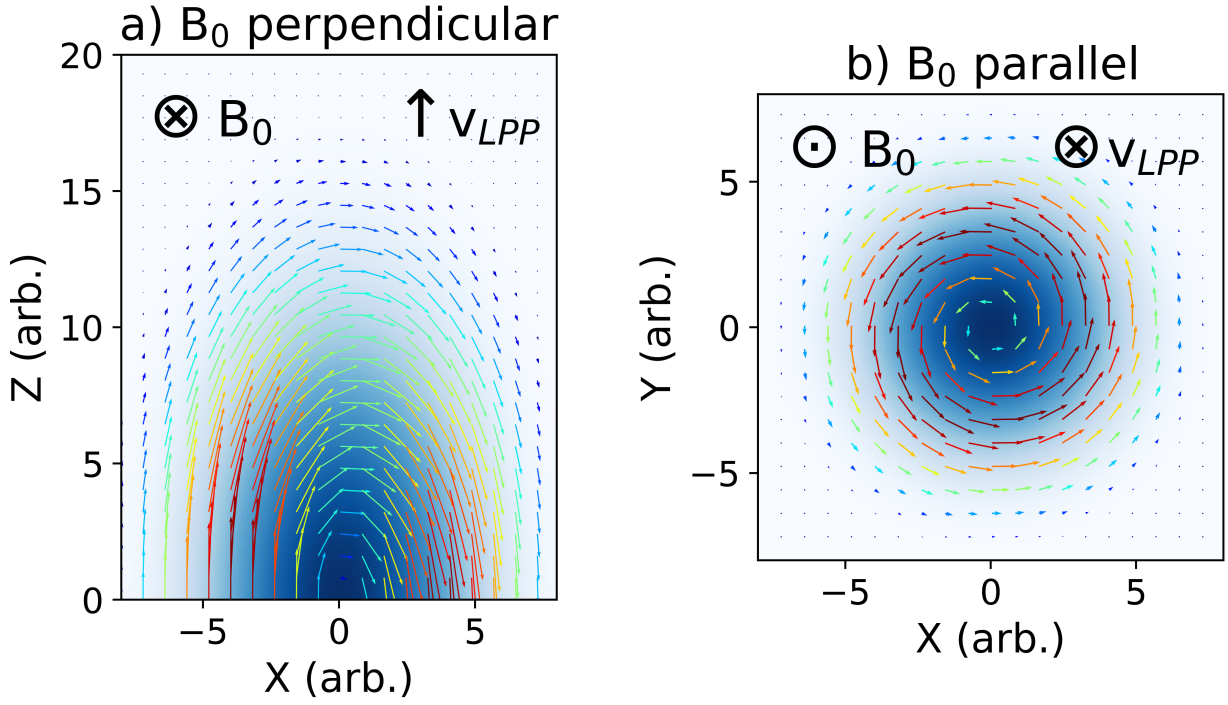

Figure A.1: A model of the $\nabla P \times \vec{B}_0$ currents that form a diamagnetic cavity in both the parallel and perpendicular cases. Vectors represent the diamagnetic current (colored by their magnitude) while the blue shading shows the assumed electron pressure modeled as ellipsoidal isobaric contours [6, 104].

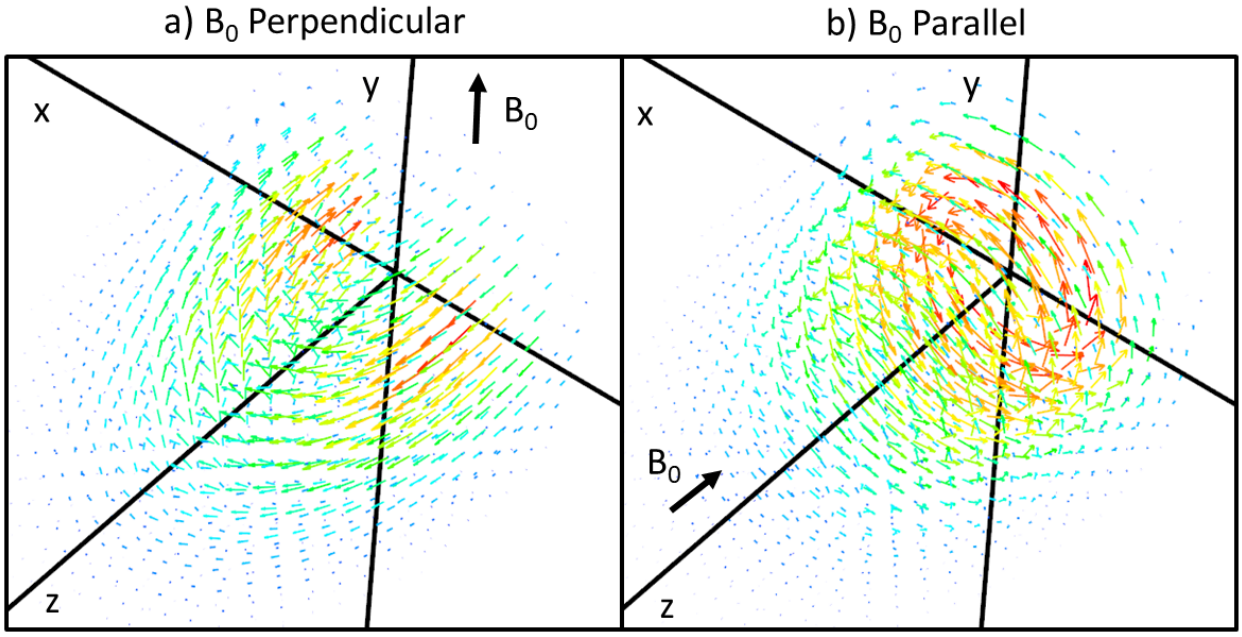

Figure A.2: A 3D vector plot of the diamagnetic current structures shown in Fig. A.1.

Numerous previous experiments have investigated the formation of diamagnetic cavities in which the LPP bulk velocity is perpendicular to the ambient magnetic field [149, 130, 25, 26, 91]. High repetition-rate lasers have recently begun to enable the volumetric mapping of electrostatic and magnetic fields in these experiments [14, 107]. Common shared features of these measurements include finger-like "flute mode" instabilities at the edges of the bubble [69, 100] and anomalously fast diffusion of the ambient field back into the cavity as it collapses.

A recent series of measurements has been made employing the high-repetition rate 15 J laser described in Chapter 3 to make volumetric magnetic field measurements of a diamagnetic cavity generated by a LPP with a field-parallel bulk velocity. The resulting cavity is elongated along the field, occupying a larger total volume than in the field-perpendicular case and subsequently expelling less of the ambient magnetic field (Fig. A.3). Near the axis, a partially evacuated ($\Delta B \sim 10\%\ B_0$) "foot" extends far down the field. Field compressions are observed on either side of the cavity in the region where the cavity expansion is

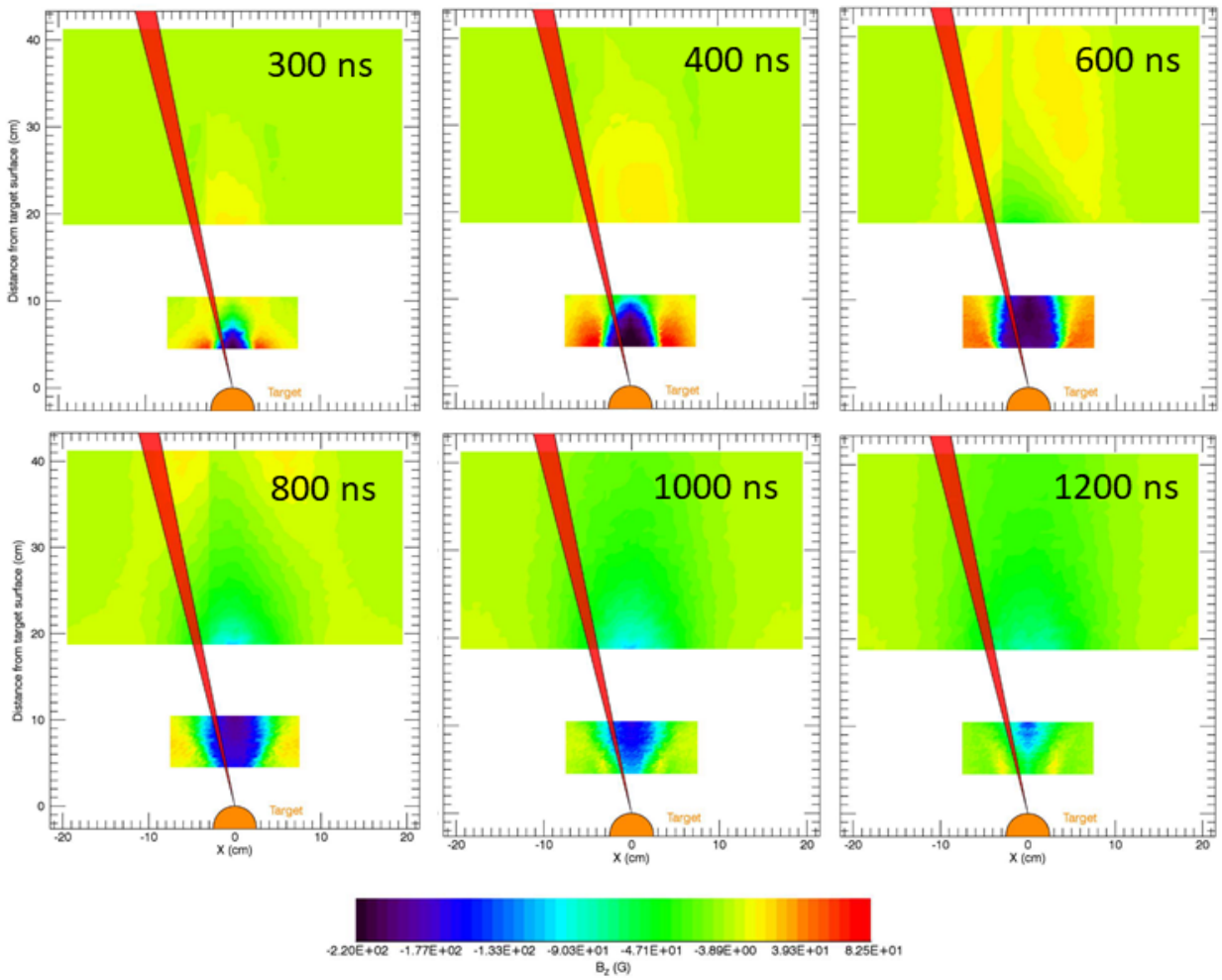

Figure A.3: XZ planes (at $y = 0$) of magnetic field measurements at six different times during the expansion and collapse of a diamagnetic cavity produced by a field-parallel LPP. The region $x < 0$ in the smaller plane and $x < -5$ in the larger plane were physically inaccessible because of the laser path, so data in those regions is mirrored from $x > 0$ assuming cylindrical symmetry.

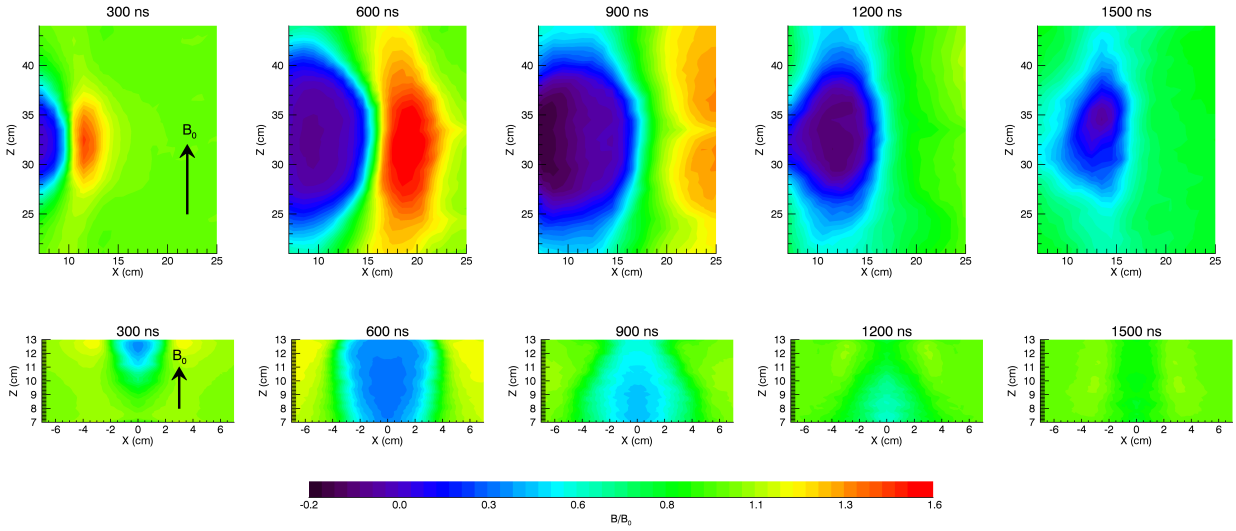

Figure A.4: A comparison of XZ plane measurements of magnetic field in the field-parallel and field-perpendicular LPP cases. The shape of both cavities is similar relative to the direction of the ambient field. The perpendicular cavity was created by a higher laser energy (20 J) than the parallel cavity (15 J), partially accounting for the more complete evacuation of the magnetic field in the perpendicular case.

more similar to the field-perpendicular case. A comparison with the field-perpendicular case (Fig. A.4) shows that the bubble is similarly shaped relative to the ambient field, and that in both cases the bubble collapses fastest perpendicular to the field as the ambient field diffuses back in.

Fast-gated ion fluorescence images [61] of the field-parallel diamagnetic cavity show field-parallel striations that may correspond to the flute modes observed in previous experiments (Fig. A.5a). The spatial frequency of the striations is approximately 1 cm^{-1} (Fig. A.5b) assuming the striations are close to the $x = 0$ plane. The spatial location of the striations changes from shot-to-shot, consistent with randomly seeded instability growth. Flute modes observed in previous experiments were consistent with the large Larmor radius limit of the Rayleigh-Taylor Instability (RTI), which has been theoretically investigated for the case of a plasma expanding across the field [69]. It is an open question whether the field-parallel striations observed in the current experiments are also generated by the RTI and, if so, how

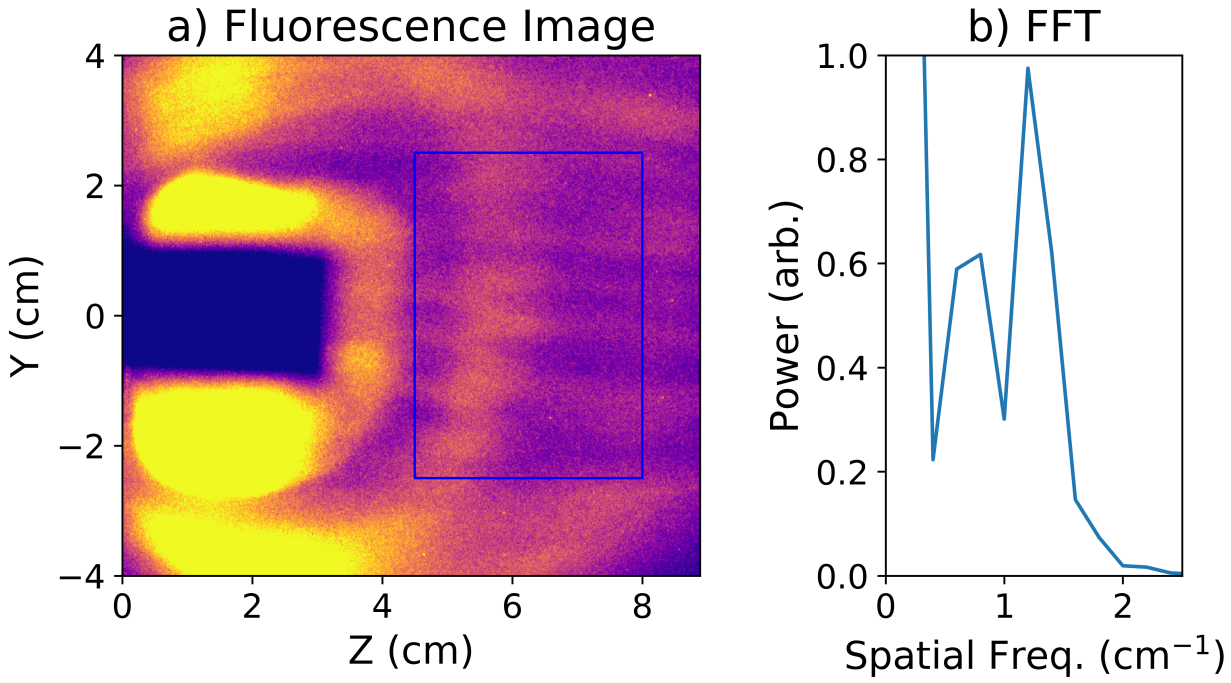

Figure A.5: Imaging of plasma fluorescence with a fast-gated camera (a, false color) shows flute mode structures in the field-parallel diamagnetic cavity at $t \sim 1.1$ μs. The brightest part of the LPP has been occluded to avoid saturating the detector. A spatial FFT (b) of a cut through this region (blue box) perpendicular to the flutes and averaged along the flutes estimates their spatial frequency to be approximately 1 cm^{-1}.

the parallel magnetic field affects the evolution of that instability. Future imaging could resolve this question by determining the spatial extent of the striations as a function of time in order to extract an instability growth rate to compare to theory.

REFERENCES

[1] M. Ackermann, M. Ajello, A. Allafort, L. Baldini, J. Ballet, G. Barbiellini, M. G. Baring, D. Bastieri, K. Bechtol, R. Bellazzini, R. D. Blandford, E. D. Bloom, E. Bonamente, A. W. Borgland, E. Bottacini, T. J. Brandt, J. Bregeon, M. Brigida, P. Bruel, R. Buehler, G. Busetto, S. Buson, G. A. Caliandro, R. A. Cameron, P. A. Caraveo, J. M. Casandjian, C. Cecchi, Ö. Çelik, E. Charles, S. Chaty, R. C. G. Chaves, A. Chekhtman, C. C. Cheung, J. Chiang, G. Chiaro, A. N. Cillis, S. Ciprini, R. Claus, J. Cohen-Tanugi, L. R. Cominsky, J. Conrad, S. Corbel, S. Cutini, F. D'Ammando, A. de Angelis, F. de Palma, C. D. Dermer, E. do Couto e Silva, P. S. Drell, A. Drlica-Wagner, L. Falletti, C. Favuzzi, E. C. Ferrara, A. Franckowiak, Y. Fukazawa, S. Funk, P. Fusco, F. Gargano, S. Germani, N. Giglietto, P. Giommi, F. Giordano, M. Giroletti, T. Glanzman, G. Godfrey, I. A. Grenier, M.-H. Grondin, J. E. Grove, S. Guiriec, D. Hadasch, Y. Hanabata, A. K. Harding, M. Hayashida, K. Hayashi, E. Hays, J. W. Hewitt, A. B. Hill, R. E. Hughes, M. S. Jackson, T. Jogler, G. Jóhannesson, A. S. Johnson, T. Kamae, J. Kataoka, J. Katsuta, J. Knödlseder, M. Kuss, J. Lande, S. Larsson, L. Latronico, M. Lemoine-Goumard, F. Longo, F. Loparco, M. N. Lovellette, P. Lubrano, G. M. Madejski, F. Massaro, M. Mayer, M. N. Mazziotta, J. E. McEnery, J. Mehault, P. F. Michelson, R. P. Mignani, W. Mitthumsiri, T. Mizuno, A. A. Moiseev, M. E. Monzani, A. Morselli, I. V. Moskalenko, S. Murgia, T. Nakamori, R. Nemmen, E. Nuss, M. Ohno, T. Ohsugi, N. Omodei, M. Orienti, E. Orlando, J. F. Ormes, D. Paneque, J. S. Perkins, M. Pesce-Rollins, F. Piron, G. Pivato, S. Rainò, R. Rando, M. Razzano, S. Razzaque, A. Reimer, O. Reimer, S. Ritz, C. Romoli, M. Sánchez-Conde, A. Schulz, C. Sgrò, P. E. Simeon, E. J. Siskind, D. A. Smith, G. Spandre, P. Spinelli, F. W. Stecker, A. W. Strong, D. J. Suson, H. Tajima, H. Takahashi, T. Takahashi, T. Tanaka, J. G. Thayer, J. B. Thayer, D. J. Thompson, S. E. Thorsett, L. Tibaldo, O. Tibolla, M. Tinivella, E. Troja, Y. Uchiyama, T. L. Usher, J. Vandenbroucke, V. Vasileiou, G. Vianello, V. Vitale, A. P. Waite, M. Werner, B. L. Winer, K. S. Wood, M. Wood, R. Yamazaki, Z. Yang, and S. Zimmer. Detection of the characteristic pion-decay signature in supernova remnants. *Science*, 339(6121):807–811, 2013.

[2] K. Akimoto, S. P. Gary, and N. Omidi. Electron/ion whistler instabilities and magnetic noise bursts. *Journal of Geophysical Research: Space Physics (1978–2012)*, 92(A10):11209–11214, 10 1987.

[3] K. Akimoto, D. Winske, T. G. Onsager, M. F. Thomsen, and S. P. Gary. Steepening of parallel propagating hydromagnetic waves into magnetic pulsations: A simulation study. *Journal of Geophysical Research: Space Physics (1978–2012)*, 96(A10):17599–17607, 10 1991.

[4] V. Angelopoulos, U. Auster, K. H. Glassmeier, and W. Baumjohann. THE L2 FGM. CDAWeb.

[5] V. Angelopoulos, C. W. Carlson, and J. McFadden. THE L2 MOM. CDAWeb.

[6] S. I. Anisimov, D. Bäuerle, and B. S. Luk'yanchuk. Gas dynamics and film profiles in pulsed-laser deposition of materials. *Physical Review B*, 48(16):12076–12081, oct 1993.

[7] M. G. Baring. Diffusive shock acceleration: the Fermi mechanism.

[8] A. R. Bell. The acceleration of cosmic rays in shock fronts - i. *Monthly Notices of the Royal Astronomical Society*, 182(2):147–156, feb 1978.

[9] A. R. Bell. Turbulent amplification of magnetic field and diffusive shock acceleration of cosmic rays. *Monthly Notices of the Royal Astronomical Society*, 353(2):550, 2004.

[10] E. Belova, N. Gorelenkov, E. Fredrickson, K. Tritz, and N. Crocker. Coupling of neutral-beam-driven compressional Alfvén eigenmodes to kinetic Alfvén waves in NSTX tokamak and energy channeling. *Physical Review Letters*, 115(1), jun 2015.

[11] A. G. Berezutsky, V. N. Tishchenko, Y. P. Zakharov, I. B. Miroshnichenko, and I. F. Shaikhislamov. Generation of torsional Alfvén and slow magnetosonic waves by periodic bunches of laser plasma in a magnetised background. *Quantum Electronics*, 49(2):178–180, feb 2019.

[12] R. Blandford and D. Eichler. Particle acceleration at astrophysical shocks: A theory of cosmic ray origin. *Physics Reports*, 154(1):1 – 75, 1987.

[13] R. D. Blandford and J. P. Ostriker. Particle acceleration by astrophysical shocks. *The Astrophysical Journal*, 221:L29–L32, 1978.

[14] J. Bonde, S. Vincena, and W. Gekelman. Electrostatic structure of a magnetized laser-produced plasma. *Phys. Rev. E*, 92:051102, Nov 2015.

[15] C. Bonifazi and G. Moreno. Reflected and diffuse ions backstreaming from the Earth's bow shock 2. origin. *Journal of Geophysical Research: Space Physics*, 86(A6):4405–4413, jun 1981.

[16] D. Burgess. Cyclic behavior at quasi-parallel collisionless shocks. *Geophysical Research Letters*, 16(5):345–348, 5 1989.

[17] D. Burgess. Foreshock-shock interaction at collisionless quasi-parallel shocks. *Advanced Space Research*, 15(8/9):159–169, jan 1995.

[18] D. Burgess, E. Möbius, and M. Scholer. Ion acceleration at the Earth's bow shock. *Space Science Reviews*, 173(1-4):5–47, jun 2012.

[19] D. Burgess and M. Scholer. Microphysics of quasi-parallel shocks in collisionless plasmas. In A. Balogh, A. Bykov, P. Cargill, R. Dendy, T. Dudok de Wit, and J. Raymond, editors, *Microphysics of Cosmic Plasmas*, volume 47, pages 437–457. Springer US, Boston, MA, 2014.

[20] D. Burgess and M. Scholer. *Collisionless Shocks in Space Plasmas*. Cambridge University Press, 2015.

[21] J. H. Campbell and F. Rainer. Optical glasses for high-peak-power laser applications. In J. B. Breckinridge and A. J. M. III, editors, *Damage to Space Optics, and Properties and Characteristics of Optical Glass*. SPIE, jan 1993.

[22] D. Caprioli and A. Spitkovsky. Simulations of ion acceleration at non-relativistic shocks. i. acceleration efficiency. *The Astrophysical Journal*, 783(2):91, feb 2014.

[23] T. A. Casper and G. R. Smith. Observation of Alfvén ion-cyclotron fluctuations in the end-cell plasma in the tandem mirror experiment. *Physical Review Letters*, 48(15):1015–1018, apr 1982.

[24] F. F. Chen. Langmuir probe diagnostics. In *IEEE-ICOPS Meeting, Jeju, Korea*, volume 2, 2003.

[25] A. Collette and W. Gekelman. Structure of an exploding laser-produced plasma. *Physical Review Letters*, 105(19), nov 2010.

[26] A. Collette and W. Gekelman. Structure of an exploding laser-produced plasma. *Physics of Plasmas*, 18(5):055705, 2011.

[27] N. R. Council. *Severe Space Weather Events: Understanding Societal and Economic Impacts: A Workshop Report*. The National Academies Press, Washington, DC, 2008.

[28] G. Ding, J. E. Scharer, and K. L. Kelly. Effects of rapidly decaying plasmas on Langmuir probe measurements. *Journal of Applied Physics*, 84(3):1236–1240, aug 1998.

[29] S. Dorfman, H. Hietala, P. Astfalk, and V. Angelopoulos. Growth rate measurement of ULF waves in the ion foreshock. *Geophysical Research Letters*, 44(5):2120–2128, 2017.

[30] R. P. Drake. The design of laboratory experiments to produce collisionless shocks of cosmic relevance. *Physics of Plasmas*, 7(11):4690–4698, November 2000.

[31] N. Dubouloz and M. Scholer. On the origin of short large-amplitude magnetic structures upstream of quasi-parallel collisionless shocks. *Geophysical Research Letters*, 20(7):547–550, apr 1993.

[32] P. Dyal. Particle and field measurements of the starfish diamagnetic cavity. *Journal of Geophysical Research: Space Physics*, 111(A12):n/a–n/a, 2006. A12211.

[33] J. P. Eastwood, E. A. Lucek, C. Mazelle, K. Meziane, Y. Narita, J. Pickett, and R. A. Treumann. The foreshock. *Space Science Reviews*, 118(1-4):41–94, jun 2005.

[34] E. T. Everson, P. Pribyl, C. G. Constantin, A. Zylstra, D. Schaeffer, N. L. Kugland, and C. Niemann. Design, construction, and calibration of a three-axis, high-frequency magnetic probe 'b-dot probe'as a diagnostic for exploding plasmas. *Review of Scientific Insturments*, 80(11):113505, May 2009.

[35] R. Fitzpatrick. *Plasma Physics*. Taylor & Francis Inc, 2014.

[36] F. Fiuza, R. A. Fonseca, J. Tonge, W. B. Mori, and L. O. Silva. Weibel-instability-mediated collisionless shocks in the laboratory with ultraintense lasers. *Physical Review Letters*, 108(23), jun 2012.

[37] B. D. Fried and S. D. Conte. *The Plasma Dispersion Function*. Academic Press, 111 Fifth Avenue, New York, NY, 1961.

[38] B. Friedman and G. DuCharme. Semi-empirical scaling for ion–atom single charge exchange cross sections in the intermediate velocity regime. *Journal of Physics B: Atomic, Molecular and Optical Physics*, 50(11):115202, may 2017.

[39] S. Fuselier. Ion distributions in the Earth's foreshock upstream from the bow shock. *Advances in Space Research*, 15(8-9):43–52, jan 1995.

[40] L. Gargaté and A. Spitkovsky. Ion acceleration in non-relativistic astrophysical shocks. *The Astrophysical Journal*, 744(1):67, dec 2011.

[41] S. Gary and D. Schriver. The electromagnetic ion cyclotron beam anisotropy instability. *Planetary and Space Science*, 35(1):51–59, jan 1987.

[42] S. P. Gary. The electromagnetic ion beam instability and energy loss of fast alpha particles. *Nuclear Fusion*, 18(3):327–334, mar 1978.

[43] S. P. Gary. Electromagnetic ion/ion instabilities and their consequences in space plasmas: A review. *Space Science Reviews*, 56(3):373–415, 1991.

[44] S. P. Gary and C. D. Madland. Electromagnetic ion instabilities in a cometary environment. *Journal of Geophysical Research*, 93(A1):235, 1988.

[45] S. P. Gary, C. W. Smith, M. A. Lee, M. L. Goldstein, and D. W. Forslund. Electromagnetic ion beam instabilities. *Physics of Fluids*, 27(7):1852–1862, 1984.

[46] W. Gekelman, H. Pfister, Z. Lucky, J. Bamber, D. Leneman, and J. Maggs. Design, construction, and properties of the large plasma research device-the LAPD at UCLA. *Rev. Sci. Insturm.*, 62(12):2875–2883, December 1991.

[47] W. Gekelman, P. Pribyl, Z. Lucky, M. Drandell, D. Leneman, J. Maggs, S. Vincena, B. Van Compernolle, S. K. P. Tripathi, G. Morales, T. A. Carter, Y. Wang, and T. DeHaas. The upgraded large plasma device, a machine for studying frontier basic plasma physics. *Review of Scientific Instruments*, 87(2):025105, 2016.

[48] W. Gekelman, S. Vincena, B. V. Compernolle, G. J. Morales, J. E. Maggs, P. Pribyl, and T. A. Carter. The many faces of shear Alfvén waves. *Physics of Plasmas*, 18(5), 2011.

[49] I. Gingell, S. J. Schwartz, D. Burgess, A. Johlander, C. T. Russell, J. L. Burch, R. E. Ergun, S. Fuselier, D. J. Gershman, B. L. Giles, K. A. Goodrich, Y. V. Khotyaintsev, B. Lavraud, P.-A. Lindqvist, R. J. Strangeway, K. Trattner, R. B. Torbert, H. Wei, and F. Wilder. MMS observations and hybrid simulations of surface ripples at a marginally quasi-parallel shock. *Journal of Geophysical Research: Space Physics*, 122(11):11,003–11,017, nov 2017.

[50] K.-H. Glassmeier, A. J. Coates, M. H. Acuña, M. L. Goldstein, A. D. Johnstone, F. M. Neubauer, and H. Rème. Spectral characteristics of low-frequency plasma turbulence upstream of comet P/Halley. *Journal of Geophysical Research*, 94(A1):37, 1989.

[51] E. Greenstadt, G. Le, and R. Strangeway. ULF waves in the foreshock. *Advances in Space Research*, 15(8-9):71–84, jan 1995.

[52] E. W. Greenstadt. Oblique, parallel, and quasi-parallel morphology of collisionless shocks. In *Collisionless Shocks in the Heliosphere: Reviews of Current Research*, pages 169–184. American Geophysical Union, 1985.

[53] J. Grun, R. Decoste, B. H. Ripin, and J. Gardner. Characteristics of ablation plasma from planar, laser-driven targets. *Applied Physics Letters*, 39(7):545–547, 1981.

[54] J. Grun, R. Stellingwerf, and B. H. Ripin. Control of ion-velocity distributions in laser–target interaction experiments. *The Physics of Fluids*, 29(10):3390–3393, 1986.

[55] A. Gurevich and L. Pitaevskii. Recombination coefficient in a dense low-temperature plasma. *Zh. Eksp. Teor. Fiz*, 46, 1964.

[56] L. Hackel, J. Miller, and C. Dane. Phase conjugation in a high power regenerative laser amplifier system. *International Journal of Nonlinear Optical Physics*, 2(01):171–185, 1993.

[57] T. Hada, C. F. Kennel, and T. Terasawa. Excitation of compressional waves and the formation of shocklets in the Earth's foreshock. *Journal of Geophysical Research: Space Physics (1978–2012)*, 92(A5):4423–4435, 5 1987.

[58] H. J. Hartfuss, T. Geist, and M. Hirsch. Heterodyne methods in millimetre wave plasma diagnostics with applications to ECE, interferometry and reflectometry. *Plasma Physics and Controlled Fusion*, 39(11):1693–1769, nov 1997.

[59] W. Heidbrink, E. Fredrickson, N. Gorelenkov, T. Rhodes, and M. V. Zeeland. Observation of compressional Alfvén eigenmodes (CAE) in a conventional tokamak. *Nuclear Fusion*, 46(2):324–334, jan 2006.

[60] P. Hellinger and A. Mangeney. Electromagnetic ion beam instabilities: Oblique pulsations. *Journal of Geophysical Research: Space Physics*, 104(A3):4669–4680, mar 1999.

[61] P. Heuer, D. Schaeffer, E. Knall, C. Constantin, L. Hofer, S. Vincena, S. Tripathi, and C. Niemann. Fast gated imaging of the collisionless interaction of a laser-produced and magnetized ambient plasma. *High Energy Density Physics*, 22:17 – 20, 2017.

[62] P. V. Heuer, M. S. Weidl, R. S. Dorst, D. B. Schaeffer, A. S. Bondarenko, S. K. P. Tripathi, B. Van Compernolle, S. Vincena, C. G. Constantin, C. Niemann, and D. Winske. Observations of a field-aligned ion/ion-beam instability in a magnetized laboratory plasma. *Physics of Plasmas*, 25(3):032104, 2018.

[63] P. V. Heuer, M. S. Weidl, R. S. Dorst, D. B. Schaeffer, S. K. P. Tripathi, S. Vincena, C. G. Constantin, C. Niemann, L. B. Wilson, and D. Winske. Laboratory observations of ultra-low frequency analogue waves driven by the right-hand resonant ion beam instability. *The Astrophysical Journal Letters*, 891(1):L11, feb 2020.

[64] P. V. Heuer, M. S. Weidl, R. S. Dorst, D. B. Schaeffer, S. K. P. Tripathi, S. Vincena, C. G. Constantin, C. Niemann, and D. Winske. Laser-produced plasmas as drivers of laboratory collisionless quasi-parallel shocks. *Physics of Plasmas*, 27(4):042103, 2020.

[65] H. Hietala, T. V. Laitinen, K. Andréeová, R. Vainio, A. Vaivads, M. Palmroth, T. I. Pulkkinen, H. E. J. Koskinen, E. A. Lucek, and H. Rème. Supermagnetosonic jets behind a collisionless quasiparallel shock. *Physical Review Letters*, 103(24), dec 2009.

[66] M. Hoppe and C. Russell. On the nature of ULF waves upstream of planetary bow shocks. *Advances in Space Research*, 1(1):327 – 332, 1981.

[67] G. G. Howes. Laboratory space physics: Investigating the physics of space plasmas in the laboratory. *Physics of Plasmas*, 25(5):055501, 2018.

[68] J. Huba. *NRL Plasma Formulary*. Naval Research Laboratory, 2017.

[69] J. D. Huba, J. G. Lyon, and A. B. Hassam. Theory and simulation of the Rayleigh-Taylor instability in the limit of large Larmor radius. *Phys. Rev. Lett.*, 59:2971–2974, Dec 1987.

[70] C. M. Huntington, F. Fiuza, J. S. Ross, A. B. Zylstra, R. P. Drake, D. H. Froula, G. Gregori, N. L. Kugland, C. C. Kuranz, M. C. Levy, C. K. Li, J. Meinecke, T. Morita, R. Petrasso, C. Plechaty, B. A. Remington, D. D. Ryutov, Y. Sakawa, A. Spitkovsky, H. Takabe, and H.-S. Park. Observation of magnetic field generation via the Weibel instability in interpenetrating plasma flows. *Nature Physics*, 11(2):173–176, jan 2015.

[71] I. H. Hutchinson. *Principles of Plasma Diagnostics*. Cambridge University Press, 2002.

[72] R. Janev, R. Phaneuf, and H. Hunter. Recommmended cross sections for electron capture and ionization in collisions of C^{q+} and O^{q+} ions with H, He, and H_2. *Atomic Data and Nuclear Data Tables*, 40(2):249 – 281, 1988.

[73] T. R. Jarboe. Review of spheromak research. *Plasma Physics and Controlled Fusion*, 36(6):945–990, jun 1994.

[74] H. W. Jeffrey. Magnetospheric ulf waves: A tutorial with a historical perspective. In M. J. Engebretson, K. Takahashi, and M. Scholer, editors, *Solar Wind Sources of Magnetospheric Ultra-Low-Frequency Waves*, volume 81 of *Geophysical Monograph Series*, pages 1–11. American Geophysical Union (AGU), 2000 Florida Avenue, NW, Washington, DC, 20009, USA, apr 2013.

[75] C. F. Kennel and H. E. Petschek. Limit on stably trapped particle fluxes. *Journal of Geophysical Research*, 71(1):1–28, jan 1966.

[76] K. Killen, N. Omidi, D. Krauss-Varban, and H. Karimabadi. Linear and nonlinear properties of ULF waves driven by ring-beam distribution functions. *Journal of Geophysical Research*, 100(A4):5835, 1995.

[77] D. W. Koopman. Momentum transfer interaction of a laser-produced plasma with a low-pressure background. *Physics of Fluids*, 15(11):1959, 1972.

[78] A. Koval. Wind magnetic fields investigation high-resolution definitive data (WI H2 MFI). CDAWeb.

[79] N. A. Krall and A. W. Trivelpiece. *Principles of Plasma Physics*. McGraw-Hill Book Company, 1973.

[80] T. B. Krause, A. Apte, and P. J. Morrison. A unified approach to the Darwin approximation. *Physics of Plasmas*, 14(10):102112, oct 2007.

[81] J. B. Lestz, N. N. Gorelenkov, E. V. Belova, S. X. Tang, and N. A. Crocker. Analytic stability boundaries for compressional and global Alfvén eigenmodes driven by fast ions. i. interaction via ordinary and anomalous cyclotron resonances. *Physics of Plasmas*, 27(2):022513, feb 2020.

[82] R. Linn and S. Bale. Wind ion moments at 3 second spin resolution (WI PM 3DP). CDAWeb.

[83] R. B. Lobbia and A. D. Gallimore. Temporal limits of a rapidly swept Langmuir probe. *Physics of Plasmas*, 17(7):073502, jul 2010.

[84] E. A. Lucek, T. S. Horbury, I. Dandouras, and H. Rème. Cluster observations of the Earth's quasi-parallel bow shock. *Journal of Geophysical Research: Space Physics*, 113(A7):n/a–n/a, jun 2008.

[85] R. L. Merlino. Understanding Langmuir probe current-voltage characteristics. *American Journal of Physics*, 75(12):1078–1085, dec 2007.

[86] C. Mitchell, S. Vincena, J. Maggs, and W. Gekelman. Laboratory observation of Alfvén resonance. *Geophysical Research Letters*, 28(5):923–926, 2001.

[87] H. M. Mott-Smith and I. Langmuir. The theory of collectors in gaseous discharges. *Phys. Rev.*, 28:727–763, Oct 1926.

[88] S. N. Nahar and A. K. Pradhan. Electron-ion recombination rate coefficients, photoionization cross sections, and ionization fractions for astrophysically abundant elements. i. carbon and nitrogen. *The Astrophysical Journal Supplement Series*, 111(1):339, 1997.

[89] C. Niemann, C. G. Constantin, D. B. Schaeffer, A. Tauschwitz, T. Weiland, Z. Lucky, W. Gekelman, E. T. Everson, and D. Winske. High-energy Nd:glass laser facility for collisionless laboratory astrophysics. *Journal of Instrumentation*, 7(03):P03010, March 2012.

[90] C. Niemann, W. Gekelman, C. G. Constantin, E. T. Everson, D. B. Schaeffer, A. S. Bondarenko, S. E. Clark, D. Winske, S. Vincena, B. V. Compernolle, and P. Pribyl. Observation of collisionless shocks in a large current-free laboratory plasma. *Geophysical Research Letters*, 41:7413–7418, 2014.

[91] C. Niemann, W. Gekelman, C. G. Constantin, E. T. Everson, D. B. Schaeffer, S. E. Clark, D. Winske, A. B. Zylstra, P. Pribyl, S. K. P. Tripathi, D. Larson, S. H. Glenzer, and A. S. Bondarenko. Dynamics of exploding plasmas in a large magnetized plasma. *Physics of Plasmas*, 20(1):012108, January 2013.

[92] N. Omidi, D. Sibeck, O. Gutynska, and K. J. Trattner. Magnetosheath filamentary structures formed by ion acceleration at the quasi-parallel bow shock. *Journal of Geophysical Research: Space Physics*, 119(4):2593–2604, apr 2014.

[93] N. Omidi, H. Zhang, D. Sibeck, and D. Turner. Spontaneous hot flow anomalies at quasi-parallel shocks: 2. hybrid simulations. *Journal of Geophysical Research: Space Physics*, 118(1):173–180, jan 2013.

[94] T. G. Onsager, D. Winske, and M. F. Thomsen. Interaction of a finite-length ion beam with a background plasma: Reflected ions at the quasi-parallel bow shock. *Journal of Geophysical Research: Space Physics (1978–2012)*, 96(A2):1775–1788, 2 1991.

[95] H.-S. Park, C. M. Huntington, F. Fiuza, R. P. Drake, D. H. Froula, G. Gregori, M. Koenig, N. L. Kugland, C. C. Kuranz, D. Q. Lamb, M. C. Levy, C. K. Li, J. Meinecke, T. Morita, R. D. Petrasso, B. B. Pollock, B. A. Remington, H. G. Rinderknecht, M. Rosenberg, J. S. Ross, D. D. Ryutov, Y. Sakawa, A. Spitkovsky, H. Takabe, D. P.

Turnbull, P. Tzeferacos, S. V. Weber, and A. B. Zylstra. Collisionless shock experiments with lasers and observation of Weibel instabilities. *Physics of Plasmas*, 22(5):056311, may 2015.

[96] G. K. Parks, E. Lee, S. Y. Fu, N. Lin, Y. Liu, and Z. W. Yang. Shocks in collisionless plasmas. *Reviews of Modern Plasma Physics*, 1(1):1, Jun 2017.

[97] G. Paschmann, N. Sckopke, I. Papamastorakis, J. R. Asbridge, S. J. Bame, and J. T. Gosling. Characteristics of reflected and diffuse ions upstream from the Earth's bow shock. *Journal of Geophysical Research: Space Physics*, 86(A6):4355–4364, jun 1981.

[98] C. S. Peri, P. Benaglia, D. P. Brookes, I. R. Stevens, and N. L. Isequilla. E-BOSS: an extensive stellar BOw shock survey. *Astronomy & Astrophysics*, 538:A108, feb 2012.

[99] W. Press. *Numerical recipes in FORTRAN : the art of scientific computing*. Cambridge University Press, Cambridge England New York, NY, USA, 1992.

[100] B. H. Ripin, J. D. Huba, E. A. McLean, C. K. Manka, T. Peyser, H. R. Burris, and J. Grun. Sub-Alfvénic plasma expansion. *Physics of Fluids B*, 5(10), June 1993.

[101] P. T. Rumsby and J. W. M. Paul. Temperature and density of an expanding laser produced plasma. *Plasma Physics*, 16(3):247, 1974.

[102] M. J. Runkel, A. K. Burnham, D. Milam, W. D. Sell, M. D. Feit, and A. M. Rubenchik. Results of pulse-scaling experiments on rapid-growth DKDP triplers using the optical sciences laser at 351 nm. In G. J. Exarhos, A. H. Guenther, M. R. Kozlowski, K. L. Lewis, and M. J. Soileau, editors, *Laser-Induced Damage in Optical Materials: 2000*. SPIE, apr 2001.

[103] F. L. Scarf, D. A. Gurnett, W. S. Kurth, and R. L. Poynter. Plasma wave turbulence at Jupiter's bow shock. *Nature*, 280(5725):796–797, aug 1979.

[104] D. B. Schaeffer, A. S. Bondarenko, E. T. Everson, S. E. Clark, C. G. Constantin, and C. Niemann. Characterization of laser-produced carbon plasmas relevant to laboratory astrophysics. *Journal of Applied Physics*, 120(4):043301, 2016.

[105] D. B. Schaeffer, E. T. Everson, A. S. Bondarenko, S. E. Clark, C. G. Constantin, D. Winske, W. Gekelman, and C. Niemann. Experimental study of subcritical laboratory magnetized collisionless shocks using a laser-driven magnetic piston. *Physics of Plasmas*, 22(11):113101, 2015.

[106] D. B. Schaeffer, W. Fox, D. Haberberger, G. Fiksel, A. Bhattacharjee, D. H. Barnak, S. X. Hu, and K. Germaschewski. Generation and evolution of high-Mach-number laser-driven magnetized collisionless shocks in the laboratory. *Phys. Rev. Lett.*, 119, July 2017.

[107] D. B. Schaeffer, L. R. Hofer, E. N. Knall, P. V. Heuer, C. G. Constantin, and C. Niemann. A platform for high-repetition-rate laser experiments on the large plasma device. *High Power Laser Science and Engineering*, 6:e17, 2018.

[108] M. Scholer. Upstream waves, shocklets, short large-amplitude magnetic structures and the cyclic behavior of oblique quasi-parallel collisionless shocks. *Journal of Geophysical Research: Space Physics*, 98(A1):47–57, jan 1993.

[109] M. Scholer and D. Burgess. The role of upstream waves in supercritical quasi-parallel shock re-formation. *Journal of Geophysical Research*, 97(A6):8319, 1992.

[110] M. Scholer and T. Terasawa. Ion reflection and dissipation at quasi-parallel collisionless shocks. *Geophysical Research Letters*, 17(2):119–122, feb 1990.

[111] P. Song and C. Russell. Time series data analysis in space physics. *Space Science Reviews*, 87(3/4):387–463, 1999.

[112] L. C. Steinhauer. Review of field-reversed configurations. *Physics of Plasmas*, 18(7):070501, jul 2011.

[113] T. H. Stix. *Waves in plasmas*. Springer Science & Business Media, 1992.

[114] E. C. Stone. Voyager 1 explores the termination shock region and the heliosheath beyond. *Science*, 309(5743):2017–2020, sep 2005.

[115] A. V. Streltsov, M. Lampe, W. Manheimer, G. Ganguli, and G. Joyce. Whistler propagation in inhomogeneous plasma. *Journal of Geophysical Research: Space Physics*, 111(A3), 2006.

[116] A. V. Streltsov, J. R. Woodroffe, and J. D. Huba. Propagation of whistler mode waves through the ionosphere. *Journal of Geophysical Research: Space Physics*, 117(A8), 2012.

[117] G. I. Taylor. The spectrum of turbulence. *Proceedings of the Royal Society of London. Series A, Mathematical and Physical Sciences*, 164(919):476–490, 1938.

[118] T. Terasawa, M. Hoshino, J. Sakai, and T. Hada. Decay instability of finite-amplitude circularly polarized Alfvén waves: A numerical simulation of stimulated brillouin scattering. *Journal of Geophysical Research*, 91(A4):4171–4187, 4 1986.

[119] V. A. Thomas, D. Winske, M. F. Thomsen, and T. G. Onsager. Hybrid simulation of the formation of a hot flow anomaly. *Journal of Geophysical Research*, 96(A7):11625, 7 1991.

[120] M. F. Thomsen, J. T. Gosling, S. J. Bame, K. B. Quest, C. T. Russell, and S. A. Fuselier. On the origin of hot diamagnetic cavities near the Earth's bow shock. *Journal of Geophysical Research*, 93(A10):11311, 1988.

[121] V. N. Tishchenko, A. G. Berezutsky, E. L. Boyarintsev, Y. P. Zakharov, I. B. Miroshnichenko, V. G. Posukh, A. G. Ponomarenko, A. A. Chibranov, and I. F. Shaikhislamov. Low-frequency waves produced by a package of laser plasma clouds in a magnetized background. *Journal of Physics: Conference Series*, 1404:012100, nov 2019.

[122] S. K. P. Tripathi, B. Van Compernolle, W. Gekelman, P. Pribyl, and W. Heidbrink. Excitation of shear Alfvén waves by a spiraling ion beam in a large magnetoplasma. *Phys. Rev. E*, 91, Jan 2015.

[123] B. Trubnikov. Reviews of plasma physics. *Consultant Bureau, New York*, 1:226, 1965.

[124] K. Tsubouchi and B. Lembège. Full particle simulations of short large-amplitude magnetic structures (SLAMS) in quasi-parallel shocks. *Journal of Geophysical Research: Space Physics*, 109(A2):n/a–n/a, 2004. A02114.

[125] B. T. Tsurutani. Comets: a laboratory for plasma waves and instabilities. In A. D. Johnstone, editor, *Cometary Plasma Processes*, volume 61 of *Geophysical Monograph Series*, pages 189–209. American Geophysical Union (AGU), 2000 Florida Avenue, NW, Washington, DC 20009, USA, mar 2013.

[126] B. T. Tsurutani, E. J. Smith, and D. E. Jones. Waves observed upstream of interplanetary shocks. *Journal of Geophysical Research: Space Physics (1978–2012)*, 88(A7):5645–5656, 7 1983.

[127] D. L. Turner, N. Omidi, D. G. Sibeck, and V. Angelopoulos. First observations of foreshock bubbles upstream of Earth's bow shock: Characteristics and comparisons to HFAs. *Journal of Geophysical Research: Space Physics*, 118(4):1552–1570, apr 2013.

[128] D. L. Turner, L. B. Wilson, T. Z. Liu, I. J. Cohen, S. J. Schwartz, A. Osmane, J. F. Fennell, J. H. Clemmons, J. B. Blake, J. Westlake, B. H. Mauk, A. N. Jaynes, T. Leonard, D. N. Baker, R. J. Strangeway, C. T. Russell, D. J. Gershman, L. Avanov, B. L. Giles, R. B. Torbert, J. Broll, R. G. Gomez, S. A. Fuselier, and J. L. Burch. Autogenous and efficient acceleration of energetic ions upstream of Earth's bow shock. *Nature*, 561(7722):206–210, sep 2018.

[129] B. Van Compernolle, G. J. Morales, and W. Gekelman. Cherenkov radiation of shear Alfvén waves. *Physics of Plasmas*, 15(8), 2008.

[130] M. VanZeeland and W. Gekelman. Laser-plasma diamagnetism in the presence of an ambient magnetized plasma. *Physics of Plasmas*, 11(1):320–323, jan 2004.

[131] M. VanZeeland, W. Gekelman, S. Vincena, and G. Dimonte. Production of Alfvén waves by a rapidly expanding dense plasma. *Phys. Rev. Lett.*, 87, Aug 2001.

[132] S. Vincena, W. Gekelman, M. A. V. Zeeland, J. Maggs, and A. Collette. Quasielectrostatic whistler wave radiation from the hot electron emission of a laser-produced plasma. *Physics of Plasmas*, 15(7):072114, jul 2008.

[133] X. Y. Wang and Y. Lin. Generation of filamentary structures by beam-plasma interaction. *Physics of Plasmas*, 13(5):052102, may 2006.

[134] M. S. Weidl, P. Heuer, D. Schaeffer, R. Dorst, D. Winske, C. Constantin, and C. Niemann. Towards a parallel collisionless shock in LAPD. *Journal of Physics: Conference Series*, 900(1):012020, 2017.

[135] M. S. Weidl, D. Winske, F. Jenko, and C. Niemann. Hybrid simulations of a parallel collisionless shock in the large plasma device. *Physics of Plasmas*, 23(12), 2016.

[136] M. S. Weidl, D. Winske, and C. Niemann. On the background-gyroresonant character of Bell's instability in the large-current regime. *The Astrophysical Journal*, 872(1):48, feb 2019.

[137] M. S. Weidl, D. Winske, and C. Niemann. Three regimes and four modes for the resonant saturation of parallel ion-beam instabilities. *The Astrophysical Journal*, 873(1):57, mar 2019.

[138] L. Wilson, D. Sibeck, D. Turner, A. Osmane, D. Caprioli, and V. Angelopoulos. Relativistic electrons produced by foreshock disturbances observed upstream of Earth's bow shock. *Physical Review Letters*, 117(21), nov 2016.

[139] L. B. Wilson, C. Cattell, P. J. Kellogg, K. Goetz, K. Kersten, L. Hanson, R. MacGregor, and J. C. Kasper. Waves in interplanetary shocks: A wind/WAVES study. *Physical Review Letters*, 99(4), jul 2007.

[140] L. B. Wilson, A. Koval, D. G. Sibeck, A. Szabo, C. A. Cattell, J. C. Kasper, B. A. Maruca, M. Pulupa, C. S. Salem, and M. Wilber. Shocklets, SLAMS, and field-aligned ion beams in the terrestrial foreshock. *Journal of Geophysical Research: Space Physics*, 118(3):957–966, 3 2013.

[141] L. B. Wilson, A. Koval, A. Szabo, A. Breneman, C. A. Cattell, K. Goetz, P. J. Kellogg, K. Kersten, J. C. Kasper, B. A. Maruca, and M. Pulupa. Observations of electromagnetic whistler precursors at supercritical interplanetary shocks. *Geophysical Research Letters*, 39(8):L08109, Apr. 2012.

[142] L. B. Wilson III. Low frequency waves at and upstream of collisionless shocks. In A. Keiling, D. Lee, and V. Nakariakov, editors, *Low-Frequency Waves in Space Plasmas*, volume 216 of *Geophysical Monograph Series*, chapter 16, pages 269–291. American Geophysical Union (AGU) and John Wiley & Sons, Inc., 2000 Florida Avenue, NW, Washington DC, 20009, USA and Hoboken, NJ, feb 2016.

[143] D. Winske, J. D. Huba, C. Niemann, and A. Le. Recalling and updating research on diamagnetic cavities: Experiments, theory, simulations. *Frontiers in Astronomy and Space Sciences*, 5, jan 2019.

[144] D. Winske and M. M. Leroy. Diffuse ions produced by electromagnetic ion beam instabilities. *Journal of Geophysical Research*, 89(A5):2673–2688, May 1984.

[145] D. Winske, N. Omidi, K. B. Quest, and V. A. Thomas. Re-forming supercritical quasi-parallel shocks: 2. mechanism for wave generation and front re-formation. *Journal of Geophysical Research*, 95(A11):18821, 1990.

[146] J. R. Woodroffe and A. V. Streltsov. Whistler interactions with density gradients in the magnetosphere. *Journal of Geophysical Research: Space Physics*, 118(1):167–172, 2013.

[147] N. C. Woolsey, Y. A. Ali, R. G. Evans, R. A. D. Grundy, S. J. Pestehe, P. G. Carolan, N. J. Conway, R. O. Dendy, P. Helander, K. G. McClements, J. G. Kirk, P. A. Norreys, M. M. Notley, and S. J. Rose. Collisionless shock and supernova remnant simulations on VULCAN. *Phys. Plasmas*, 8(5):2439–2445, May 2001.

[148] P. H. Yoon, V. S. Pandey, and D.-H. Lee. Oblique nonlinear whistler wave. *Journal of Geophysical Research: Space Physics*, 119(3):1851–1862, mar 2014.

[149] Y. P. Zakharov, A. Orishich, A. Ponomarenko, and V. Posukh. Effectiveness of the slowing of expanding clouds of diamagnetic plasma by a magnetic field (experimental). *Sov. J. Plasma Phys*, 12(10):674–678, 1986.

[150] G. Zank. Interaction of the solar wind with the local interstellar medium: a theoretical perspective. *Space Science Reviews*, 89(3/4):413–688, 1999.